



저작자표시-비영리-변경금지 2.0 대한민국

이용자는 아래의 조건을 따르는 경우에 한하여 자유롭게

- 이 저작물을 복제, 배포, 전송, 전시, 공연 및 방송할 수 있습니다.

다음과 같은 조건을 따라야 합니다:



저작자표시. 귀하는 원저작자를 표시하여야 합니다.



비영리. 귀하는 이 저작물을 영리 목적으로 이용할 수 없습니다.



변경금지. 귀하는 이 저작물을 개작, 변형 또는 가공할 수 없습니다.

- 귀하는, 이 저작물의 재이용이나 배포의 경우, 이 저작물에 적용된 이용허락조건을 명확하게 나타내어야 합니다.
- 저작권자로부터 별도의 허가를 받으면 이러한 조건들은 적용되지 않습니다.

저작권법에 따른 이용자의 권리는 위의 내용에 의하여 영향을 받지 않습니다.

이것은 [이용허락규약\(Legal Code\)](#)을 이해하기 쉽게 요약한 것입니다.

[Disclaimer](#)

공학박사학위논문

Thermally Driven
Intrinsic and Extrinsic Doping Mechanisms in
Amorphous Oxide Semiconductors

열에너지에 의한 비정질 산화물 반도체의
내인성 및 외인성 도핑 메커니즘 연구

2016년 2월

서울대학교 대학원

재료공학부

연 한 울

ABSTRACT

Thermally Driven Intrinsic and Extrinsic Doping Mechanisms in Amorphous Oxide Semiconductors

Han-Wool Yeon

Department of Materials Science and Engineering

The Graduate School

Seoul National University

Amorphous oxide semiconductors (AOSs) have been considered as one of the most promising materials for implementation of next-generation electronic devices that are flexible, transparent, and large-area applicable due to their novel properties. AOSs have long-range film uniformity induced by long-range structural disorder and show excellent electron mobility comparable to the corresponding crystalline oxide semiconductors. However, the use of AOSs in electronic devices has been hindered by the lack of controllability of electrical properties as well as stability, which is induced by various electronic states of dopant in subgap region. Although electron mobility is relatively insensitive to structural disorder, electronic states of both *intrinsic* and *extrinsic* dopants are affected by the local atomic structure. As a result, dopants form various electronic states and irregular doping efficiency is observed. Moreover, degree of structural disorder tends to decrease because amorphous structure is thermodynamically metastable, which is referred as structural relaxation (SR). Thus, doping efficiency of dopants as well as distribution of subgap states could change by thermal stress. Therefore, understanding the continuous change of doping efficiency of *intrinsic* and

extrinsic dopants driven by thermal stress is necessary for controlling the electrical properties and improving the of stability of AOSs.

The objective of this thesis is to unravel the *intrinsic* and *extrinsic* doping mechanisms in AOSs with respect to thermal history and to provide guidelines for not only delicate control of electrical properties, but also creation of new functionality in AOSs. Before investigating thermally driven doping mechanisms in AOSs, it is necessary to regulate the additional reactions in AOSs such as redox reactions. In this study, novel metal/AOSs/metal structured devices are designed to prevent unwanted reactions of AOSs with the ambient. Based on the devices, changes in electrical properties of AOSs induced by *intrinsic* atomic rearrangement as well as *extrinsic* dopant migration were investigated.

First, concentration of oxygen vacancy (V_O) as an intrinsic donor in amorphous In-Ga-Zn-O (a-IGZO) was modulated by solely SR. As annealing temperature increases from 300 °C to 450 °C, concentration of V_O in the shallow donor state 1000 time increases. The SR-driven intrinsic doping effect depends strongly on the annealing temperature but not on the annealing time. The Arrhenius activation energy of the SR-driven doping effect is 1.76 eV, which is similar to the bonding energies in a-IGZO. Free volume in a-IGZO decreases during SR and V_O in either deep-donor or electron-trap states consequently transforms into shallow-donor state.

The second focus is to identify the electronic states of *extrinsic* Cu dopant in AOSs. Amorphization of Cu-based metal oxides have induced peculiar electrical characteristics with loss of *p*-type characteristics of Cu dopant in the corresponding crystalline oxides. Therefore, unravelling the doping mechanism of Cu in AOSs is essential to determine the exact electronic states of Cu in AOSs. In the early stage of annealing, Cu dominantly diffuses into a-IGZO through the free volume and acts as an electron donor and increases

electrical conductivity of a-IGZO. Moreover, resistive switching (RS) characteristics are generated in Cu-doped a-IGZO due to the electrochemical migration of Cu at the free volume. With further annealing, substitutional Cu becomes predominant which prefers In to Ga or Zn. After annealing, inter-diffused Cu and In form crystalline Cu-In-O clusters in a-IGZO. Cu-In-O clusters not only form bulk-heterogeneous *pn* junction, but also give rise to negative differential resistance behavior in a-IGZO. RS performance can be modulated by Cu doping concentration at the free volume as well as the formation of Cu-In-O clusters.

This study reported thermally-driven *intrinsic* and *extrinsic* doping mechanism in AOSs without any reactions of AOSs with the ambient using the novel metal/AOSs/metal structured devices. A systematic study on electrical conduction mechanism analysis of the devices, microstructural and chemical analysis provided useful information for understanding the changes in electronic state of *intrinsic* and *extrinsic* dopants according to the structural location and suggested that *extrinsic* doping control gives rises to new-functionality in AOSs such as resistive switching in addition to the modulation of electrical conductivity.

Keywords: amorphous oxide semiconductors, In-Ga-Zn-O, doping, oxygen vacancy, Cu, electronic states, structural relaxation, diffusion, resistive switching, memristor

Student Number: 2009-23046

Table of Contents

Abstract.....	i
Table of Contents.....	iv
List of Tables.....	viii
List of Figures.....	ix

Chapter 1. Introduction

1.1. Amorphous oxide semiconductor-based electronic devices	1
1.2. Doping issues in amorphous oxide semiconductors	5
1.2.1. Effect of structural disorder on doping efficiency	5
1.2.2. Intrinsic doping: oxygen vacancy with hydrogen	15
1.2.3. Extrinsic doping: copper	20
1.3. Objective of the thesis	26
1.4. Organization of the thesis	29

Chapter 2. Theoretical Background

2.1. Subgap states in amorphous oxide semiconductors	30
2.1.1. Structural disorder	31
2.1.2. Chemical disorder	33
2.2. Structural relaxation in amorphous solid	44

2.3. Electrical conduction mechanisms in metal/semiconductor/metal structures	46
2.3.1. Schottky emission	46
2.3.2. Poole-Frenkel conduction	49
2.3.3. Space-charge-limited conduction	50
2.3.4. Tunneling-based conduction	51
2.4 Introduction to resistive switching devices	52

Chapter 3. Experimental Procedures

3.1. Sample preparation	63
3.1.1. Device fabrication	63
3.1.2. Multi-layer thin-films	66
3.1.3. Van der Pauw samples	67
3.2. Structural and optical analysis	68
3.3. Post-fabrication annealing	69
3.4. Electrical analysis	70
3.5. Microstructural and chemical analysis	71
3.6. Computation	72

Chapter 4. Development of the Devices Able to Regulate Extrinsic Reactions of Amorphous Oxide Semiconductors

4.1. Introduction	73
4.2. Experiments	74
4.3. Characteristics of as-deposited oxide films	75

4.4. Microstructural changes	79
4.5. Chemical state changes	84
4.6. I - V characteristics changes	87
4.7. Summary	95

Chapter 5. Structural Relaxation-Driven Intrinsic Doping

5.1. Introduction	97
5.2. Experiments	98
5.3. I - V characteristics changes	98
5.4. Conduction mechanism analysis	105
5.4.1. Schottky-thermionic emission	105
5.4.2. Ohmic and Poole-Frenkel conduction	110
5.4.3. Extraction of free electron/doping concentration	114
5.5. C - V characteristics of Schottky conducting devices	127
5.6. Effect of H dopant	142
5.7. Summary	145

Chapter 6. Dynamical Changes in Cu Doping Effect

6.1. Introduction	146
6.2. Experiments	147
6.3. I - V characteristics changes	148
6.4. Conduction mechanism analysis	155
6.5. Electrical breakdown behavior	159
6.5.1. The origin of resistive switching	159

6.5.2. Resistive switching characteristics	165
6.6. Microstructural and chemical analysis	171
6.7. Cu diffusion modeling	178
6.8. Summary	182

Chapter 7. Conclusion

7.1. Summary of results	183
7.2. Future works and suggested research	185
7.2.1. Effect of O non-stoichiometry on SR-driven doping	185
7.2.2. Flexible Cu-doped AOSs memristor	187
References	189
Abstract (In Korean)	206
Curriculum Vitae	210

LIST OF TABLES

Table 1.1	Comparison of electron configuration, bonding energy, and bond length of In, Ga, Zn in a-IGZO (InGaZnO_4)
------------------	--

LIST OF FIGURES

- Figure 1.1** (a) Mobility and frequency capability of materials for TFTs. (b) Schematic drawings of metal s orbitals in ionic oxide semiconductors. Applications of AOSs on various electronic devices: (c) flexible AOSs TFTs, (d) AOSs TFTs-based displays, (e) integration with non-volatile memory, (f) AOSs TFTs-based CMOS circuits, (g) touch-free image sensors based on AOSs photo transistors, and (h) flexible Schottky diodes for high-frequency mobile phones. (i) Illustration of future transparent and flexible systems of IoT.
- Figure 1.2** (a) Variations in hall mobility of $\text{In}_2\text{O}_3\text{-Ga}_2\text{O}_3\text{-ZnO}$ thin films with respect to chemical composition changes. (b) Stability of a-IZO and a-IGZO thin-films after deposition.
- Figure 1.3** (a) Deposition methods of AOSs thin-films and/or doping processes in AOSs. (b) Doping elements in AOSs in terms of electric role.
- Figure 1.4** Distributions of dopants in semiconductors with respect to phase condition; crystalline or amorphous structure. In amorphous phase, dopants form various local atomic structure. Thus, doping efficiency in AOSs is exceedingly low compared to the corresponding crystalline oxide semiconductors. Moreover, dopants form various electronic states in subgap region.

Figure 1.5 (a) Carrier concentration of Li-doped-Zn-Sn-O (Li-ZTO) films and threshold voltage of Li-ZTO TFTs with respect to Li doping concentration. (b) Hall mobility of Y-doped In-Zn-O (Y-IZO) according to deposition power of Y_2O_3 . (c) Transfer characteristics of a-IGZO TFTs according to density of a-IGZO thin-films. Chemical composition of In, Ga, and Zn is nearly constant regardless of film density. (d) Resistivity changes in a-IGZO with respect to pulsed laser deposition power and oxygen partial pressure ($P_{O_2,DEP.}$) during film deposition. Chemical composition of In, Ga, and Zn is not affected by the deposition power.

Figure 1.6 Thermally driven atomic rearrangement in AOSs in terms of intrinsic and extrinsic factors.

Figure 1.7 (a) Candidate for annealing sequences during TFTs fabrication. Transfer curves of (b) solution-derived a-IGZO TFTs and (b) a-IGZO TFTs based on vacuum-deposition process with respect to annealing temperature. (c) Subgap density of states in a-IGZO TFTs (Figure 1.7b) obtained by device simulation (TCAD) and the capacitance-voltage method. (d) Correlation between the Kiessig fringe periods of the active thin films pre-annealed at various temperatures and their transistor performance of effective mobility and on-voltage. Active material is Si-W-In-O. The data in brackets are the estimated film thickness from the Kiessig fringe periods with unit of nm. (e) contact resistance (ρ_c) and sheet resistance of a-IGZO thin films (R_{sh}). Ti was selected as contact material.

Figure 1.8 (a) Transfer curves of a-IGZO TFTs after annealing at 400 °C for 1 h in dry O₂ and wet O₂ atmosphere at 1 atm. with respect to annealing temperature. (b) Thermal desorption spectra (TDS) of a-IGZO thin films during annealing from 60 to 700 °C at a heating rate of 60 °C·min⁻¹. Background pressure of vacuum chamber for TDS measurement is around 10⁻⁷ Pa. The magnitude of H₂O, O₂, Zn is varied among the samples and H₂O, O₂, and Zn intensively desorb from un-annealed a-IGZO thin films. (c) Time variations of threshold voltage shift (ΔV_{th}) under constant current (I) stress for a-IGZO TFTs. After annealing in dry O₂ and wet O₂ (19.7% of H₂O), bias stability of a-IGZO TFTs is enhanced. (d) Subgap density of states in a-IGZO TFTs (Figure 1.8) obtained by device simulation (TCAD) and the capacitance-voltage method.

Figure 1.9 (a) Schematics of subgap density of states (DOS) in a-IGZO which is modified from ref. 1.3. (b) Local coordination structures of some oxygen vacancies.

Figure 1.10 Illustration of the free volume changes in amorphous solid during isothermal annealing below T_g .

Figure 1.11 (a) Composition profile of a-IGZO measured by secondary ion mass spectroscopy (SIMS). Electron doping in a-IGZO by (b) annealing in H₂ ambient (3%), and (c) H plasma at RT. (d) The changes of Subgap DOS in a-IGZO TFTs with respect to H₂ high-pressure annealing (HPA) conditions. (e) SIMS depth profile of H in a-IGZO thin-films. Diffusivity of H is $\sim 10^{-14}$ cm²·s⁻¹ at < 200 °C. (f) Kinetic Monte Carlo simulation of out-diffusion of H₂O in a-IGZO.

Figure 1.12 (a) The variations of free electron concentration (n) with the temperature (T), and the Cu concentration in crystalline ZnO. (b) Formation energy of oxygen vacancy (V_O) and Cu vacancy (V_{Cu}) in Cu₂O and CuAlO₂ with respect to Fermi energy level. (c) Chemical bond between an oxide ion and a cation that has a closed-shell electronic configuration in crystalline Cu₂O.

Figure 1.13 (a) Energy dispersive spectroscopy of the CuMn/a-IGZO interfaces after annealing at 250 °C for 1 h in air. (b) The changes of DOS in a-IGZO with respect to dipping time on 0.05 M CuSO₄ solution. (c) SIMS depth profile of the Cu/a-IGZO interfaces after annealing at 250 °C for 1 h in air. (d) Area mapping of the Cu concentration in ZTO surface with/without Ta-interfacial layer. (e) The changes in transfer curves of a-IGZO TFTs after voltage sweep to 20.1 V. subthreshold slope increases and turn-on voltage decreases. (f) Schematic diagram of Cu-doped a-IGZO/a-IGZO TFTs. (g) Cross-sectional schematics of a-IGZO TFTs composed of Cu gate electrodes.

Figure 1.14 (a) Schematics of defect reactions of Cu in Si: A. formation of point defects and their complexes, B. Cu silicide precipitates in the bulk, C. decoration of existing extended defects, D. out-diffusion to the surface, and E. segregation. (b) Illustration of Cu migration in the nMOSFETs which are turn-on state under 300 °C.

Figure 1.15 Observation of Ag electrochemical migration in SiO₂. Ag ions not only drift toward the Pt electrode affected by electric field, but also are oxidized in SiO₂.

Figure 1.16 Overview of the thesis.

Figure 2.1 (a) Schematics of changes in electronic band structure with respect to structural disorder and chemical disorder. These schematics are modified from refs. 1.49 and 2.1. (b) Calculated density of states (DOS) in amorphous Cd-Ge-O. (c) DOS model for a-IGZO. Solid curves within the bandgap represent the exponentially distributed band-tail states, while the dash curve near the E_C represents the Gaussian-distributed donor-like V_O state.

Figure 2.2 (a) Schematic sketch of the total DOS of AOSs. D_0 and O_{UC} denote Individual local O deficiencies and undercoordinated O, respectively. (b) Running coordination numbers of In with O in crystalline and amorphous $InGaZnO_4$. (c) Integrated conduction electron charge inside the Wigner-Seitz volume around the In atoms as a function of the In coordination number. The best In atom that trap free electrons is denoted as In^* . (d) Transition of atomic structure forming $(In^*-M)^{2-}$ center.

Figure 2.3 (a) Subgap states above valence band (VB) maximum due to undercoordinated O. These localized deep levels are annihilated. after H is doped. It would be induced by hydrogenation. Thus, O-H bonds are additionally formed, results in fully coordination of O. (b) a-IGZO films deposited on O rich and deficient conditions (top) and HXPES spectra of the corresponding films. (c) HXPES results in a-IGZO thin films according to post-deposition annealing conditions. Wet annealing was conducted at 400 C for 1 h under H_2O partial pressure of 0.2 atm.

Figure 2.4 (a) Transfer characteristics of a-IGZO TFTs with respect to annealing at 50-300 °C for 15 min. under O₃ ambient. (b) TDS spectra of O₂ for a-IGZO thin-films subjected to different post-deposition annealing processes. (c) Dynamic changes in electronic states of O_{wb} according to gate voltage and photon energy. (d) Effect of monochromated photon energy on transfer characteristics changes in a-IGZO TFTs that underwent high gate voltage. All figures are bring from ref. 2.10.

Figure 2.5 (a) Ca dopant form Ca-O bonds with O_{wb}S, results in decrease of O_{wb} density. (b) Transfer curves of thin-film transistors (TFTs) composed of Si-doped In-O. Doping concentration of Si is varied from 3 (ISO3) to 10 at% (ISO10). The TFTs stored in vacuum (~10 Pa) for 3 months. Subsequently, the TFTs were exposed to air for 2 weeks. (c) The changes in Fermi energy (E_F) of Si-doped In-O TFTs with respect to gate bias voltage (V_{GS}) as well as ambient atmosphere (vacuum or air). After storing it in vacuum, E_F shifts above the mobility edge (E_m) due to desorption of O_{wb}. After exposing to air, E_F was changed back to the line plotted in blue because O_{wb} sneak in the oxides.

Figure 2.6 (a) Contour plot of wavefunction and (b) total and partial DOS in a-IGZO with one neutral interstitial Oi⁰. (c) The changes of DOS in Figure 2.6b when 2 H atoms are added in close to Oi⁰. All figures are bring from ref. 2.13.

- Figure 2.7** Summary of candidate chemical disorder (i.e., defects) composed of subgap states in AOSs.
- Figure 2.8** (a) Isoconfigurational viscosities of amorphous Pd-Si. (b) The temperature dependence of the rate of viscosity changes. (c) Densification of amorphous silica powder at 775 °C.
- Figure 2.9** Basic electrical conduction in metal/semiconductor/metal structures modified from refs. 2.16-2.24.
- Figure 2.10** Transition of dominant conduction mechanisms from Ohmic to P-F with respect to the magnitude of electric field.
- Figure 2.11** SCLC in Cr/ZrO₂/heavy doped-Si structure.
- Figure 2.12** (a) Circuit symbol of memristor or RS devices. (b) metal/metal oxides/metal structure for RS devices. In addition to metal oxides, various insulating (or semiconducting) materials show RS behavior. (c) Schematics of crossbar circuits composed of RS devices per one cell.
- Figure 2.13** (a) Schematics of 3-dimensional crossbar array using RS devices in terms of vertical stacking (left) and horizontal stacking (right) of word lines. (b) Demonstrated performance and required performance for representative applications of RS devices.

Figure 2.13 (a) RS mode: unipolar and bipolar. (b) Current-voltage characteristics of a Cu/SiO₂/Pt structured devices.

Figure 2.14 (a) In-situ transmission electron microscopy (TEM) images and the corresponding current-voltage characteristics of Pt/ZnO/Pt devices. (b) Energy band diagram presents the modulation of Schottky barrier height due to formation of O-deficient interfacial layer at Pt/TiO₂ interface. (c) Gradual decrease of O concentration (yellow) in GaO_x after RS. Concentration gradient of Ga (red) is not observed. (d) Schematic of electron trapping due to Au nanoparticles in TiO₂.

Figure 2.15 Resistive switching mechanism: conductive filaments formation (forming or SET). Refs. 1.72, 2.29, 2.31, 2.35-2.44 were considered.

Figure 2.16 Resistive switching mechanism: conductive filaments dissolution (RESET). Refs. 1.72, 2.29, 2.31, 2.35-2.44 were considered.

Figure 2.17 (a) *I-V* characteristics of ITO/xHTPA/Ca/Al devices with and without Au NPs. (b) Au NPs inclusion in xHTPA. Images are obtained by high-resolution dark-field TEM. (c) Formation of high-field domain in a voltage-controlled NDR. (d) RS characteristics of polystyrene (PS) with respect to weight percent of phenyl-C61 butyric acid methyl ester (PCBM) clusters.

Figure 3.1 Schematics of the plane view of the devices at each process step.

Figure 3.2 (a) Plain optical image and (b) cross-sectional TEM images of the devices in the as-fabricated state.

Figure 4.3 Schematic structure of multi-layer thin films to measure (a) composition profile with chemical states, (b) roughness, (c) density, and (d) optical properties of a-IGZO thin films.

Figure 3.4 (a) Schematic of the plane view of the van der Pauw samples at each process step. (b) Plain optical image of van der Pauw sample.

Figure 3.5 (a) Probe station used in this study. (b) Agilent 4156C semiconductor parameter analyzer. (c) Qualitau MIRA EM tester (C6020).

Figure 4.1 (a) AFM results of the as-deposited a-IGZO thin-films on the same substrate as the devices (top) and photographs of the 1-cm wide samples (bottom). (b) XRR spectra of IGZO thin-films deposited on Si wafers, which shows that the density of both the 40-nm and 160-nm-thick a-IGZO films is $5.8 \text{ g}\cdot\text{cm}^{-3}$.

Figure 4.2 (a) Transmittance (T), reflectance (R), and (b) optical absorption spectra (α) of 160-nm-thick a-IGZO thin films deposited on quartz glass ($3 \times 3 \text{ cm}^2$).

- Figure 4.3** Schematic structure of the devices prevent extrinsic reactions used in this work. A cross-sectional TEM image of the devices in the as-fabricated state is also shown.
- Figure 4.4** Gibbs free energy of oxide formation of In, Ga, Zn, Cu, and W.
- Figure 4.5** High-resolution TEM images and fast Fourier transform (FFT) diffractograms of the devices in the as-fabricated state (middle), after annealing at 400 °C for 1 h (left), and after annealing at 450 °C for 9 h (right). The FFT analysis area is marked by the white-dotted line.
- Figure 4.6** Magnified high-angle annular dark-field scanning TEM images (top) and EDS composition profiles of the devices along the arrow in the TEM images (bottom).
- Figure 4.7** Composition XPS profiles of the Ta-Al/W/a-IGZO/W-Ta-Al thin films in the as-fabricated state (left) and after annealing at 450 °C for 9 h (right).
- Figure 4.8** XPS results of O (V_O), In, Ga, Zn, and W in a-IGZO thin films. The location of each XPS data point in the depth profiles was marked in Figure 4.7(1→10 or 1→15). The XPS peaks are cited from refs. [1.36,4.7-4.11].

Figure 4.9 (a) Typical I - V characteristics of the devices with Ta-Al layer and the device without Ta-Al in the as-fabricated state. (b) Schottky diode parameters for the devices: Schottky barrier (Φ_B), ideality factor (n), and series resistance (R_S).

Figure 4.10 (a) Schematic energy band diagram of the W/a-IGZO/W structures. (b) The variation in V_{bi} and W_D with respect to N_D in a-IGZO thin films at RT.

Figure 4.11 The changes in the (a) I - V characteristics and (b-c) electrical conductance in the devices without Ta-Al and with Ta-Al with respect to ambient atmosphere as well as annealing time at 450 °C.

Figure 4.12 Plain optical images of the devices after at 450 °C for 9 h under N₂/O₂ ambient.

Figure 5.1 The representative current-voltage (I - V) characteristics of the devices in the as-fabricated state and after annealing at 300 °C for 1 h (measured at RT). In the as-fabricated state, rectifying I-V curves are observed even though the devices have a symmetric structure. After annealing at 300 °C for 1 h, counter figure-eight hysteretic I - V curves are observed in the voltage range from -1 to 1 V.

Figure 5.2 The changes in the I - V characteristics of the devices in the as-fabricated state as a function of the voltage sweep range (measured at RT). In the voltage sweep range of -3 V to 3 V, a counter figure-eight hysteretic loop is clearly observed. As the voltage sweep range increases, the hysteresis area increases.

Figure 5.3 I - V map of the devices considering both the annealing temperatures from 300 to 450 °C and the annealing times from 1 to 16 h. The contact area of the devices was 25 μm^2 . After annealing at 300 °C, the rectifying and hysteretic behaviors with similar electrical conductance are observed even after the annealing time of 16 h. After annealing at 400 °C, the hysteresis disappears with an increase in the electrical conductance, and the I - V curves become symmetric as the annealing time increases. When the I - V curves become symmetric, the I - V characteristics are nearly constant regardless of further annealing. After annealing at 450 °C, symmetric I - V curves are observed even after an annealing time of 1 h.

Figure 5.4 The variations in the Schottky diode parameters in the devices after annealing at 300-400 °C: Schottky barrier (Φ_B), ideality factor (n), and series resistance (R_s) at RT. The contact area of the devices was 25 μm^2 .

- Figure 5.5** Dependence of the reverse current (I_{REVERSE}), Φ_B , and the concentration of positively charged defects in the depletion region of a-IGZO (N_D) on the contact area (left) and temperature (right).
- Figure 5.6** (a) Double logarithmic I - V plots and the slope of the corresponding plots to determine the Ohmic conduction. (b) $\text{Log}(I/V)$ - $E^{0.5}$ plots to identify the P-F conduction.
- Figure 5.7** Representative I - V characteristics of the devices after annealing at 450 °C for 9 h. (a) semi-logarithmic plot, (b) double-logarithmic plot, and (c) the slope of the corresponding double-logarithmic I - V curve.
- Figure 5.8** Arrhenius plots of (a) Ohmic resistance and (b) the current at $E=62.5$ kV/cm with the P-F parameter, r .
- Figure 5.9** The changes in the free electron concentration (n_e) and shallow-donor energy level (E_C-E_D) of V_{OS} in a-IGZO after annealing at 400 and 450 °C.
- Figure 5.10** Cumulative distribution of the electrical parameters of the devices following the method described in the JEDEC standard JESD 37. , I_{REVERSE} , and N_{DS} (or N_D) of the Schottky conducting devices (a) after annealing at 300 °C and (b) after annealing at 400 °C. (c) n_e , E_C-E_D , and N_{DS} of the devices that show Ohmic and Poole-Frenkel conduction at low and high voltages, respectively.

Figure 5.11 The V_O concentration at the shallow-donor state (N_{DS}) in a-IGZO with respect to post-fabrication annealing conditions.

Figure 5.12 N_{DS} values in a-IGZO for the 40-nm devices with respect to post-fabrication annealing conditions.

Figure 5.13 Thickness changes in a-IGZO thin-film patches after annealing at 450 °C for 9 h. 6.2% thickness reduction was observed by HRTEM.

Figure 5.14 Illustrations of the (a) atomic rearrangement of a-IGZO in the devices and (b) the change of density of states (DOS) in a-IGZO due to SR. The configuration of DOS in a-IGZO in the as-fabricated state was obtained from refs. 1.3 and 2.10.

Figure 5.15 Schematics of the cross-sectional view of the devices. Because the devices are designed to prevent extrinsic reactions, three different capacitors [(1) Schottky diode, (2) MOS capacitor, and (3) MOM capacitor] are connected in parallel.

Figure 5.16 Schematic energy band diagrams of the capacitors. High-quality Ohmic contacts are not formed at TE/a-IGZO interfaces.

Figure 5.17 Equivalent circuits of the device. Interfacial capacitance at the TE/a-IGZO contact may also affect the C characteristics of the devices in addition to the Schottky diodes, MOS capacitors, and MOM capacitors.

Figure 5.18 Changes of W_D in a-IGZO thin-film patches (bottom), C of MOM, MOS capacitors and Schottky diodes (middle), and A^2/C^2 in the devices with respect to applied bias (top) (a) N_D of $1.0 \times 10^{17} \text{ cm}^{-3}$ and of 0.37 eV. (b) N_D of $1.2 \times 10^{16} \text{ cm}^{-3}$ and Φ_B of 0.50 eV. The total C of the devices is significantly affected by the MOM and MOS capacitances which are comparable or larger than C of the Schottky diodes. Therefore, the values of N_D and Φ_B extracted from the A^2/C^2 - V curves are inaccurate.

Figure 5.19 (a) I - V and the corresponding (b) C - V characteristics of the as-fabricated devices with regard to contact area (measured at RT and an AC frequency of 1 MHz). The inset in Figure 5.19a shows the contact area dependence of the electrical conductance at ± 1 V. (c) A^2/C^2 - V plots to extract N_D and Φ_B .

Figure 5.20 I - V , C - V , and A^2/C^2 - V results in the devices after annealing (a) at 300 °C for 1 h and (b) at 400 °C for 1 h. (c) Frequency dependence of C - V characteristics in the devices.

Figure 5.21 Representative I - V curves of the devices in the as-fabricated state with respect to the O partial pressure during a-IGZO thin-film deposition. Base pressure (10^{-5} Pa) and working pressure (0.5 Pa) conditions were same.

Figure 6.1 Schematic structure of the W devices and the Cu devices composed of 40-nm-thick a-IGZO thin-film patches. A cross-sectional TEM image of the Cu devices in the as-fabricated state is shown as well.

Figure 6.2 The representative I - V characteristics in the as-fabricated devices (measured at RT). Both devices show rectifying I - V behaviors.

Figure 6.3 I - V map of the devices considering the both annealing temperature from 300 to 500 °C and the annealing time from 1 to 100 h. Contact area of the devices is 25 μm^2 .

Figure 6.4 Electrical conductance (G) of the devices. I - V characteristics as well as G of the W devices is strongly affected by annealing temperature, but not on the annealing time. However, I - V characteristics and G of the Cu devices is altered by annealing time as well as annealing temperature.

Figure 6.5 The variations of Φ_B , n , and N_D in the Schottky conducting devices with respect to annealing conditions.

Figure 6.6 $\text{Log}(I/V)-E^{0.5}$ plots of the Cu devices after annealing at 400-500 °C to identify the P-F conduction..

Figure 6.7 (a) P-F fitting results; P-F parameter, r . (b) Substrate temperature dependence of electrical conductance of the Cu devices after annealing at 450 °C for 16 h at $E=100$ kV/cm.

Figure 6.8 Electrical breakdown characteristics. The Cu devices showed hard breakdown in the as-fabricated state and after annealing at 300 °C for up to 9 h. However, RS behavior is observed after annealing time of 16 h.

Figure 6.9 (a) Electrical breakdown characteristics of the W devices after annealing at 300 °C. (b) Contact area and (c) temperature dependence of resistance of the Cu devices after annealing at 300 °C for 100 h. The resistance values of the electrically-broken W devices with respect to substrate temperature are also included. (d) The DOS changes in stoichiometric a-IGZO due to Cu inclusion at the free volume.

Figure 6.10 The DOS changes in stoichiometric a-IGZO due to Cu inclusion at the substitutional sites (i.e., In, Ga, or Zn).

Figure 6.11 (a) Breakdown voltage of the Cu devices and the W devices. (b) Electrical breakdown characteristics of the W devices after annealing at 400 °C

Figure 6.12 Resistive switching characteristics in the Cu devices after annealing at 400 °C for 1 h and 16 h with respect to operating bias polarity.

Figure 6.13 Cumulative distributions of the electrical resistance at LRS/HRS, SET/RESET voltage, and RESET power.

Figure 6.14 HAADF-STEM images, EDS map, HRTEM images, and FFT diffractograms of the devices with respect to annealing conditions. Scale bar, 10 nm. After annealing at 400 °C for 1 h, Cu diffusion was not detected. However, Cu-rich clusters are observed after annealing time of 16 h. As annealing temperature increases to 500 °C, Cu-rich clusters are observed even after annealing time of 1 h, whereas a-IGZO in the W devices maintain amorphous phase without inter-diffusion. Diffraction patterns indicate that Cu-rich clusters are Cu-In-O clusters.

Figure 6.15 SIMS analysis of Cu/a-IGZO interfaces with respect to annealing conditions. Among In, Ga, and Zn, In is dominantly inter-diffused with Cu.

Figure 6.16 (a) Composition XPS profiles of the Ta-Al/Cu/a-IGZO/W/Ta-Al thin films in the as-fabricated state (top) and after annealing at 500 °C for 1 h (bottom). XPS results of (b) Cu, (c) In, (d) Ga, (e) Zn, and (f) O (V_O). (g) XPS peak shift of the elements after the annealing.

Figure 6.17 Cu doping kinetics in a-IGZO. (a) C atomic movement in the Cu devices according to annealing conditions. (b) Potential energy diagram of Cu diffusion. (c) Composition profile changes in Cu/a-IGZO contacts.

Figure 7.1 Schematics of atomic rearrangement during structural relaxation in AOSs. Reduction in density of O_{wb} as well as M_{uc} would be dominant mechanism of SR-driven doping.

Figure 7.2 (a) Co-deposition process of AOSs with Cu. (b) Application of *p*-type $Ge_2Sb_2Te_5$ on the counter electrode. (b) CF growth dynamics determined by kinetic parameters: ion mobility and redox rate.

CHAPTER 1

Introduction

1.1. Amorphous oxide semiconductor-based electronic devices

Megatrend of electronic devices could be claimed that the electronics evolve to have various characteristics, not only high-density and high-performance but also large-area uniform, mechanically flexible, transparent in visible region, low-temperature process capable, and ultimately recyclable^[1.1-1.5]. To implement such new generation electronic devices, advanced materials compared to conventional *crystalline* semiconductors (e.g., Si) are needed^[1.1-1.5].

Amorphous oxide semiconductors (AOSs) have been considered as one of the most promising materials for implementation of next-generation device platforms due to their novel properties, which originate from short range atomic ordering the characteristics of ionic bonding based on heavy post transition metal cations^[1.6-1.8]. Long-range disordering ironically gives rise to long-range uniform electrical properties of AOSs thin-films. Absence of dislocation and grain boundary enhance the mechanical flexibility of AOSs compared to the corresponding *crystalline* oxides. Moreover, AOSs show fast electron mobility ($> 10 \text{ cm}^2\text{V}^{-1}\text{s}^{-1}$) comparable to the corresponding crystalline

oxides and is superior to another candidate amorphous semiconductors such as amorphous Si, amorphous chalcogenides, and organic semiconductors even if they are fabricated at low temperature including room temperature due to ionic bonding characteristics based on metal cations with $(n-1)d^{10}ns^0$ ($n \geq 5$) electron configuration (**Figure 1.1a**). Conduction band minimum (CBM), which is dominant electron transport path, of ionic oxide semiconductors is mainly composed of metal ns orbital with spherical shape (**Figure 1.1b**). Because the magnitude of overlap among metal ns orbitals is weakly affected by structural disorder, ionic oxide semiconductors maintain fast electron mobility even when amorphization occurs^[1,6-1.8].

Figures 1.1c-1.1h shows an application of AOSs on various electronic devices. Mechanically flexible AOSs thin-film transistors (TFTs) are now used in current flat-panel displays such as smart-phones, e-paper, larger-area LCD as well as organic light-emitting diode (OLED) displays^[1.3,1-9]. Moreover, because most of AOSs have wide band gap (> 3 eV), AOSs have attracted great interest for development of transparent TFTs in next generation display such as smart window and transparent electronic wall^[1.5]. In addition to TFTs for displays, AOSs TFTs are integrated with low-temperature fabricated non-volatile memory and implement CMOS logic circuits^[1.10-1.12]. Phototransistors for image sensors^[1.4] and Schottky diodes for microwave circuits in flexible mobile phones^[1.13] have been developed based on AOSs. Thus, AOSs are fundamental materials for future transparent and flexible device platforms of internet of things (IoT) as shown in **Figure 1.1i**^[1.4].

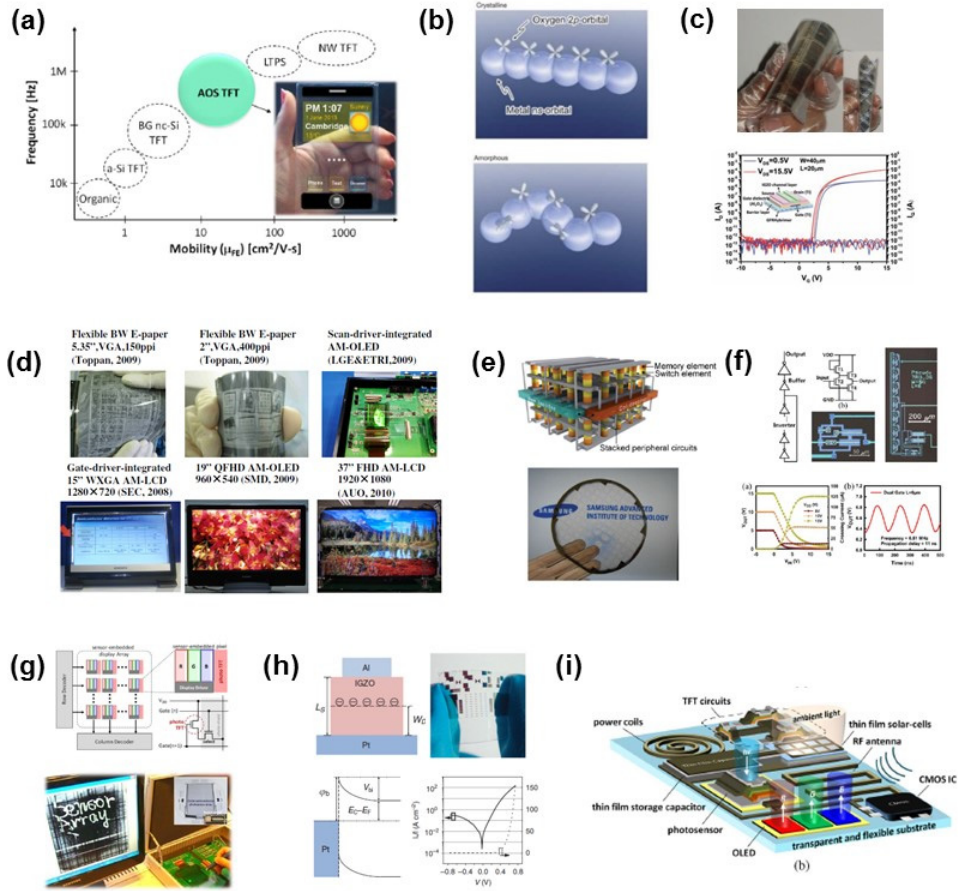


Figure 1.1 (a) Mobility and frequency capability of materials for TFTs^[1.4]. (b) Schematic drawings of metal s orbitals in ionic oxide semiconductors^[1.2]. Applications of AOSs on various electronic devices: (c) flexible AOSs TFTs^[1.9], (d) AOSs TFTs-based displays^[1.3], (e) integration with non-volatile memory^[1.10], (f) AOSs TFTs-based CMOS circuits^[1.12], (g) touch-free image sensors based on AOSs photo transistors^[1.4], and (h) flexible Schottky diodes for high-frequency mobile phones^[1.13]. (i) Illustration of future transparent and flexible systems of IoT^[1.4].

However, further improvement of electrical performance as well as long-term stability in AOSs-based electronic devices is still required to show real market place^[1.14-1.18]. Although various factors such as device structure and interconnecting materials affect electrical performance and long-term stability of the devices^[1.14,1.17,1.18], enhancement of electrical properties and stability of AOSs is primarily required. Doping control in AOSs would be the most fundamental solutions for advancement of electrical characteristics in AOSs^[1.19-1.21]. Unfortunately, doping physics in AOSs are not still veiled or debated^[1.22-1.28]. Although, doping could enhance the electrical properties and stability of AOSs, doping efficiency was not consistent according to doping concentration^[1.29-1.31], film density^[1.32], and film deposition power^[1.33]. The following sections describe the details of doping issues in AOSs involving structural disorder and provide an objective of the thesis that unraveling *intrinsic* and *extrinsic* doping mechanism in AOSs for development of novel AOSs.

1.2. Doping issues in amorphous oxide semiconductors

1.2.1. Effect of structural disorder on doping efficiency

Amorphous In-Ga-Zn-O (a-IGZO), which is representative materials for AOSs, was invented based on novel material design by Hosono's group^[1.2,1.6,1.8]. ZnO is base material and In dopants are added to increase electron mobility using large 5s orbitals of In (**Figure 1.2a**)^[1.2,1.6,1.8]. Moreover, Ga dopants are also incorporated in amorphous In-Zn-O (a-IZO) to enhance stability because the Ga ions form stronger chemical bonds with O than Zn and In (**Table 1.1**)^[1.34]. Electrical conductivity of a-IGZO is affected by adsorption/desorption of O, because oxygen vacancy (V_O) acts as *intrinsic* electron donor^[1.2,1.6,1.8]. **Figure 1.2b** shows the aging effect on electrical conductivity of a-IZO and a-IGZO^[1.35]. Electrical conductivity of a-IZO increases, while that of a-IGZO is nearly constant. This result strongly suggests that Ga suppresses formation of excess V_O s in a-IGZO. Moreover, complex structure induced by ternary compositions with different-sized aliovalent cations forms strong amorphous phase^[1.36]; glass transition temperature (T_g) of a-IGZO is around 600 °C.^[1.37] Based on these dopant selection rules, researches about doping in AOSs have been intensively conducted to fabricate more innovative AOSs than a-IGZO in terms of electrical properties as well as stability. **Figure 1.3a** illustrate the possible doping processes in AOSs. Doping has been conducted through incorporation of dopants in the raw material during the film formation (e.g., physical deposition of solid-state target, solution process) or doping after film formation (e.g., ion implantation, diffusion).^[1.20] Up to date, doping materials used to fabricate AOSs are marked in periodic table as shown in **Figure 1.3b**. Electric roles of doping elements in AOSs can be classified as i) electron donor, ii) mobility enhancer,

and iii) stabilizer against thermal-photo stress and ambient. Interfacial *extrinsic* doping have also been conducted to solve surface problems of AOSs during the device fabrication. In these circumstances, important issues, but there have been pay no attention, could be raised as follows.

First, doping efficiency in AOSs is significantly affected by structural disorder in AOSs, which is distinct from CBM in AOSs^[1.7, 1.20, 1.35]. **Figure 1.4** illustrates the possible dopant location in crystalline and amorphous structure. In crystalline structure, most of substitutional dopants are located at periodic position and they yield free charge carriers^[1.7, 1.20]. However, in amorphous structure, substitutional dopants do not remain at the original substitutional positions, and occupy off-center/interstitial positions because of relaxed local atomic structure^[1.20]. Thus, substitutional dopants could not yield charge carriers if local charge neutrality of the constituent ions is maintained (i.e., charge compensation)^[1.7, 1.20, 1.35]. Moreover, dopants have potential to agglomerate at the relatively open space or to form complex compound (i.e., precipitation)^[1.20]. Therefore, dopants in AOSs form various electronic states (e.g., shallow donor, electron trap, or deep donor) with respect to local atomic structure; i.e., various-type-subgap states are formed at electronic structure in AOSs^[1.22, 1.23, 1.27]. As a result, solely intuitive and irregular doping efficiency is observed at AOSs (**Figures 1.5a and 1.5b**)^[1.29-1.31]. Moreover, electrical performance of a-IGZO TFTs is affected by a-IGZO film density^[1.32] and resistivity of a-IGZO thin films is affected by film deposition power, although chemical composition of a-IGZO thin-films is not influenced by film density and film deposition power^[1.33] (**Figures 1.5c and 1.5d**). These results support that the degree of structural disorder significantly affects the doping efficiency as well as subgap states in AOSs.

Second issue is that post annealing process could affect the electronic states of dopants, results in changes of doping efficiency. **Figure 1.6** depicts atomic rearrangement in AOSs/metal contact structure. Amorphous phase is thermodynamically metastable phase. Therefore, the degree of structural disorder in AOSs is always apt to decrease to form more stable structure as internal atomic rearrangement occurs even below the T_g . This process is also known as structural relaxation (SR)^[1.37-1.40]. It means that SR may induce the changes in electronic states of *intrinsic* dopants. Moreover, when *extrinsic* doping occurs by diffusion, SR simultaneously occurs. Diffusion of *extrinsic* dopant occurs through two path, interstitial site (i.e., free volume in amorphous solid) and substitutional site.^[1.41] Migration behavior and structural location of *extrinsic* dopants is altered by the degree of structural disorder. Because SR decreases free volume size and changes local structure of substitutional site, doping efficiency as well as electronic states of extrinsic dopants also affected by SR.

Since post-annealing processes (**Figure 1.7a**) drastically improve electrical performance as well as stability of AOSs-based devices (e.g., TFTs), post-annealing processes have been considered as inevitable process for fabrication of AOSs-based devices, not only solution-deposition process (**Figure 1.7b**)^[1.36] but also vacuum-deposition process (**Figures 1.7c-1.7f**)^[1.3,1.42-1.44]. During annealing at below T_g , electronic states of dopants are changed due to SR, which may affect improvement of electrical performance as well as stability of the devices (**Figure 1.7e**)^[1.35,1.43,1.45]. However, effect of thermal-driven the changes in electronic state of dopants could not be clearly identified, because subsequent *extrinsic* reactions, such as redox reactions, also occurred during annealing and may contribute to the improvement (**Figures 1.8a-1.8c**)^[1.44-1.47]. Therefore, understanding thermally driven *intrinsic* and *extrinsic* doping mechanisms is prerequisite for controlling the electrical properties and stability in AOSs.

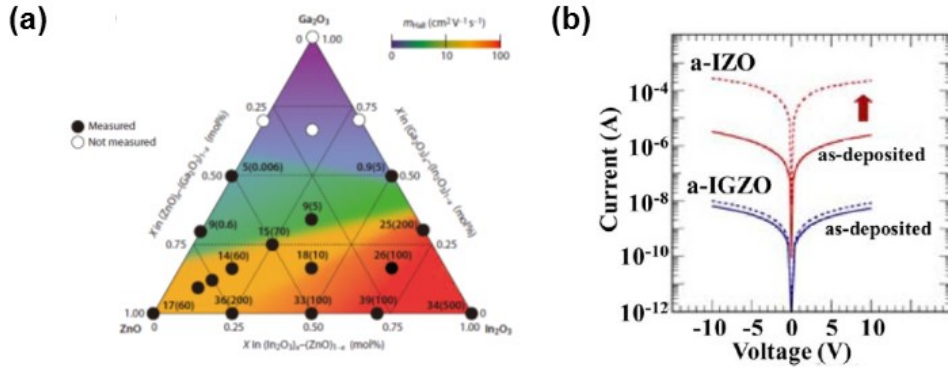


Figure 1.2 (a) Variations in hall mobility of In_2O_3 - Ga_2O_3 - ZnO thin films with respect to chemical composition changes^[1.8]. **(b)** Stability of a-IZO and a-IGZO thin-films after deposition^[1.35].

Metal	Electron configuration	M-O bond energy (eV)	M-O bond length (nm)
In	$[\text{Xe}]5s^24d^{10}$	1.70	0.222
Ga	$[\text{Ar}]4s^23d^{10}4p^1$	2.04	0.202
Zn	$[\text{Ar}]4s^23d^{10}$	1.52	0.205

Table 1.1 Comparison of electron configuration, bonding energy, and bond length of In, Ga, Zn in a-IGZO (InGaZnO_4)^[1.34].

Chapter 1: Introduction

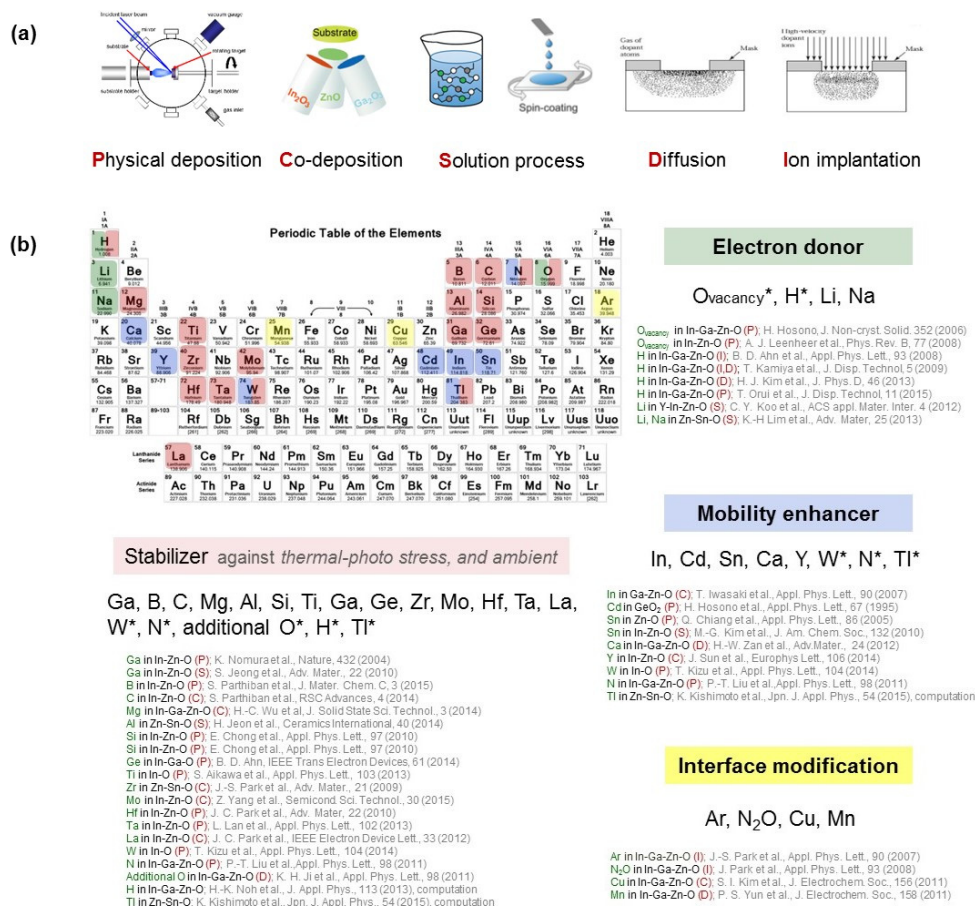


Figure 1.3 (a) Deposition methods of AOSs thin-films and/or doping processes in AOSs^[1,20]. (b) Doping elements in AOSs in terms of electric role.

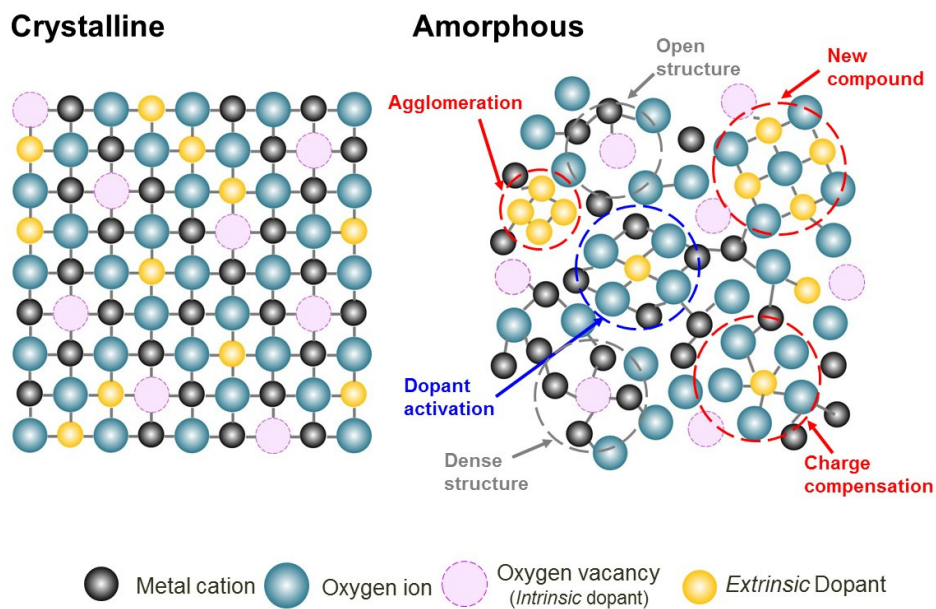


Figure 1.4 Distributions of dopants in semiconductors with respect to phase condition; crystalline or amorphous structure. In amorphous phase, dopants form various local atomic structure. Thus, doping efficiency in AOSs is exceedingly low compared to the corresponding crystalline oxide semiconductors. Moreover, dopants form various electronic states in subgap region.

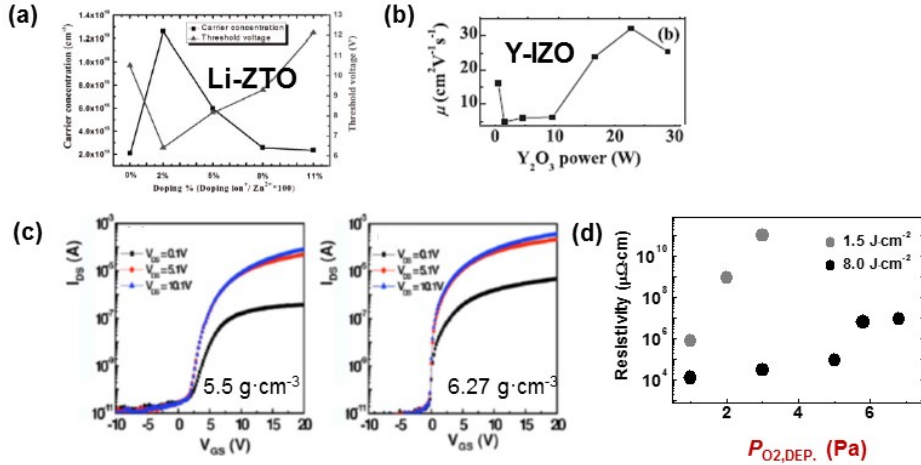


Figure 1.5 (a) Carrier concentration of Li-doped-Zn-Sn-O (Li-ZTO) films and threshold voltage of Li-ZTO TFTs with respect to Li doping concentration^[1.30]. (b) Hall mobility of Y-doped In-Zn-O (Y-IZO) according to deposition power of Y₂O₃^[1.31]. (c) Transfer characteristics of a-IGZO TFTs according to density of a-IGZO thin-films. Chemical composition of In, Ga, and Zn is nearly constant regardless of film density^[1.32]. (d) Resistivity changes in a-IGZO with respect to pulsed laser deposition power and oxygen partial pressure ($P_{O_2,DEP}$) during film deposition. Chemical composition of In, Ga, and Zn is not affected by the deposition power^[1.33].

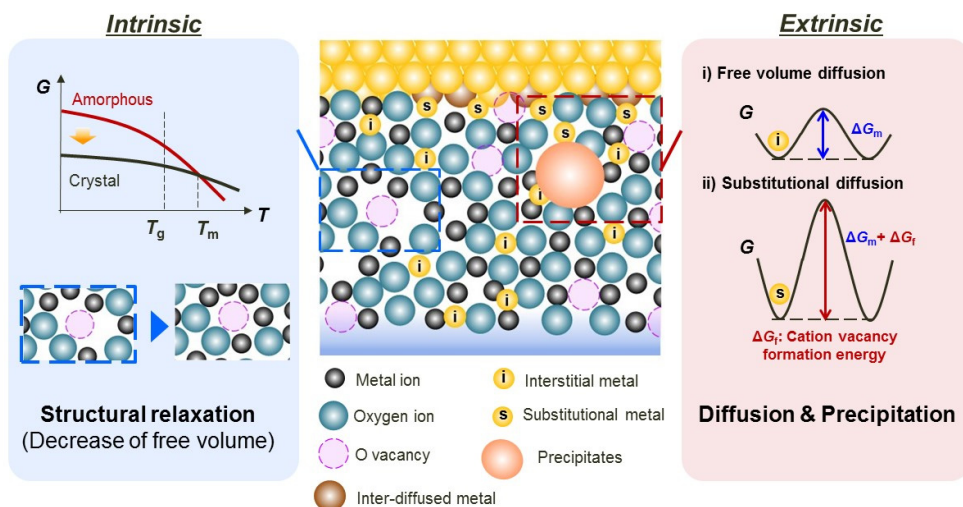


Figure 1.6 Thermally driven atomic rearrangement in AOSs in terms of intrinsic and extrinsic factors.

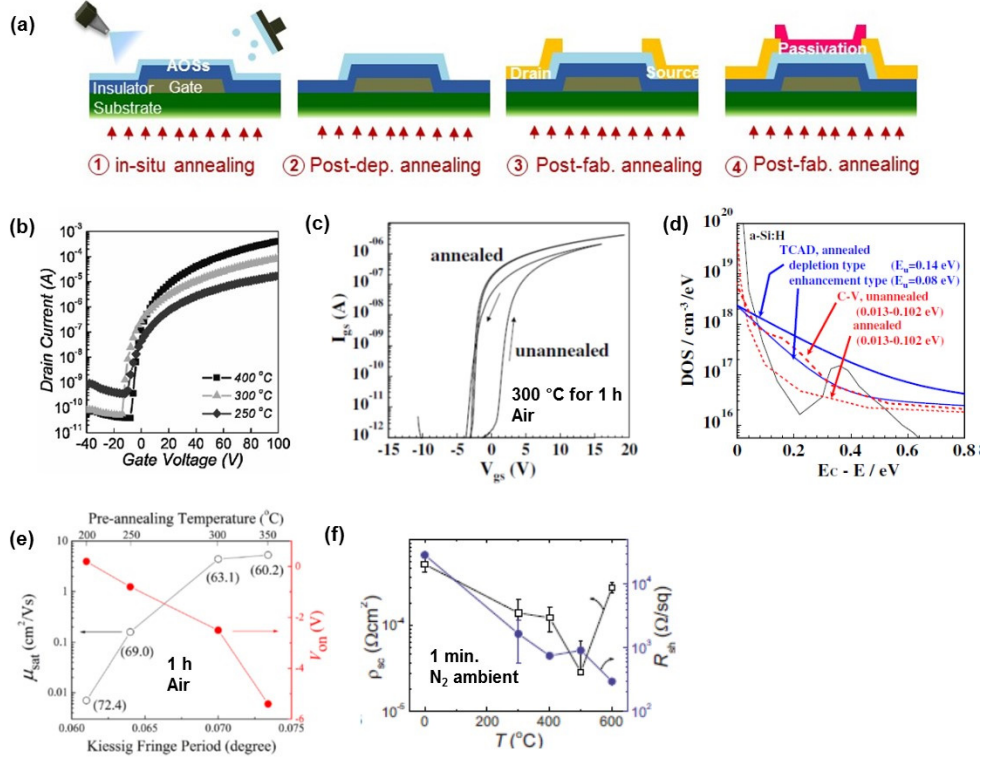


Figure 1.7 (a) Candidate for annealing sequences during TFTs fabrication. Transfer curves of (b) solution-derived a-IGZO TFTs and (b) a-IGZO TFTs based on vacuum-deposition process with respect to annealing temperature^[1.36,1.3,1.42]. (c) Subgap density of states in a-IGZO TFTs (Figure 1.7b) obtained by device simulation (TCAD) and the capacitance-voltage method^[1.3,1.42]. (d) Correlation between the Kiessig fringe periods of the active thin films pre-annealed at various temperatures and their transistor performance of effective mobility and on-voltage. Active material is Si-W-In-O. The data in brackets are the estimated film thickness from the Kiessig fringe periods with unit of nm^[1.43]. (e) contact resistance (ρ_c) and sheet resistance of a-IGZO thin films (R_{sh}). Ti was selected as contact material^[1.44].

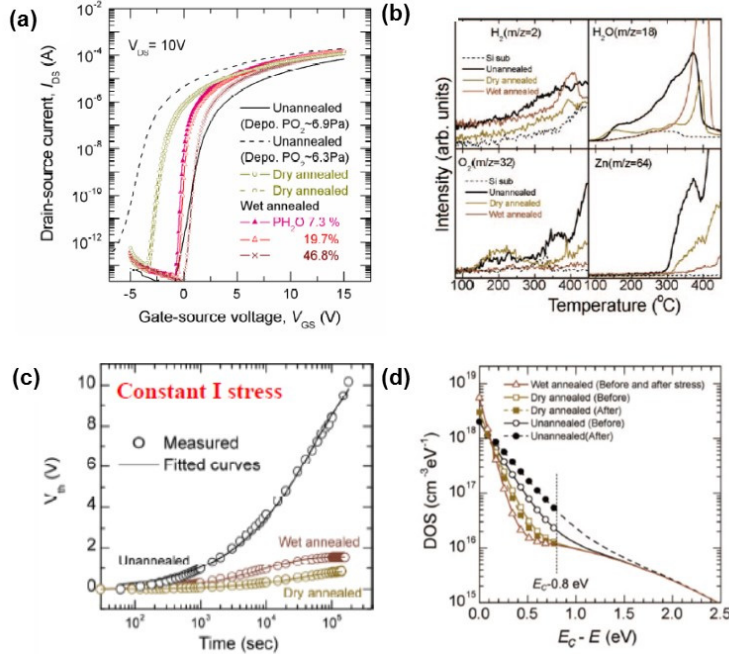


Figure 1.8 (a) Transfer curves of a-IGZO TFTs after annealing at 400 °C for 1 h in dry O_2 and wet O_2 atmosphere at 1 atm. with respect to annealing temperature^[1.45,1.46]. (b) Thermal desorption spectra (TDS) of a-IGZO thin films during annealing from 60 to 700 °C at a heating rate of 60 °C·min⁻¹. Background pressure of vacuum chamber for TDS measurement is around 10⁻⁷ Pa. The magnitude of H_2O , O_2 , Zn is varied among the samples and H_2O , O_2 , and Zn intensively desorb from un-annealed a-IGZO thin films^[1.45,1.46]. (c) Time variations of threshold voltage shift (ΔV_{th}) under constant current (I) stress for a-IGZO TFTs. After annealing in dry O_2 and wet O_2 (19.7% of H_2O), bias stability of a-IGZO TFTs is enhanced^[1.47]. (d) Subgap density of states in a-IGZO TFTs (Figure 1.8) obtained by device simulation (TCAD) and the capacitance-voltage method^[1.47].

1.2.2. Intrinsic doping: oxygen vacancy with hydrogen

Most of AOSs exhibit *n*-type electron conduction and electrical conductivity is modulated by reduction/oxidation reaction control (**Figure 1.5c**) even after film formation^[1.6,1.30,1.33,1.48]. These results indicate that V_{OS} , as inherent chemical defects, act as the dominant electron donors. Interestingly, the V_{OS} can act as deep donors^[1.24] (i.e., limited donation of free electron), electron traps^[1.3,1.22], and shallow donors, whose electronic states are determined by the atomic local environment. **Figure 1.9** shows the schematic model of subgap density of states (DOS) in a-IGZO^[1.3]. Certain researchers have suggested that all V_{OS} in crystalline AOSs are deep donors; however, certain V_{OS} act as shallow donors in a-IGZO when the structural disorder causes weak interactions among metal ions and V_{OS} (i.e., when the bonding distance between a metal ion and V_{OS} increases, called outward relaxation)^[1.24]. Other researchers have suggested that V_{OS} surrounded by a large free volume act as electron traps, whereas the shallow-donor state is formed when a V_O is located in a dense networks (**Figure 1.9b**)^[1.3]. In other words, disagreement exists with regard to which structural condition is responsible for the V_O electronic states. However, the free electron concentration (n_e) in a-IGZO is thought to be affected by the degree of structural disorder in the amorphous phase because the electronic state of V_{OS} changes depending on the degree of structural disorder. **Figure 1.10** presents a schematic illustration of the free volume changes in amorphous solids. T_f is the freezing temperature and T_m is the melting temperature. The difference in the solid volume between the amorphous phase and the crystalline state represents the free volume in the amorphous solid^[1.39]. When amorphous solids are annealed below T_g , SR occurs and the free volume size decreases because internal atomic rearrangement occurs without significant long-range migration^[1.38,1.39,1.49]. Thus,

SR can induce the changes of n_e in AOSs through the changes in the electronic state of V_{OS} . Therefore, understanding the effects of SR on the concentration of V_{OS} in the shallow-donor state (N_{DS}) and n_e in a-IGZO is important for developing device-level a-IGZO applications and reliable resistance to thermal stress. However, only a few studies, if any, exist on the SR effect on either N_{DS} or V_{OS} in a-IGZO^[1.42,1.44,1.47,1.50]. Although there have been reports on the effects of post-depositional annealing on the electrical properties of a-IGZO thin films, our understanding of the SR effect remains insufficient because the interactions with the atmosphere^[1.42,1.47,1.50] and/or metal electrodes^[1.44] during annealing also affect the electrical properties of a-IGZO. (**Figures 1.7e and 1.8**). Therefore, the interaction of a-IGZO with the ambient atmosphere and metal electrodes during thermal annealing should be prevented to ensure that only the SR effect is responsible for changes in the electrical properties of a-IGZO. These points are motivation in development of the devices enable to prevent unwanted extrinsic reactions in addition to SR during annealing in the thesis, **Section 4**.

Remarkable fact is that in addition to V_O , hydrogen (H) could be unintentional *intrinsic* electron donor in AOSs^[1.27,1.45,1.51]. Without inclusion of H_2 gas, doping concentration of hydrogen in a-IGZO thin-films by physical vapor deposition is around 10^{21} cm^{-3} (**Figure 1.11a**)^[1.51]. The source of H is not clear yet but residual H-containing species in the deposition chamber and the sputtering target are candidate^[1.51]. Experimental results that additional H doping by post-deposition annealing and ion implantation induces increase of electrical conductivity as well as n_e support that H act as shallow donor (**Figures 1.11b and 1.11c**)^[1.45]. Structural location of H in the shallow donor state would be free volume (i.e., interstitial H) site or O or V_O site (i.e., substitutional H_O)^[1.34,1.52].

Interestingly, H doping concentration ($\sim 10^{21} \text{ cm}^{-3}$) is much higher than n_e ($\sim 10^{15} \text{ cm}^{-3}$)

³⁾ in AOSs^[1.51]. It means that not all hydrogen act as shallow donor and doping efficiency is critically low or H is not major electron donor in AOSs. Recently, Hosono's group suggest that compensation of H in the shallow donor with weakly-bond O (i.e., excess O) is the origin of low doping efficiency^[1.33,1.45,1.51]. Moreover, Jeong's group reported that H dopant not only acts as shallow donor, but also creates tailing trap state in the vicinity of CBM (**Figure 1.11d**)^[1.27]. Another interesting point is that both interstitial and substitutional H dopant easily diffuse out from AOSs during post-deposition annealing at ≥ 200 °C under low H concentration ambient (e.g., N₂ ambient) as shown in **Figures 1.11e and 1.11f**^[1.27,1.52].

In the thesis, when effect of SR on the electronic states of V_O in a-IGZO is investigated, influence of H dopant on electrical properties of AOSs for is also considered based on the previous report result (**Section 5.6**).

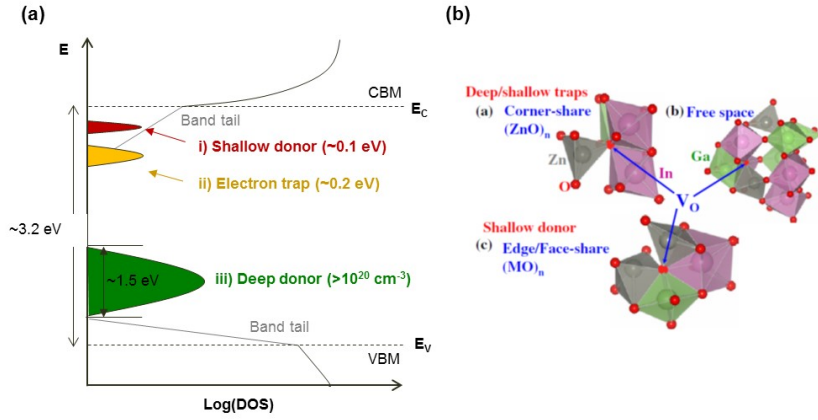


Figure 1.9 (a) Schematics of subgap density of states (DOS) in a-IGZO which is modified from ref. 1.3. (b) Local coordination structures of some oxygen vacancies^[1,3].

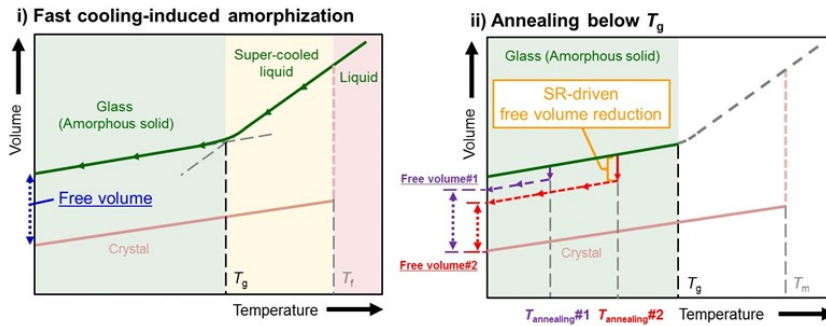


Figure 1.10 Illustration of the free volume changes in amorphous solid during isothermal annealing below T_g .

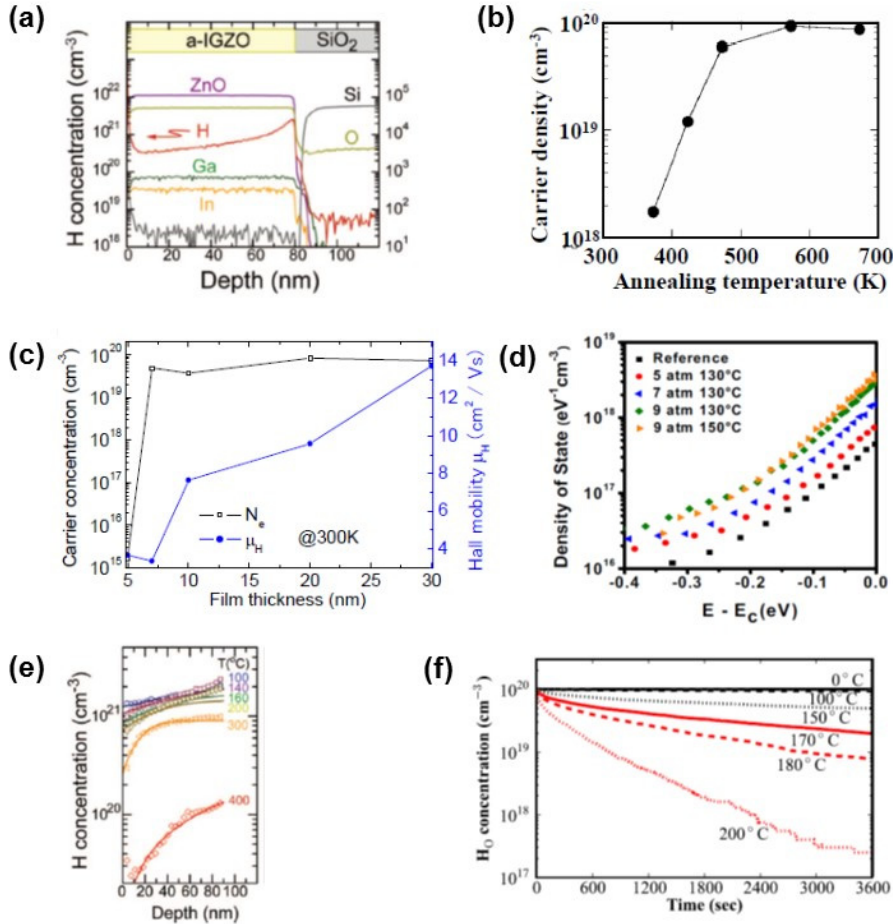


Figure 1.11 (a) Composition profile of a-IGZO measured by secondary ion mass spectroscopy (SIMS)^[1.51]. Electron doping in a-IGZO by (b) annealing in H₂ ambient (3%), and (c) H plasma at RT^[1.45]. (d) The changes of Subgap DOS in a-IGZO TFTs with respect to H₂ high-pressure annealing (HPA) conditions^[1.27]. (e) SIMS depth profile of H in a-IGZO thin-films. Diffusivity of H is $\sim 10^{-14}$ cm²·s⁻¹ at < 200 °C^[1.51]. (f) Kinetic Monte Carlo simulation of out-diffusion of H₂O in a-IGZO^[1.52].

1.2.3. Extrinsic doping: copper

Cu is the vital dopant in *crystalline* metal-oxide semiconductors to modulate the electrical properties, even changing the conduction type from *n*-type to *p*-type (**Figure 1.12a**)^[1.53-1.57]. It has been suggested that Cu suppresses formation of compensating *n*-type defect such as V_O ^[1.57] and enhances the hole mobility as it reduce the localization of valence band maximum (VBM), which is hole conduction path (**Figure 1.12b**)^[1.55,1.56]. Interestingly, *p*-type characteristics of Cu-based oxides are disappeared when the phase of metal oxides become *amorphous* and showed insulating properties^[1.58,1.59]. Various coordination structures in amorphous phase decrease doping efficiency of Cu (**Section 1.2.1**) and non-uniform distribution of Cu may become severe in multicomponent AOSs due to its structural and compositional complexity^[1.60]. If then, what is the exact electronic state of Cu dopants in AOSs?

Up to date, investigation of Cu doping effect on the electrical properties of AOSs has been solely conducted in terms of reliability of the electronics (**Figures 1.13a-1.13d**)^[1.17,1.61-1.64] likewise in the case of conventional semiconductor (e.g., Si, Ge) devices (**Figure 1.14**)^[1.66-1.68] (cf., Cu doping used to form passivation layer on a-IGZO thin-film surface preventing plasma-induced damages as shown in **Figure 1.13e**^[1.69]). Since Cu is frequently used as the interconnect material to reduce resistance-capacitance (R-C) delay at back-end of the line, Cu interconnects have been also applied to AOSs thin-films transistors (TFTs) as shown in **Figure 1.13f**^[1.71,1.61-1.65]. In previous reports, certain researchers suggest that Cu impurity acts as an acceptor-like trap (**Figure 1.13b**)^[1.61-1.63], whereas other research reports that Cu forms donor-like states in the subgap region (**Figure 1.13e**)^[1.64]. Thus, disagreement exists with regard to electronic states of Cu in AOSs, although degradation behavior of AOSs TFTs composed of Cu

electrodes are the basis of deduction in previous researches. When Cu diffusion from Cu electrodes is the dominant origin of the degradation of TFTs, Cu diffusion length should be at least 3 micrometers (i.e., minimum a-IGZO channel length in the reports) enough to affect the degradation of switching performance of TFTs during annealing at below 300 °C for 1 h^[1.62,1.63,1.64]. Based on the equation, $L = \sqrt{D_{\text{Cu}} t}$ (where L is the diffusion length, t the diffusion time, and D_{Cu} the Cu diffusivity in AOSs)^[1.41]. Extracted D_{Cu} value ($>10^{-10} \text{ cm}^2\text{s}^{-1}$) is outrageously high compared to the Cu diffusivity in several amorphous oxides at 300 °C ($\sim 10^{-15} \text{ cm}^2\text{s}^{-1}$)^[1.70,1.71]. Therefore, Cu diffusion may be not dominant origin of the degradation of electrical performance of a-IGZO TFTs and unpredicted factors would cause the degradation during annealing.

Although Jeong et al., suggest that Cu electrochemical migration occurs into a-IGZO channel during voltage sweep, the evidences of Cu electrochemical migration are insufficient enough to estimation of Cu diffusivity in a-IGZO^[1.62]. Moreover, Cu doping driven by electrochemical migration is totally different (**Figures 1.14b and 1.15**)^[1.68,1.72] from Cu doping by diffusion which driving force is purely chemical potential gradient^[1.41]. Thus, Cu doping mechanism as well as electronic states of Cu in a-IGZO have been veiled. Therefore, systematic investigation of Cu doping mechanism in AOSs with respect to various thermal annealing temperature and time is needed to unravel the exact electronic state of Cu in AOSs.

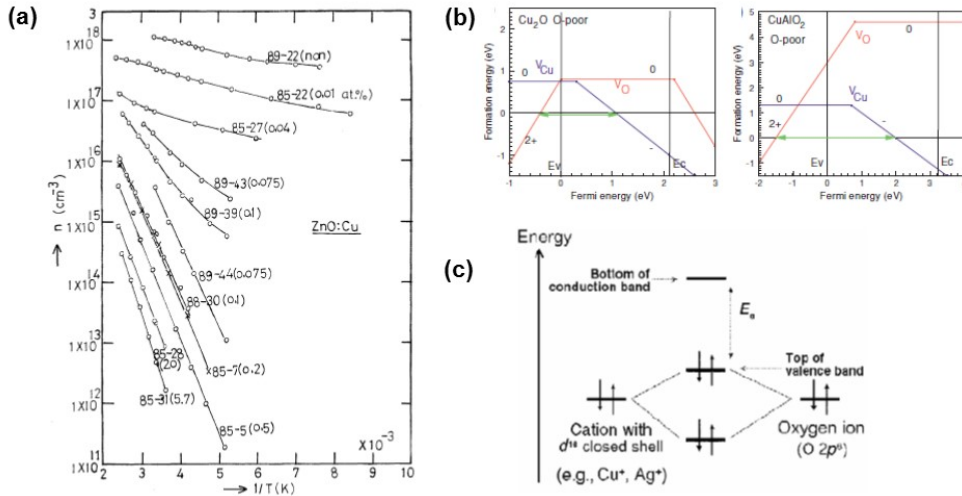


Figure 1.12 (a) The variations of free electron concentration (n) with the temperature (T), and the Cu concentration in crystalline $\text{ZnO}^{[1.53]}$. (b) Formation energy of oxygen vacancy (V_{O}) and Cu vacancy (V_{Cu}) in Cu_2O and CuAlO_2 with respect to Fermi energy level^[1.57]. (c) Chemical bond between an oxide ion and a cation that has a closed-shell electronic configuration in crystalline $\text{Cu}_2\text{O}^{[1.56]}$.

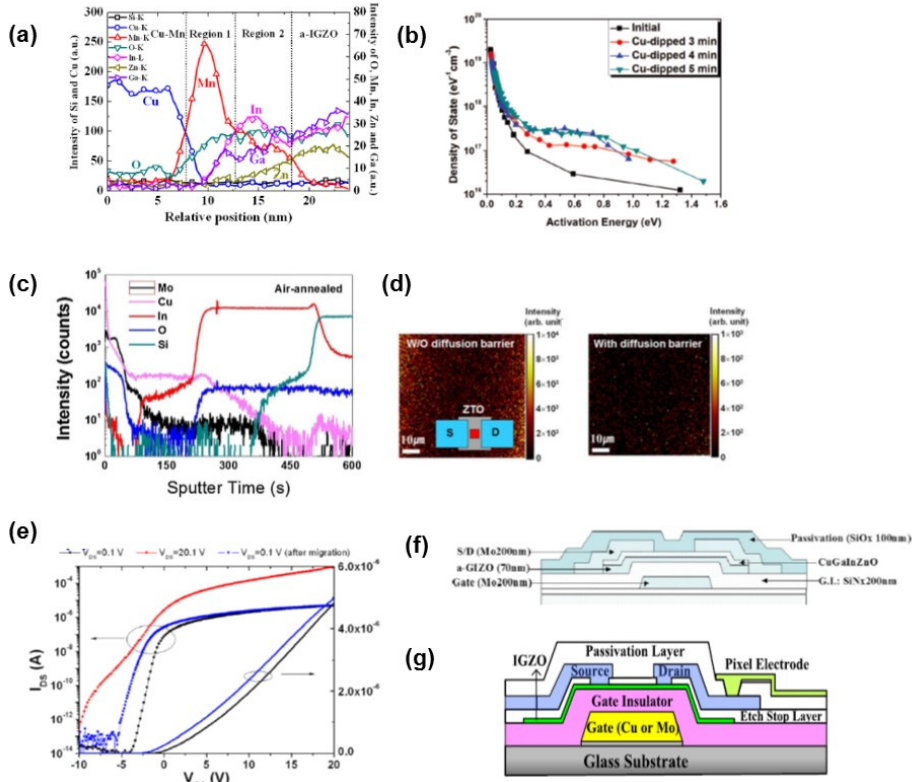


Figure 1.13 (a) Energy dispersive spectroscopy of the CuMn/a-IGZO interfaces after annealing at 250 °C for 1 h in air^[1.60]. (b) The changes of DOS in a-IGZO with respect to dipping time on 0.05 M CuSO_4 solution^[1.62]. (c) SIMS depth profile of the Cu/a-IGZO interfaces after annealing at 250 °C for 1 h in air^[1.63]. (d) Area mapping of the Cu concentration in ZTO surface with/without Ta-interfacial layer^[1.64]. (e) The changes in transfer curves of a-IGZO TFTs after voltage sweep to 20.1 V^[1.65]. subthreshold slope increases and turn-on voltage decreases. (f) Schematic diagram of Cu-doped a-IGZO/a-IGZO TFTs^[1.69]. (g) Cross-sectional schematics of a-IGZO TFTs composed of Cu gate electrodes^[1.17].

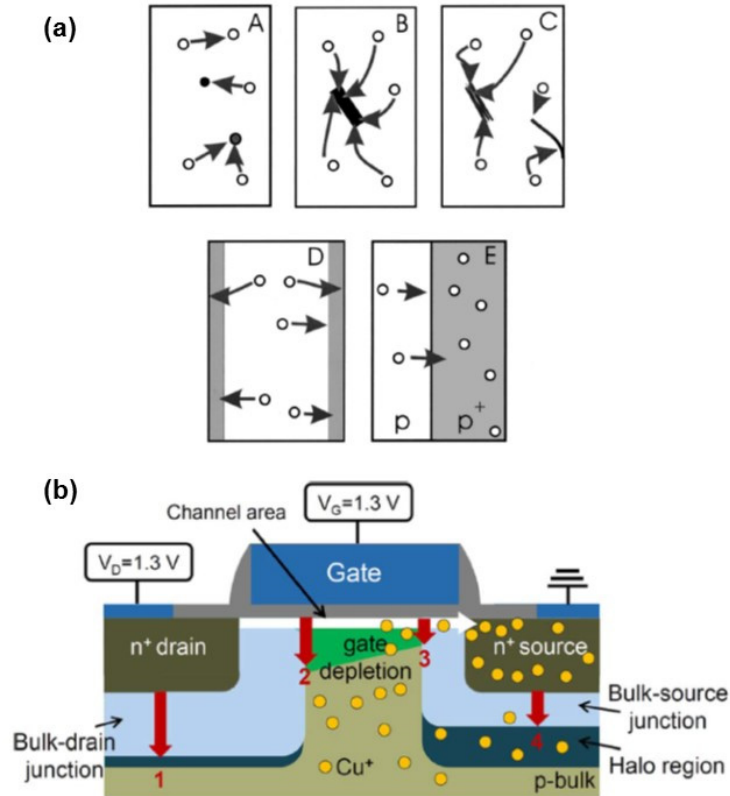


Figure 1.14 (a) Schematics of defect reactions of Cu in Si^[1.67]: A. formation of point defects and their complexes, B. Cu silicide precipitates in the bulk, C. decoration of existing extended defects, D. out-diffusion to the surface, and E. segregation. (b) Illustration of Cu migration in the nMOSFETs which are turn-on state under 300 °C^[1.68].

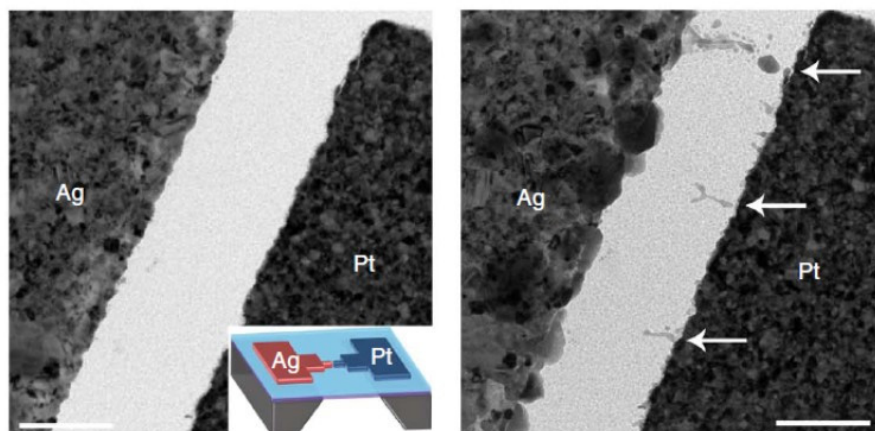


Figure 1.15 Observation of Ag electrochemical migration in SiO_2 ^[1.72]. Ag ions not only drift toward the Pt electrode affected by electric field, but also are oxidized in SiO_2 .

1.3. Objective of the thesis

Ionic amorphous oxides are optimal semiconducting materials for next generation electronic devices due to their structural merits (e.g., long-range uniformity, good mechanical flexibility), superior electron mobility to covalent bonding-based amorphous semiconductors, and high transparency in visible region.

However, the applications of AOSs to electronic devices have been hindered by immature doping processes. Although *intrinsic* and *extrinsic* doping could enhance the electrical properties and stability, controllability of doping effect is poor. Irregular doping efficiency is induced that electronic states of dopants are affected by the degree of structural disorder in AOSs and consequently dopants form various electronic states in subgap region. Moreover, the degree of structural disorder is likely decrease due to SR in amorphous structure. Thus, *intrinsic* and *extrinsic* doping efficiency as well as distribution of subgap states could be altered by thermal history. Therefore, understanding thermally driven doping mechanisms in AOSs is crucial issues for controlling the electrical properties and improvement of stability of AOSs.

The objective of this thesis is to identify the *intrinsic* and *extrinsic* doping mechanisms in AOSs with respect to thermal history and to provide a guideline for obtaining delicate control of electrical properties as well as creation of new functionality in AOSs as depicted in **Figure 1.16**.

The first focus is the development of novel devices that enable to show only the effect of *intrinsic* or *extrinsic* dopant on electrical properties of AOSs. During annealing, redox reactions of AOSs with ambient atmosphere and/or interfacial reactions AOSs with contact materials could occur. These reactions disturb investigation of the doping effects. We designed vertical metal/AOSs/metal structured devices in order to prohibit unwanted

reactions. Gibbs free energy of oxide formation and self-diffusivity of materials are fundamental criteria for material selections in the devices. Various experiments such as microstructural, compositional, optical, and chemical analysis results were conducted to verify the performance of the novel devices. After annealing, interactions of a-IGZO with electrodes and ambient atmosphere are not observed. Based on the novel devices, effects of thermally driven intrinsic and extrinsic doping on electrical properties of AOSs could be clearly identified.

The second focus is to investigate the relationship between electronic states of V_O as an *intrinsic* donor and SR. As annealing temperature increases, doping concentration of a-IGZO increases. Moreover, annealing time weakly affects the doping concentration changes in a-IGZO. Because SR solely occurs during annealing, changes in electronic states of V_O s are the proposed origin of increase of doping concentration. The unprecedented SR-driven doping effect would enable researchers to design and tailor advanced AOSs that exhibit tunable doping concentration *via* SR control. Moreover, strong dependence of SR-driven doping on the annealing temperature rather than the annealing time provides crucial information for achieving corresponding electronic devices that are reliable against thermal stress.

The final focus is to unravel the exact electronic states of *extrinsic* Cu dopants in AOSs. Cu doping mechanism as well as electronic states of Cu in AOSs have been veiled, although Cu have been considered as important impurities for semiconducting materials in terms of *p*-type dopant or factor for deteriorating performance of semiconductor devices. We unprecedently report that dominant electric role of Cu in a-IGZO is dynamically changed with respect to annealing conditions. Moreover, Cu doping generates RS in a-IGZO of which performance are affected by Cu doping

conditions. Cu doping kinetics in a-IGZO are also suggested based on the results of various supplementary experiments in addition to electrical analysis of the devices.

Our study offers a physical understanding of thermally driven *intrinsic* and *extrinsic* doping mechanisms that govern the structural location (i.e., local atomic structure) in AOSs. Moreover, with this results presented in this thesis, we have provided novel methods to investigate doping mechanisms in AOSs and suggested guidelines to develop advanced AOSs devices.

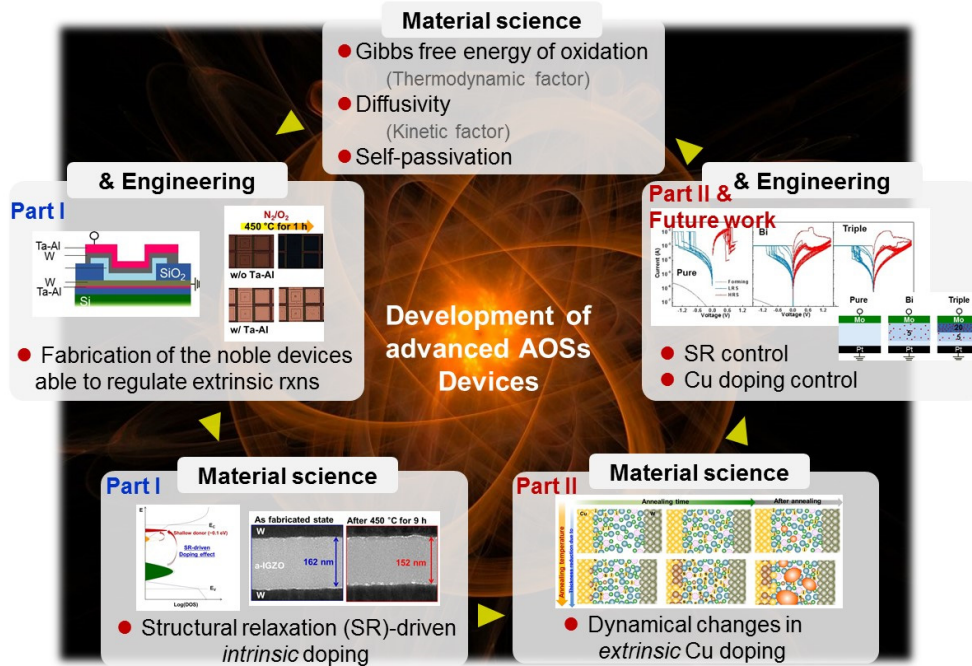


Figure 1.16 Overview of the thesis.

1.4. Organization of the thesis

This thesis consists of seven chapters. In Chapter 2, candidate origin of the subgap states in AOSs are reviewed in terms of structural disorder and chemical disorder. The basic theory of structural relaxation (SR) in amorphous solids, electrical conduction mechanisms in metal/semiconductor/metal structured devices, and redox-based resistive switching is also introduced in Chapter 2. Chapter 3 describes the experimental procedure, including the fabrication of the samples and the methods used for the electrical, optical, microstructural, and chemical investigations. In Chapter 4, development of the novel devices which able to regulate unwanted extrinsic reactions of AOSs is presented. Chapter 5 reports that doping concentration in AOSs is modulated by SR control without redox reactions. Chapter 6 describes the dynamical changes in Cu doping effect on electrical properties of AOSs with respect to annealing conditions. Chapter 7 summarizes the results of this study and suggests future works based on the novel discovery of this study.

CHAPTER 2

Theoretical Background

2.1. Subgap states in amorphous oxide semiconductors

Amorphous materials have various subgap states (i.e., electronic states between VBM and CBM) induced by disorder in amorphous structure. Disorders in amorphous materials can be classified as i) structural disorder and ii) chemical disorder^[1.20,1.49,2.1,]. Interaction of two-types of disorder forms various subgap states. Moreover, subgap states are affected by bonding characteristics (e.g., covalent, metallic, or ionic) of materials^[1.8,2.2]. Subgap states determine electrical and optical properties of amorphous materials^[1.8,1.26,1.49]. However, nature of subgap states in amorphous materials are not fully understood and are still debated, yet^[1.26,2.3,2.4]. Therefore, unravelling the origin of subgap states and modulation of subgap states would be crucial issues for material scientists and engineers. In this section, previous studies that report about subgap states related with structural disorder and chemical disorder are introduced as shown below.

2.1.1. Structural disorder

Figure 2.1a depicts the changes in electronic band structures of materials with respect to structural disorder. CBM is dominantly composed of metal s orbitals, whereas oxygen $2p$ orbitals dominantly forms the VBM^[1.8,2.2,2.5]. As structural disorder increases, localization of band edge increases and move further into the bands. Eventually the whole band is localized^[2.1]. Wide variations in bond length and bond angle give rise to band-tail state. (It is called as “Urbach tail”)^[1.49]. In general, the slope of conduction band tail states (acceptor-like trap) in AOSs is as small as < 20 meV^[2.2,2.5] because CB mainly consists of spherical cation s orbital (**Figure 2.1b**)^[1.6], results in weakly dependent on angle disorder (**Figure 2.1c**). In contrast, a slope of valence band tailing states is 80-100 mV because the VB mainly consists of direction-dependent O $2p$ orbital and is strongly affected by structural disorder (**Figures 2.1b and 2.1c**)^[1.6,2.2,2.5].

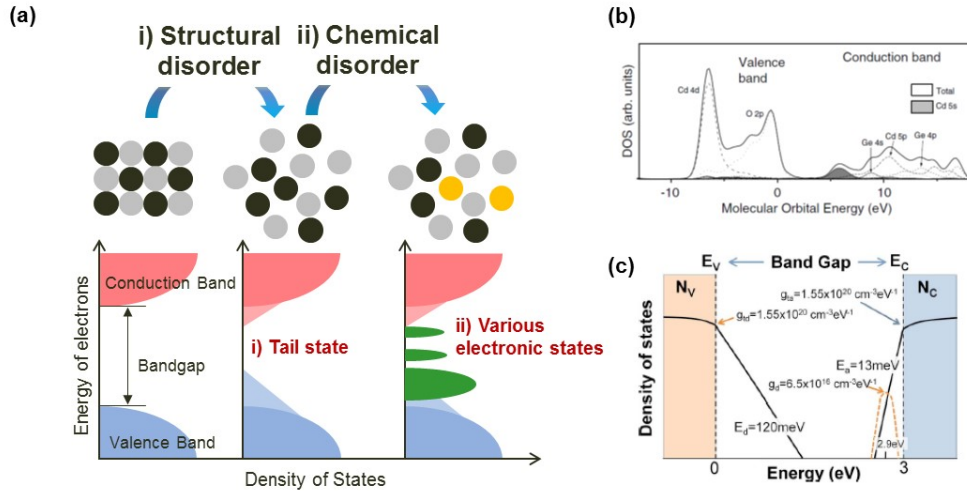


Figure 2.1 (a) Schematics of changes in electronic band structure with respect to structural disorder and chemical disorder. These schematics are modified from refs. 1.49 and 2.1. (b) Calculated density of states (DOS) in amorphous Cd-Ge-O^[1.6]. (c) DOS model for a-IGZO. Solid curves within the bandgap represent the exponentially distributed band-tail states, while the dash curve near the E_C represents the Gaussian-distributed donor-like V_O state^[2.5].

2.1.2. Chemical disorder

Chemical disorder (i.e., point defects) form various localized state in the bandgap (**Figure 2.1a**)^[1.49,2.1]. In general, V_O has been considered as intrinsic chemical disorder in oxide materials and several research group have reported that V_O dominantly form various subgap states in AOSs such as shallow electron donor, deep donor, or electron trap state as explained in **Section 1.2**^[1.3,1.22]. Recently, some researchers suggest that vacancies are vague concept in amorphous materials and a vacancy is actually not well defined in amorphous structures^[1.25,1.26,2.6-2.8]. Unlike crystalline oxides, V_O and interstitial metal (M_i) are fundamentally indistinguishable in amorphous oxides. Similarly, metal vacancy (V_M) and interstitial O could be same in amorphous oxides^[2.5]. Thus, the terminology used for defects in crystalline solids may not be appropriate for use in amorphous oxides, leaving the real nature of defects in amorphous solids unclear^[2.5]. Instead of vacancy concept, they alternatively proposed that undercoordinated atom is the origin of subgap states in AOSs^[1.25,1.26,2.6-2.8]. Coordination number of metal (M) and O in amorphous oxides is averagely lower than that in the corresponding crystalline oxides^[1.24]. For example, In, Ga, Zn, and O in crystalline InGaZnO₄ has 6, 5, 5, and 4 coordination number, respectively^[2.8]. In amorphous InGaZnO₄, In, Ga, Zn, and O have smaller coordination number^[2.8]. **Figure 2.2a** depicts the DOS of AOSs. Individual local O deficiencies (D_O) (i.e., undercoordinated M) form subgap states in the upper half on the bandgap^[1.26]. D_O can also be described as tiny metal clusters. For example, Undercoordinated In can act as an intrinsic electron-trap center in In-based amorphous oxide semiconductors^[2.4]. **Figure 2.2b** shows that mean value of the In coordination number has been yielded to be ~ 5.5 ^[2.4]. Moreover, some undercoordinated In show maximum integrated charges in the Wigner-Seitz volume

(**Figure 2.2c**)^[2.4]. The local deficiency of O atoms around the In atom can accommodate the free electrons most likely via electrostatic attraction (i.e., Coulomb attraction). Thus, undercoordinated In captures free electrons. Undercoordinated In form In*-M bond as it trap two electrons and become stable as (In*-M)²⁻ center (**Figure 2.2d**)^[2.4]. Hard X-ray photoelectron spectroscopy (HXPES) results support that O deficient films have subgap states near CBM (**Figure 2.3a**)^[2.7]. On the other hand, subgap states up to 1.5 eV above the VB edge are originated from undercoordinated O (O_{uc}), not V_O^[1.26]. Concentration of O_{uc} could be reduced H doping which form O-H bond as shown in **Figure 2.3b**^[2.7]. Experimental results (**Figure 2.3c**) that subgap density of a-IGZO at the vicinity of VBM is reduced by H₂O annealing support that O_{uc} is the dominant atomic origin of deep level above VBM; O-H bonds are formed, results in fully coordination of O^[2.9].

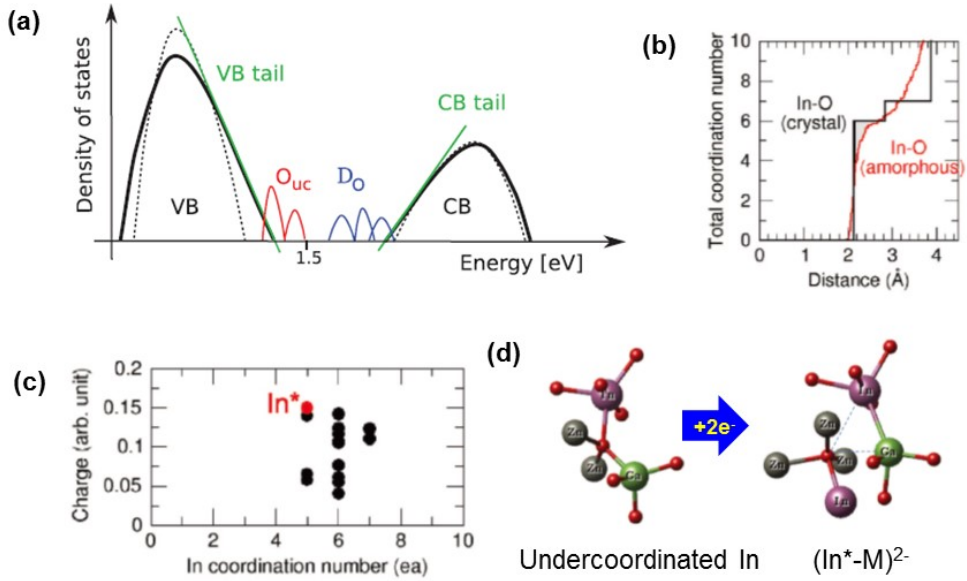


Figure 2.2 (a) Schematic sketch of the total DOS of AOSs. D_O and O_{uc} denote Individual local O deficiencies and undercoordinated O, respectively^[1,26]. (b) Running coordination numbers of In with O in crystalline and amorphous InGaZnO₄^[2,4]. (c) Integrated conduction electron charge inside the Wigner-Seitz volume around the In atoms as a function of the In coordination number. The best In atom that trap free electrons is denoted as In*^[2,4]. (d) Transition of atomic structure forming (In*-M)²⁻ center^[2,4].

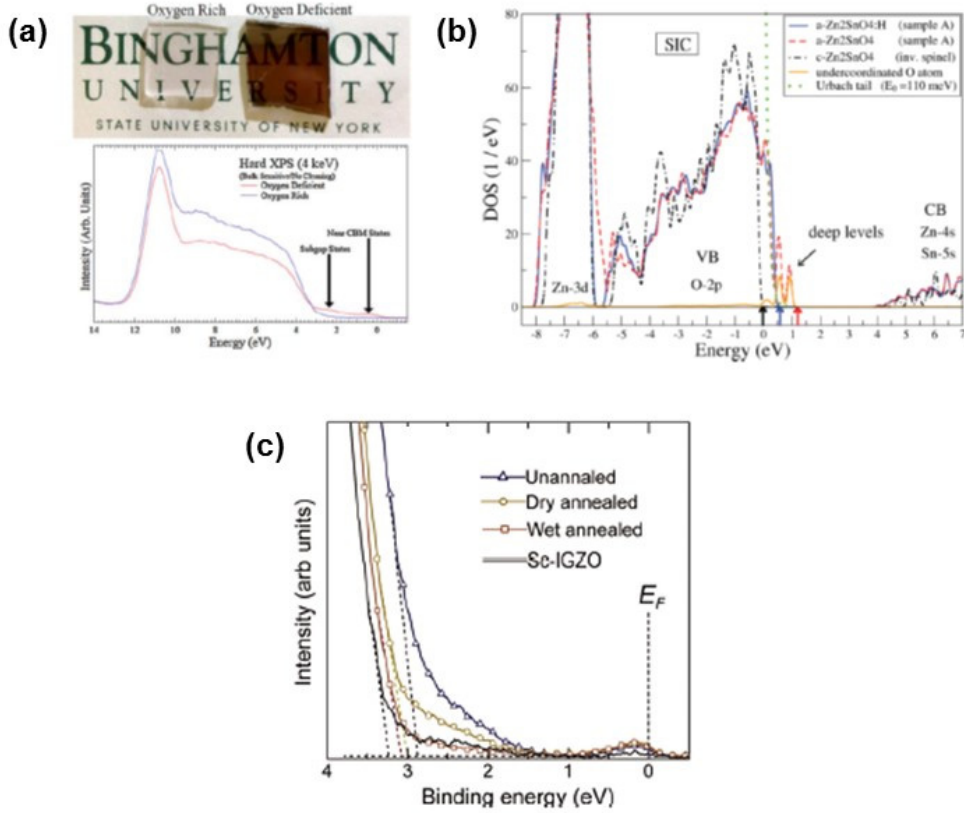


Figure 2.3 (a) Subgap states above valence band (VB) maximum due to undercoordinated O^[2.7]. These localized deep levels are annihilated. after H is doped. It would be induced by hydrogenation. Thus, O-H bonds are additionally formed, results in fully coordination of O. (b) a-IGZO films deposited on O rich and deficient conditions (top) and HXPES spectra of the corresponding films^[2.7]. (c) HXPES results in a-IGZO thin films according to post-deposition annealing conditions. Wet annealing was conducted at 400 C for 1 h under H₂O partial pressure of 0.2 atm^[2.8].

In addition to V_O and undercoordinated atom, weakly-bonded O (O_{wb}) is newly suggested that the crucial point defects which composed of subgap states as introduced in **Section 1.2.2**^[1.33,1.51,2.10-2.12]. After annealing at 300 °C under ozone (O_3) ambient, subthreshold slope (SS) value of a-IGZO TFTs increases compared to the un-annealed TFTs as well as annealed TFTs under below temperature of 250 °C as shown in **Figure 2.4a**^[2.10]. The authors suggest that SS value increases because deep continuous trap states are formed below CBM after O_3 annealing. **Figure 2.4b** shows the thermal desorption spectra (TDS) of O_2 in a-IGZO thin-films after post-deposition annealing^[2.10]. Regardless of annealing at 250 °C under O_3 ambient or 300 °C under O_2 ambient, TDS results are similar to the un-annealed a-IGZO thin-films. However, after O_3 annealing at 300 °C, significant amounts of O_2 -related species are desorbed even at low temperature from 100 to 300 °C. These results imply that O_3 annealing at 300 °C drastically increases O_{wb} density in a-IGZO and form deep continuous level. Moreover, O_{wb} can be removed by post-deposition thermal annealing process at below 200 °C under vacuum ambient^[2.10]. Interestingly, after application of high gate voltage, SS decreases whereas turn-on voltage increases (**right in Figure 2.4a**)^[2.10]. These results implies that deep traps induced by O_{wb} have the bistable states: the deep trap energy level become lower. The authors suggest that neutral state O_{wb}^0 form deep continuous trap level. When a large positive gate voltage is applied, O_{wb}^0 occupied free electron and become O_{wb}^{-1} (**Figure 2.4c**)^[2.10]. Energy level of O_{wb}^{-1} is below Fermi energy level (E_F), results in decrease of SS values. However, free electron concentration decreases during transition of valence state of O_{wb} from 0 to -1. As a result, TFTs become turn-on at larger gate voltage. When monochromated photons are subsequently examined, turn-on voltage decreases with increasing SS values as photon energy increases as shown in **Figure 2.4d**^[2.10]. Photon energy induces that O_{wb}^{-1} ejects electron and become O_{wb}^0 . O_{wb} can

form not only O_3 post-deposition annealing but also high O pressure during oxide deposition.

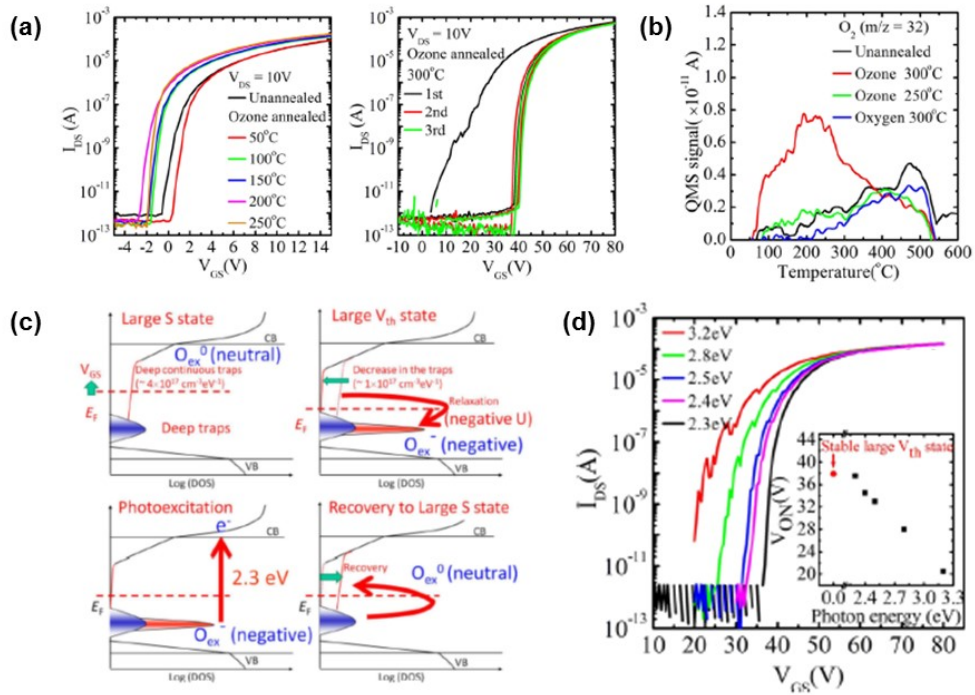


Figure 2.4 (a) Transfer characteristics of a-IGZO TFTs with respect to annealing at 50–300 °C for 15 min. under O_3 ambient. (b) TDS spectra of O_2 for a-IGZO thin-films subjected to different post-deposition annealing processes. (c) Dynamic changes in electronic states of O_{wb} according to gate voltage and photon energy. (d) Effect of monochromated photon energy on transfer characteristics changes in a-IGZO TFTs that underwent high gate voltage. All figures are bring from ref. 2.10.

Bistable O_{wb} could deteriorate stability of AOSs TFTs^[2.10]. Therefore, minimization or reduction of O_{wb} density in AOSs is crucially important. To decrease O_{wb} concentration, additional doping of alkali-earth ions such as Ca is suggested in addition to post-deposition annealing at $> 200\text{ }^{\circ}\text{C}$ ^[2.11]. Ca capping layer increases mobility of a-IGZO TFTs from ~ 10 to ~ 100 ^[2.11]. Plausible mechanism is that O_{wb} s in non-perfect Zn-O, In-O, and Ga-O bonds reacts with Ca dopants and form strong Ca-O bonds as depicted in **Figure 2.5a**^[2.11]. In addition to alkali-earth ions, Si dopant which has high oxide bond-dissociation energy is suggested to reduce O_{wb} density^[2.12]. When Si doping concentration is 3 at%, electrical conductivity of Si-doped In-O increases after storing in vacuum for 3 months, results in negative voltage shift of transfer characteristics of the ISO3 TFTs (**Figure 2.5b**)^[2.12]. When the TFTs are exposed to air for 2 weeks, transfer characteristics are nearly recovered to the as-fabricated states. The instability would be induced by desorption or adsorption of O_{wb} (**Figure 2.5c**)^[2.12]. However, 10 at%Si-doped-In-O TFTs (ISO10) show stable transfer characteristics regardless of changes in ambient atmosphere (**Figure 2.5b**)^[2.12]. Because Si dopants tightly hold O, results in decrease of O_{wb} concentration and suppression of desorption/adsorption of O_{wb} with respect to ambient atmosphere^[2.12]. As a result, long-term environmental stability of Si-doped In-O TFTs increases as Si doping concentration increases.

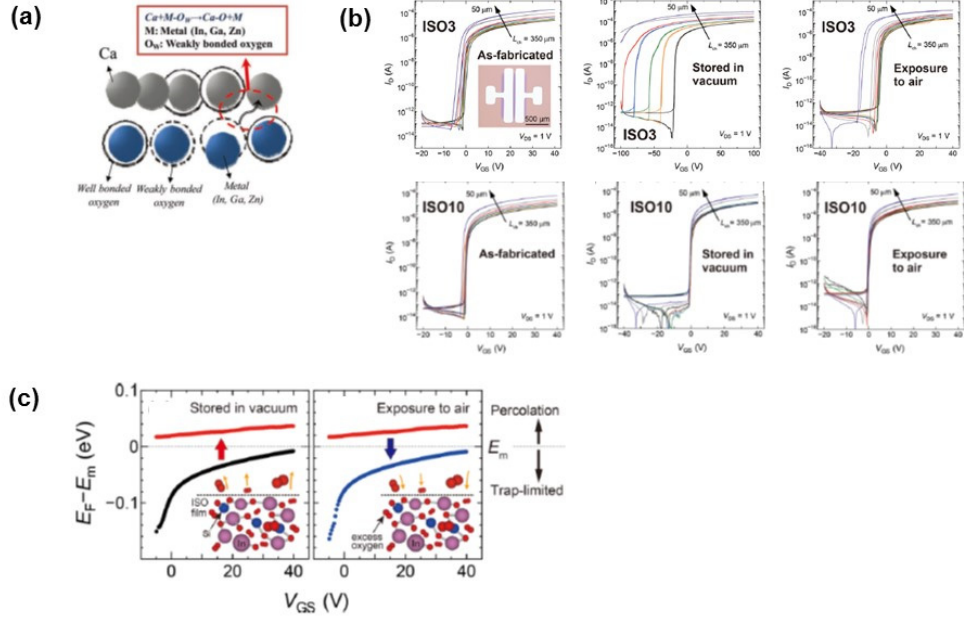


Figure 2.5 (a) Ca dopant form Ca-O bonds with O_{wb} , results in decrease of O_{wb} density^[2.11]. (b) Transfer curves of thin-film transistors (TFTs) composed of Si-doped In-O. Doping concentration of Si is varied from 3 (ISO3) to 10 at% (ISO10). The TFTs stored in vacuum (~ 10 Pa) for 3 months. Subsequently, the TFTs were exposed to air for 2 weeks^[2.12]. (c) The changes in Fermi energy (E_F) of Si-doped In-O TFTs with respect to gate bias voltage (V_{GS}) as well as ambient atmosphere (vacuum or air). After storing it in vacuum, E_F shifts above the mobility edge (E_m) due to desorption of O_{wb} . After exposing to air, E_F was changed back to the line plotted in blue because O_{wb} sneak in the oxides^[2.12].

Chapter 2: Theoretical Background

Lastly, important candidate chemical disorder to composed of subgap states is H as noted in Section 1.2.2. Although, H act as an electron donor and the concentration of H is over 10^{20} cm^{-3} (Figures 1.11a-1.11c), doping efficiency of H is very low. In Section 5.6, negligible influence of H on electrical properties of a-IGZO will be shown. O_{wb} may compensate H donor by following the reaction^[1,45,1.51]



In similar concept with O_{wb} , interstitial O (O_i) is suggested as compensation defect to H donor^[2,13]. Neutral O_i^0 forms dumbbell shaped O-O unit (Figure 2.6a). O dimer gives a defect state in the bandgap above the VBM (Figure 2.6b). When two H atoms are located at the vicinity of O_i^0 , Free electrons from H atoms are taken up by the O_i^0 , which becomes an O_i^{2-} . Deep level near VBM due to O dimer are eliminated as O_i combined with H (Figure 2.6c).

In summary, candidate chemical defects composed of subgap states are VO, M_{uc} , D_O , O_{wb} , H, and O_i (Figure 2.7). Understanding the nature of subgap states in AOS on the atomic scale is an essential prerequisite to not only improve electrical and optical properties of AOSs, but also secure long-term stability in AOS devices.

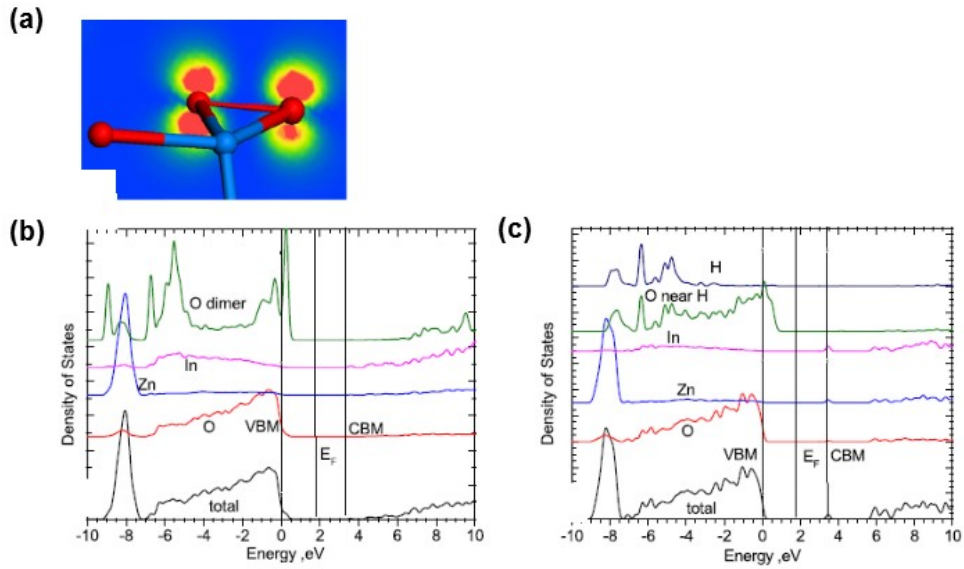


Figure 2.6 (a) Contour plot of wavefunction and (b) total and partial DOS in a-IGZO with one neutral interstitial O_i^0 . (c) The changes of DOS in Figure 2.6b when 2 H atoms are added in close to O_i^0 . All figures are bring from ref. 2.13.

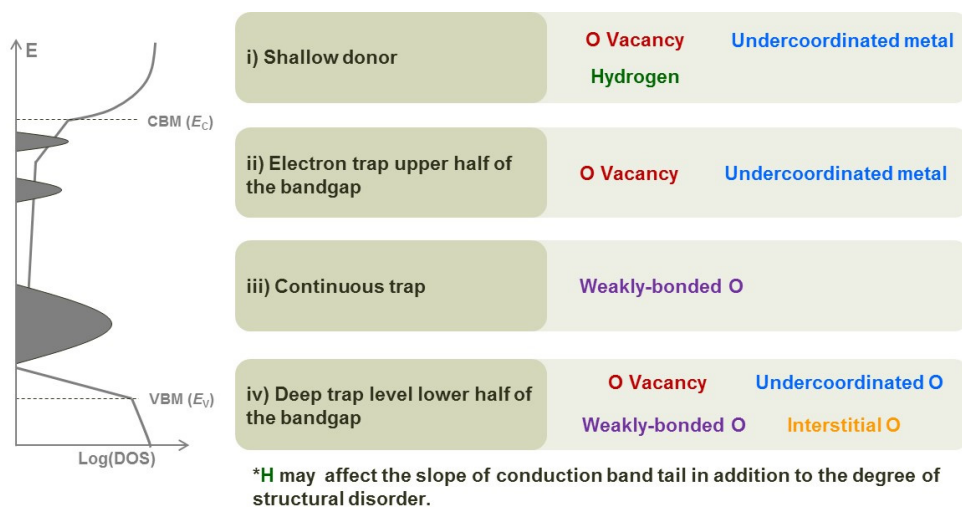


Figure 2.7 Summary of candidate chemical disorder (i.e., defects) composed of subgap states in AOSs.

2.2. Structural relaxation in amorphous solid

As was addressed in **Section 1.1**, amorphous materials are thermodynamically metastable to the corresponding crystalline-phase materials (**Figure 1.6**). As a result, structural relaxation (SR) occurs at below T_g ; internal atomic rearrangement without significant long-range atomic migration^[1.37-1.40]. Apparently, free volume, which is defined as excess specific volume of amorphous phase compared to crystalline phase^[2.14], decreases during SR as shown in **Figure 1.10**. In general, the kinetics of SR are described by viscosity (η)^[1.38,1.40,2.14]. η is a quantitative measure of the resistance flow in amorphous phase or is an inverse of atomic mobility^[1.40]. At below T_g , η follows Arrhenius relationship (**Figure 2.8a**) as^[1.38]

$$\eta \propto \exp\left(\frac{E_a}{k_B T}\right), \quad (2.2)$$

where k_B is Boltzmann's constant, T the absolute temperature, E_a is the activation energy of viscosity. Thus, the rate of atomic rearrangement increases as annealing temperature increases.

Interestingly, η values are also dependent on isothermal annealing time (**Figure 2.8b**). the rate of η is given as^[1.38]

$$\frac{d\eta}{dt} \propto \exp\left(\frac{E_a^*}{k_B T}\right), \quad (2.3)$$

Chapter 2: Theoretical Background

where E_a^* is the activation energy of the rate of η . It implies that η values increases as annealing time is elapsed, results in decrease of SR rate. **Figure 2.8c** presents the densification profile of amorphous silica films at 775 °C^[2.15]. At the early stage of annealing time, most of the densification is completed and densification rate drastically decreases. Similarly, the rate of SR would be weakly dependent on annealing time. Details of SR kinetics will be consulted in **Section 5**.

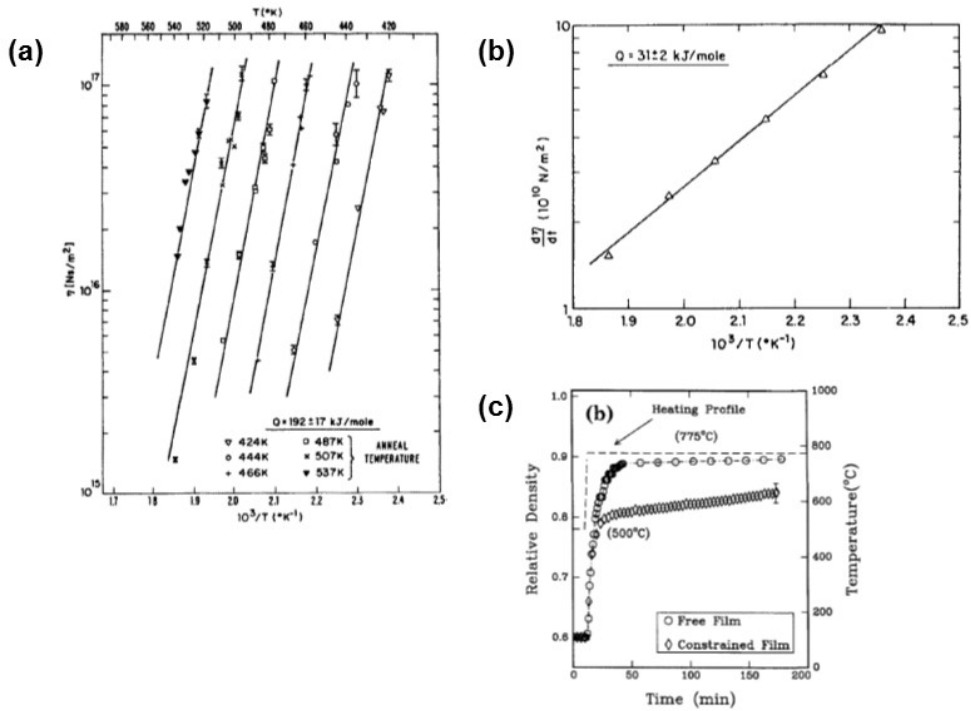


Figure 2.8 (a) Isoconfigurational viscosities of amorphous Pd-Si^[1.38]. (b) The temperature dependence of the rate of viscosity changes^[1.38]. (c) Densification of amorphous silica powder at 775 °C^[2.15].

2.3. Electrical conduction mechanism in metal/semiconductor/metal structures

In this thesis, vertical metal/AOSs/metal structured devices were utilized to identify the thermally driven *intrinsic* and *extrinsic* doping mechanisms. Doping concentration and dominant electronic states of dopants in AOSs were investigated through analyzing the changes in electrical properties of metal/AOSs/metal devices with respect to annealing conditions. **Figure 2.9** summarizes the basic electrical conduction mechanisms in metal/semiconductor/metal devices considering refs. 2.16-2.24: Schottky emission, Poole-Frenkel (P-F) conduction, space-charge-limited conduction (SCLC), and tunneling-based conduction. Details of the conduction mechanisms are introduced as shown in below.

2.3.1. Schottky emission

This conduction mechanism is based on the Schottky barrier at metal/semiconductor (MS) contact^[2.16-2.18]. Schottky barrier is formed when work function of metal (Φ_M) is higher than electron affinity (χ_s) of *n*-type semiconductors, and vice versa for *p*-type semiconductors. Space-charge region at MS contact induces electric fields and eventually disturbance of electron conduction occurs. In ideal condition, only the thermionic electrons could contribute to electrical current through MS contact. According to bias polarity, electrical conductance of the MS contact is drastically changed (i.e., rectifying contact). Interestingly, doping concentration (N_D) of semiconductors are crucial factor for determine the characteristics of Schottky emission^[2.17]. As N_D increases, probability about occurrence of electron tunneling

Chapter 2: Theoretical Background

increases. When N_D is below 10^{17} cm^{-3} , thermionic emission is dominant mechanism in Schottky contacts. In the range of $10^{17} \leq N_D \leq 10^{19}$, thermionic emission and tunneling coexist (i.e., thermionic-field emission). Remarkable fact is that rectifying performance is poorer compared to the thermionic emission^[2,18]. When N_D exceeds 10^{19} cm^{-3} , tunneling become dominant conduction mechanism in MS contact. In this conditions, MS contact acts as and Ohmic contact (i.e., quasi-Ohmic contact)^[2,17]. In this thesis, thermionic emission theory was one of the most important theory for extraction of doping concentration in AOSs in the devices. Details of Schottky-thermionic emission theory will be consulted in **Section 4.6**.

Chapter 2: Theoretical Background

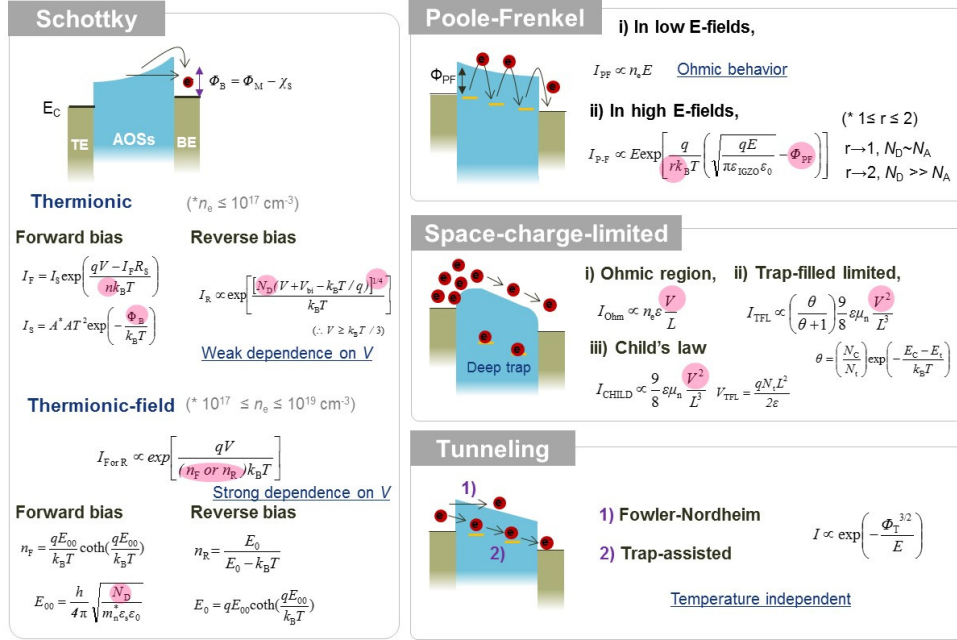


Figure 2.9 Basic electrical conduction in metal/semiconductor/metal structures modified from refs. 2.16-2.24.

2.3.2. Poole-Frenkel Conduction

P-F conduction means that electrical conduction occurs by field-enhanced thermal excitation of trapped electrons in the CBM^[2.16,2.19,2.20]. Notable characteristics is that Ohmic conduction occurs under the low magnitude of E ^[2.20] (**Figure 2.10**). When P-F conduction is dominant conduction mechanism of metal/AOSs/metal devices, free electron concentration (n_e) and donor (or trap) energy level could be extracted through analyzing the temperature dependence of P-F conduction^[2.19,2.20]. Consequently, N_D values are also derived based on the results of n_e and donor energy level. Details of P-F conduction theory and application of the theory for investigation of intrinsic N_D will be consulted in **Section 5.4.2**.

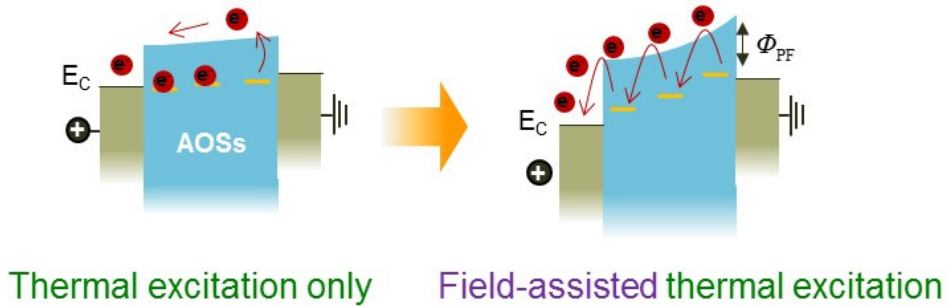


Figure 2.10 Transition of dominant conduction mechanisms from Ohmic to P-F with respect to the magnitude of electric field.

2.3.3. Space-charge-limited conduction

When semiconductors (or insulators) have significant shallow trap states, the current-voltage (I - V) characteristics of metal/semiconductor/metal vertically structured devices may follow the SCLC mechanism which consist of Ohm's law, trap-filled limited Child's law, and Child's law based on the magnitude of the applied voltage^[2,21-2,23]. At low voltages, when the number of thermally generated free carriers in semiconductors is larger than that of the injected charge carriers, the conduction follows Ohm's law ($I \propto V$). With increasing voltage, the current becomes dominated by the injected carriers, and the conduction follows the trap-filled limited Child's law [$I \propto (\Theta/1 + \Theta)V^2$], in which Θ is the ratio of the free carrier density to trapped electrons. When the traps are filled with injected carriers ($\Theta \gg 1$), the conductance sharply increases, and the conduction follows Child's law ($I \propto V^2$). In summary, the value of the slope of the double-logarithmic I - V curves [i.e., $d\log(I)/d\log(V)$] changes as the value of Θ changes from 1 (Ohmic) to >2 (Trap-filled limited Child's law) to 2 (Child's law) with increasing voltage.

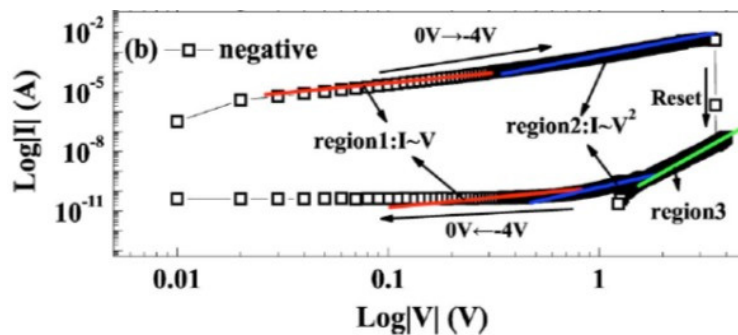


Figure 2.11 SCLC in Cr/ZrO₂/heavy doped-Si structure^[2,23].

2.3.4. Tunneling-based conduction

Tunneling is dependent on the magnitude of applied E as well as trap distribution^[2.16,2.24]. N_D also crucial factor for determine occurrence of tunneling as noted in **Section 2.3.1**. When E is applied on the semiconductors, triangular potential barrier is formed in semiconductors^[2.16]. Electron could wave function penetrate through the triangular potential barrier into the CBM of semiconductors, which refers to Fowler-Nordheim (F-N) tunneling. Although the magnitude of applied E is lower enough not to occur F-N tunneling, tunneling could occur through trap level in the band gap (i.e., trap-assisted-tunneling)^[2.24]. Remarkable characteristics of tunneling are that the tunnel emission has the strongest dependence on the applied electric field, but shows weakest dependent on the temperature.

2.4. Introduction to resistive switching devices

Non-volatile resistive switching (RS) devices or memristor (short for memory resistor) means that two-terminal device follows a state-dependent Ohm's law^[2.25]: Electrical resistance of memristor is reversibly changed by external stresses (e.g., voltage or current). **Figure 2.12a** shows the circuit symbol of RS devices as 4th passive circuit elements, in addition to resistor, capacitors, and inductors^[2.26]. Insulating or semiconducting materials are inserted between two electrodes (**Figure 2.12b**). So far, candidate active materials for RS are various, including polymer, amorphous Si, nitrides, chalcogenides, and metal oxides^[2.27].

Due to their simple structure compared to transistor-based memory, implementation of crossbar circuits, which have an unit cell in each intersection of interconnects (e.g., word line, bit line), using RS devices are expected (**Figure 2.12c**). Then the smallest possible cell size will be $4F^2$ (F of minimum feature size), where the distance between the electrodes is equal to the device size. $4F^2$ is the highest density attainable in 2-dimensional (D) planar circuits. Moreover, 3-D array (i.e., multi-stacking structure) also could be demonstrated (**Figure 2.13a**)^[2.28]. The main target application of RS devices are high-density and non-volatile memory^[2.25,2.28]. Moreover, RS devices could be utilized in logic architecture as well as neuromorphic circuits due to their outstanding performance in terms of cell density, energy per bit, read time, write time, retention, and endurance (**Figure 2.13b**)^[2.29].

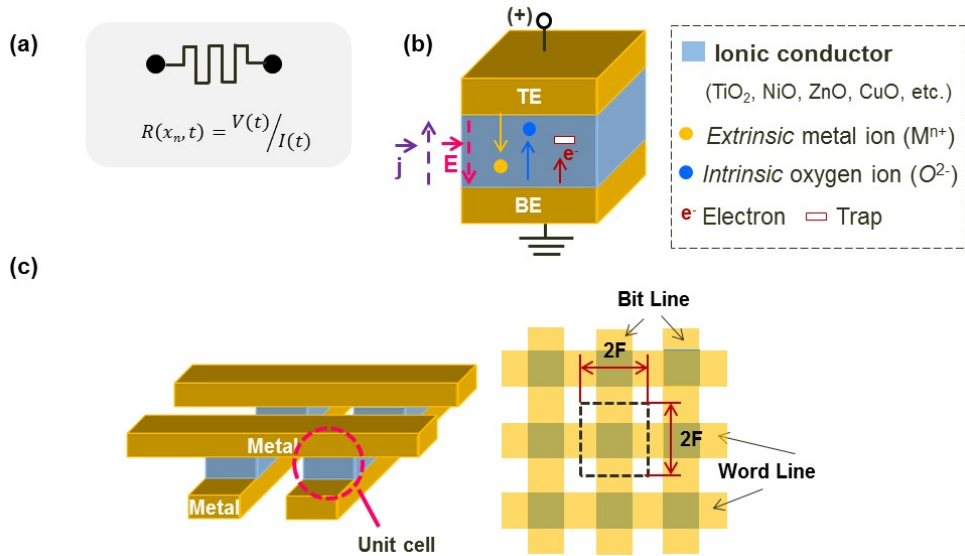


Figure 2.12 (a) Circuit symbol of memristor or RS devices^[2,25]. (b) metal/metal oxides/metal structure for RS devices. In addition to metal oxides, various insulating (or semiconducting) materials show RS behavior. (c) Schematics of crossbar circuits composed of RS devices per one cell.

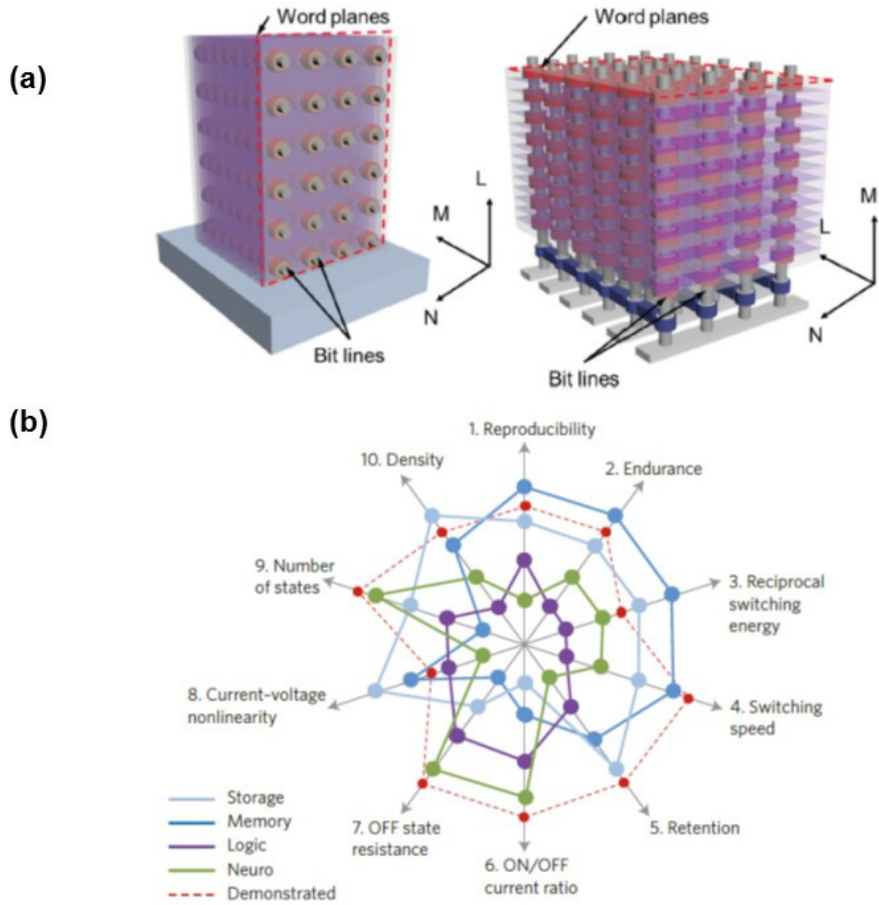


Figure 2.13 (a) Schematics of 3-dimensional crossbar array using RS devices in terms of vertical stacking (left) and horizontal stacking (right) of word lines^[2.28]. **(b)** Demonstrated performance and required performance for representative applications of RS devices^[2.29].

RS devices are classified in terms of operating polarity of voltage as unipolar (also called nonpolar when devices can be operated with both polarity of bias) and bipolar switching (**Figure 2.14a**)^[2.27]. Transition from high resistance state (HRS) to low resistance state (LRS) is called SET, and RESET is vice versa. Unipolar RS means that SET and RESET occur at the same bias polarity with different magnitude of bias, whereas bipolar RS indicates that RESET occurs only when the opposite polarity bias to SET condition is applied. In general, SET process in the first cycle shows different electrical characteristics from that of the other SET process and is called forming process (**Figure 2.14b**)^[2.30].

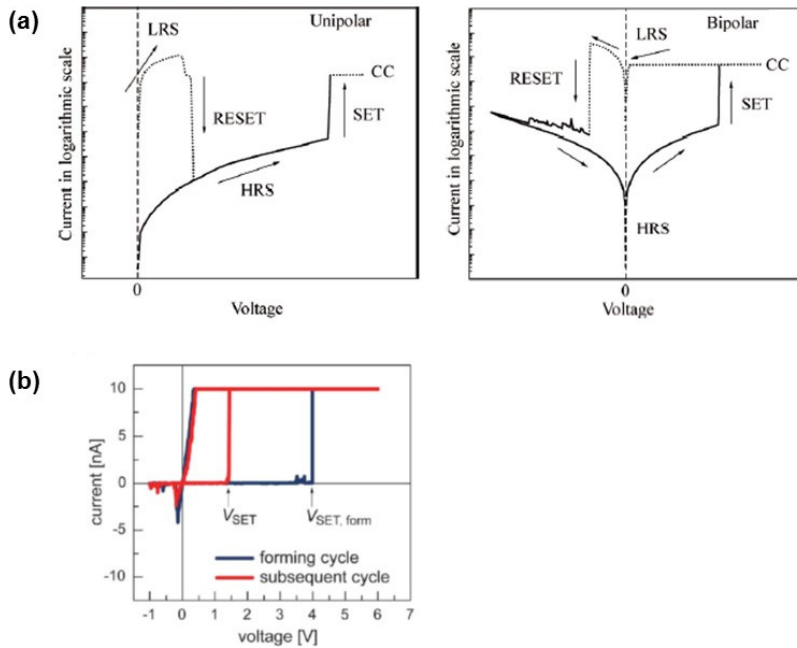


Figure 2.13 (a) RS mode: unipolar and bipolar^[2.27]. (b) Current-voltage characteristics of a Cu/SiO₂/Pt structured devices^[2.30].

So far, various RS mechanisms have been suggested^[2.25-2.29]. However, the details of the underlying mechanisms of RS are still debated and are an active research area^[2.25-2.29]. We believe that RS phenomena could not be explained by one solid theory, because various factors such as type of active materials and interfacial properties of metal/active materials affect RS.

A concomitant feature in diverse RS mechanisms is that they consider that conductive filaments (CFs) or space charge region (SCR) in active materials is core origin of RS. In further details, CFs means that localized conducting region in active materials. Main components of CFs in metal oxides can be classified as *extrinsic* metal ion from electrodes or *intrinsic* V_o (**Figure 2.12**). According to CF formation/rupture, resistance of the devices is altered (**Figure 2.14a**)^[2.31]. SCR could be located at the metal/active materials contacts (i.e., Schottky barrier)^[2.32] and/or at the bulk of active materials^[2.33,2.34]. Distribution and excess charge density in SCR are modulated by dopant migration or charge trap/de-trapping. Thus, modulation of Schottky barrier height/width^[2.32], homogeneous changes in electrical conductivity of active materials^[2.33], or charge trapping/detrapping at SCR in the bulk region^[2.34] could be plausible RS mechanisms based on SCR.

In this thesis, Cu dopant-based CFs and charge trapping/detrapping at SCR in the bulk of AOSs is main factors for RS in AOSs (**Section 6**). Therefore, we focus on the CF-based RS and charge trapping/detrapping at SCR in the bulk and introduce details of their proposed mechanisms as shown below.

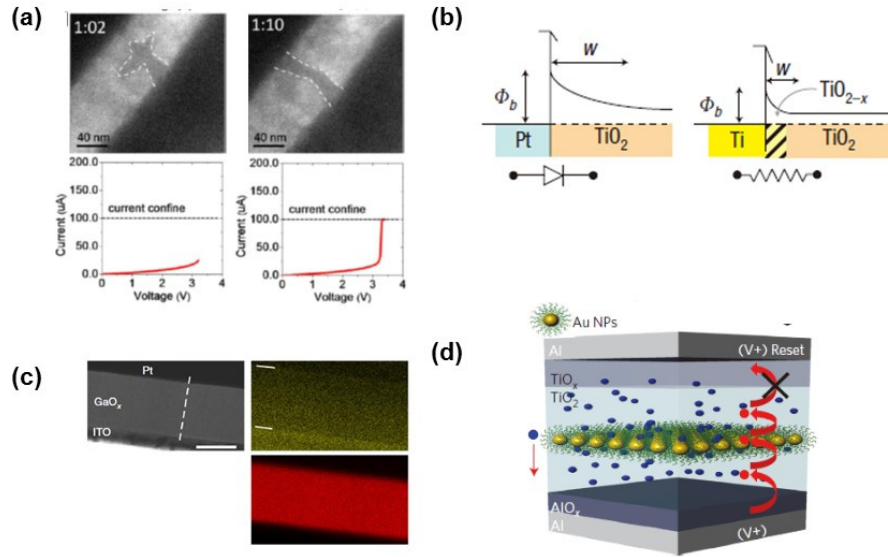


Figure 2.14 (a) *In-situ* transmission electron microscopy (TEM) images and the corresponding current-voltage characteristics of Pt/ZnO/Pt devices^[2.31]. (b) Energy band diagram presents the modulation of Schottky barrier height due to formation of O-deficient interfacial layer at Pt/TiO₂ interface^[2.32]. (c) Gradual decrease of O concentration (yellow) in GaO_x after RS^[2.33]. Concentration gradient of Ga (red) is not observed. (d) Schematic of electron trapping due to Au nanoparticles in TiO₂^[2.34].

Figures 2.15 and **2.16** summarize the Forming (or SET) mechanism and RESET mechanism in CF-based RS, respectively. Refs. 1.72, 2.29, 2.31, 2.35-2.44 were considered to draw **Figures 2.15** and **2.16**.

Firstly, mobile ions are generated by the electric field or electrochemical potential gradient as shown in **top in Figure 2.15**^[2.31,2.35]. Bondings in oxides are broken due to thermochemical driving force^[2.37] and electrochemical dissolution (or oxidation) also occurs at active electrodes^[2.36]. At initial states, mobile ions could be formed due to non-stoichiometry of oxides as well as diffusion of *extrinsic* defects from electrodes^[2.33,2.38].

Secondly, mobile ions move to toward the counter electrodes by drift, diffusion, and electromigration (**middle in Figure 2.15**)^[2.29]. In general, ion drift dominantly occurs by the electric field. When ions move to the counter electrodes, reduction concurrently occurs^[2.39]. Thus, CFs are formed by reduction of ions with alignment of ions (i.e., percolation path)^[2.40,2.41] or local phase transformation^[2.42] (**bottom in Figure 2.15**), results in forming or SET. Driving forces of RESET process are composed of thermal stress and/or electrochemical potential gradient (**Figure 2.16**)^[2.29,2.35,2.43]. As electrical current dominantly flows local CFs at LRS, Joule-heating would occur^[2.43]. RESET mechanism of unipolar RS suggests that significant amount of Joule-heating induces CF rupture: It is called fuse-antifuse mechanism^[2.43]. In the RESET process of bipolar RS, electrochemical oxidation also occurs at CFs. Thus, rupture of CFs in bipolar RS is interplay of Joule-heating and electrochemical dissolution^[2.29,2.35,2.44]. In general, all of CFs is not eliminated under RESET. Instead, part of CFs partially rupture and subsequently connection of top electrodes and bottom electrode is disconnected. Partial recovery of CFs is solely needed for SET, again. Therefore, electrical characteristics of initial states are different from that of HRS (**Figure 2.13b**).

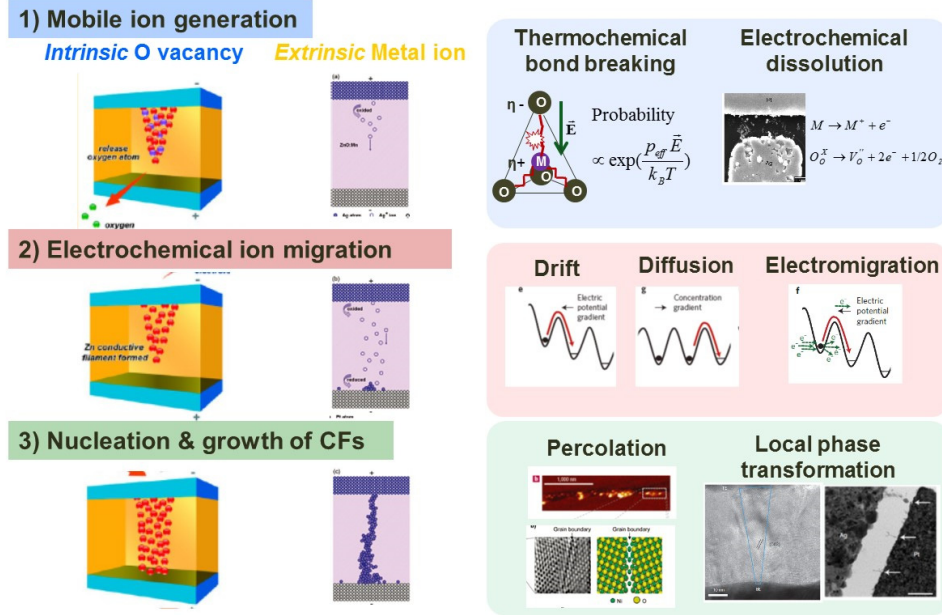
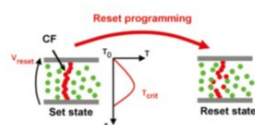


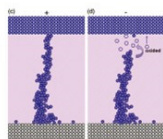
Figure 2.15 Resistive switching mechanism: conductive filaments formation (forming or SET). Refs. 1.72, 2.29, 2.31, 2.35-2.44 were considered.

4) CFs dissolution



Joule-heating
(Thermochemical)

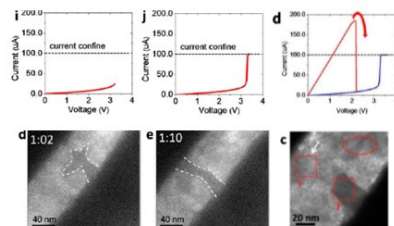
U. Russo et al., *ITED*, 56, 186 (2009)



Oxidation
(Electrochemical)

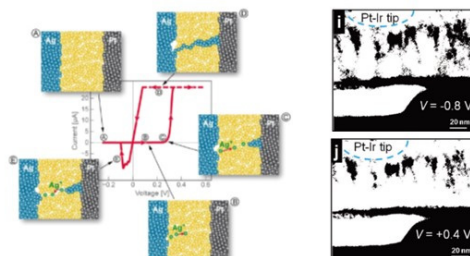
Y. C. Yang et al., *Nano Lett.*, 9 (2009)

❖ Joule-heating dominant → Unipolar switching



J.-Y. Chen et al., *Nano Lett.*, 13 (2013)

❖ Oxidation dominant → Bipolar switching



R. Waser et al., *Nanotechnology*, 22 (2011)
S. J. Choi et al., *Adv. Mater.*, 23 (2011)

Figure 2.16 Resistive switching mechanism: conductive filaments dissolution (RESET).

Refs. 1.72, 2.29, 2.31, 2.35-2.44 were considered.

Figure 2.17a presents typical unipolar RS based on charge trapping/detrapping at SCR in the bulk: Current-voltage (I - V) characteristics of crosslinkable poly(4-n-hexyltriphenyl)amine (xHTPA) with and without Au nanoparticles (NPs) inclusion^[2,45]. Top and bottom electrode materials are In-Sn-O (ITO) and Ca/Al, respectively. When Au NP is blended in xHTPA (**Figure 2.17b**), negative differential resistance (NDR) behavior is newly observed. Voltage-controlled NDR behavior have been explained that high field domains (i.e., increase of charge density in SCR) are formed during application of bias (**Figure 2.17c**)^[2,16,2,46]. In detail, charges are trapped on NPs, and a space-charge field builds up, results in reduction of electrical conductance of the devices. Characteristics of NDR-based RS is tuned by NPs concentration (i.e., changes in distribution of SCR in the bulk of active materials) as shown in **Figure 2.17d**^[2,47].

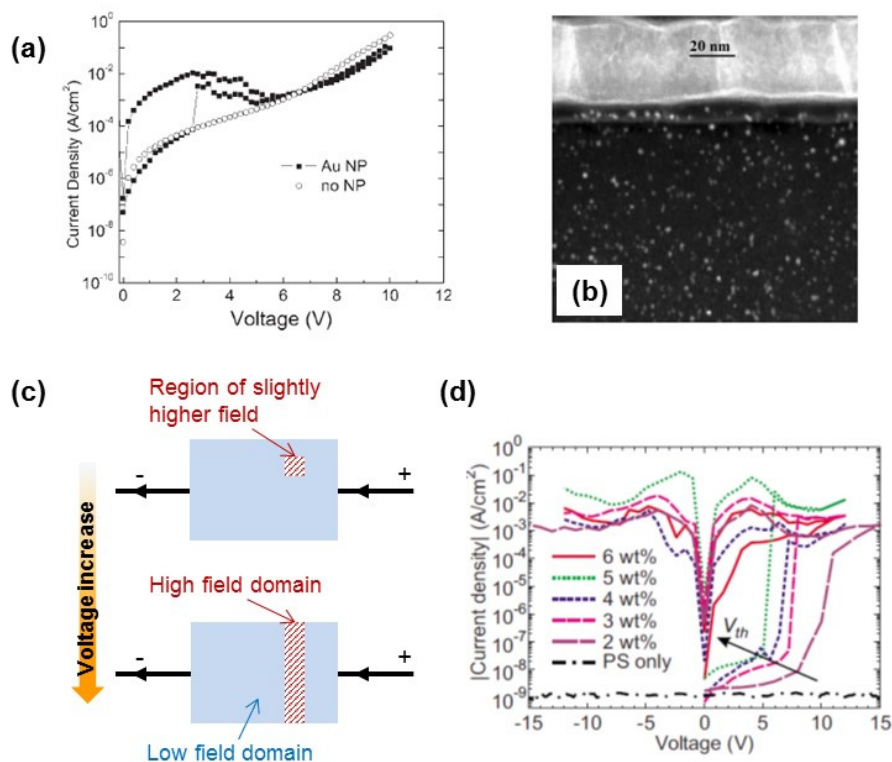


Figure 2.17 (a) I - V characteristics of ITO/xHTPA/Ca/Al devices with and without Au NPs^[2.45]. (b) Au NPs inclusion in xHTPA. Images are obtained by high-resolution dark-field TEM^[2.45]. (c) Formation of high-field domain in a voltage-controlled NDR. (d) RS characteristics of polystyrene (PS) with respect to weight percent of phenyl-C61 butyric acid methyl ester (PCBM) clusters^[2.47].

CHAPTER 3

Experimental Procedures

3.1. Sample Preparation

3.1.1 Device fabrication

The purpose of the devices is that thermally driven atomic rearrangement (or migration) induced the changes in electrical properties of AOSs are measured without unwanted interactions of AOSs with electrodes and ambient atmosphere. **Figure 3.1** show the schematics of the plane view of the devices according to the fabrication process steps. A 30-nm-thick Ta-Al bilayer was deposited on a SiO₂ (100 nm)/Si wafer using DC sputtering as the adhesive layer. For the bottom electrode (BE) of the devices, 160-nm-thick W was deposited on the Ta-Al adhesive layer. A 500-nm-thick SiO₂ isolation layer was deposited by plasma-enhanced chemical vapor deposition at a substrate temperature of 300 °C. Throughgoing holes were patterned in the isolation layer using photolithography and dry etching, and the area was varied from 25 to 400 μm^2 . This step was followed by radiofrequency (RF) sputtering of a-IGZO thin films, using a polycrystalline InGaZnO₄ target at room temperature (RT). Film thickness is varied

from 40-nm to 160-nm. Using photolithography followed by dilute HF etching, the a-IGZO thin-films were patterned into square-shaped patches; the area of each patch was $6,400\ \mu\text{m}^2$ to fill the SiO_2 hole. Finally, the top electrode (TE) consisted of a W (160-nm-thick)/Ta-Al (100-nm-thick) stack that was DC-sputtered in a blanket layer and patterned using the lift-off process to cover the a-IGZO patches. Plane optical images and cross-sectional images of the devices in the as-fabricated state using transmission electron microscopy (TEM) are shown in **Figures 3a and 3b**, respectively. W that directly contacts with a-IGZO hardly diffuse into a-IGZO and the Ta-Al bilayer blocks interaction between the a-IGZO and the ambient atmosphere. Details of material selection rule and the validity of the devices on the investigation of thermally driven doping mechanism are consulted in **Section 4**.

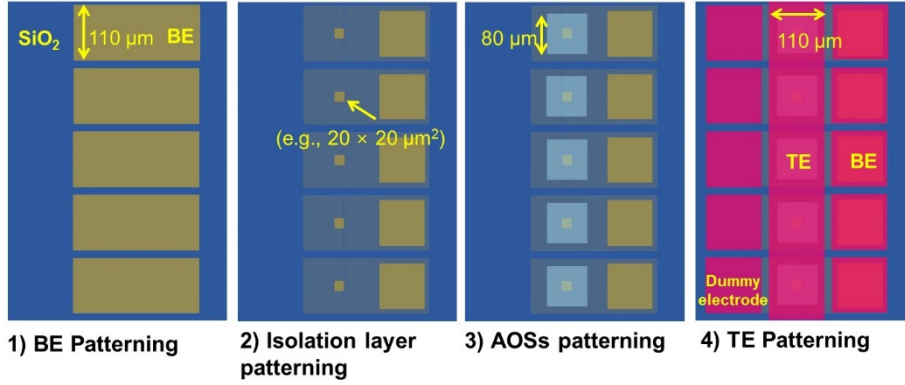


Figure 3.1 Schematics of the plane view of the devices at each process step.

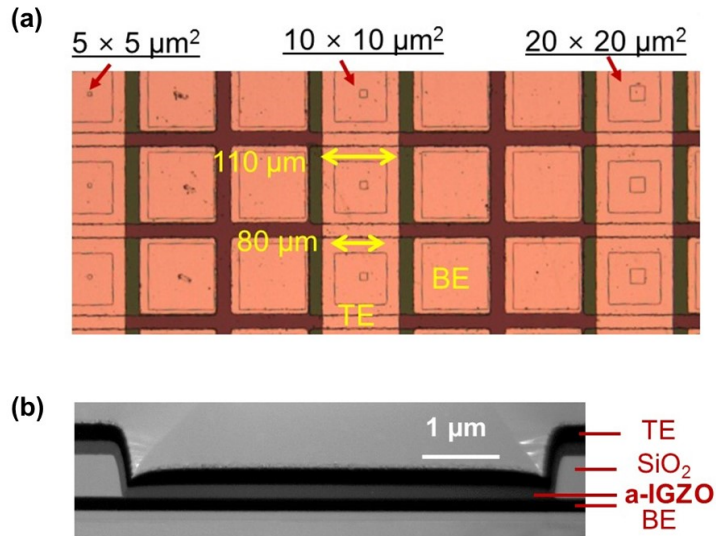


Figure 3.2 (a) Plain optical image and (b) cross-sectional TEM images of the devices in the as-fabricated state.

3.1.2. Multi-layer thin films

Size of a-IGZO thin-films patches in the devices is too small to conduct X-ray photoelectron spectroscopy (XPS) and secondary ion mass spectroscopy (SIMS), which analysis is used to measure composition profile as well as chemical states of materials. Therefore, when the devices are fabricated, multi-layer thin-films are simultaneously fabricated as shown in **Figure 3.3a**. Moreover, a-IGZO/W-Ta-Al/Si substrate, a-IGZO/Si substrate, and a-IGZO/glass substrate samples are fabricated to measure roughness, density, and optical properties of a-IGZO thin films (**Figures 3.3b-d**).

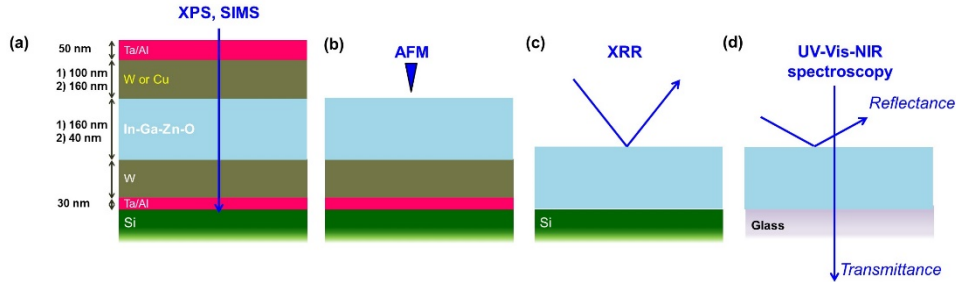


Figure 3.3 Schematic structure of multi-layer thin films to measure (a) composition profile with chemical states, (b) roughness, (c) density, and (d) optical properties of a-IGZO thin films.

3.1.3. Van der Pauw samples

The van der Pauw-Hall method is one of the most widely used to measure resistivity, carrier type, carrier concentration (n_e), and carrier mobility of thin-film materials^[3,1]. To measure initial electrical properties of a-IGZO, van der Pauw-Hall samples were fabricated as depict in **Figures 3.4a and 3.4b**. $1 \times 1 \text{ cm}^2$ -a-IGZO thin-films, which thickness is same with the a-IGZO thin-films in the devices, were deposited on 100-nm-thick-SiO₂/Si substrates. A 100-nm-thick Al contacts were deposited at each corner of a-IGZO thin-film patches. Patterns of both a-IGZO patches and Al contacts are formed using shadow mask during the deposition. We selected contact material as Al, because Al form Ohmic contact at the oxide interfaces, as it uptakes O from the oxides (i.e., V_O generation) and subsequently forms heavy-doped region at Al/oxide interfaces.^[2,17]

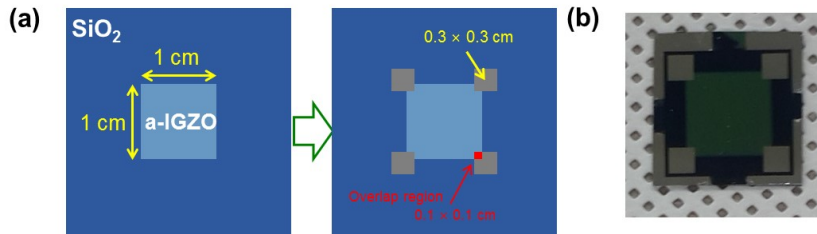


Figure 3.4 (a) Schematic of the plane view of the van der Pauw samples at each process step. **(b)** Plain optical image of van der Pauw sample.

3.2. Structural and Optical analysis

Roughness of as-deposited a-IGZO thin-films on the same substrate as the devices (**Figure 3.3b**) was measured using atomic force microscopy (Nanostation II, Surface Imaging Systems). Density of a-IGZO thin-films was measured using X-ray reflectivity (XRR, X'pert-Pro, Philips, Inc). For the XRR measurements, the substrates were changed to 525- μm -thick Si wafers (**Figure 3.3c**) because the use of a multi-layered substrate makes analyzing the spectrum data more difficult. Transmittance (T) and reflectance (R) of a-IGZO thin-films deposited on 1000- μm -thick quartz glass (**Figure 3.3d**) with respect to the photon energy ($h\nu$) measured using an Agilent Cary 5000 UV-Vis-NIR spectrophotometer.

3.3. Post-fabrication annealing

The devices (**Figure 3.2**) and multi-layer thin films (**Figure 3.3a**) were annealed at temperatures of 300- 500 °C for 1-100 h. For the annealing process, the temperature increased at a heating rate of 5 °C/min from RT to the target annealing temperature, followed by maintenance of the target temperature for the specified duration. Most of Annealing processes are examined under vacuum condition (10^{-3} Pa). To verify the devices could block interaction between a-IGZO thin films and ambient atmosphere (**Section 4**), conditions of ambient atmosphere were varied as

- vacuum (10^{-3} Pa),
- N₂ (working pressure of 10^{-1} Pa),
- N₂ (working pressure of 10^3 Pa),
- N₂/O₂ (95vol%/5vol%; working pressure of 10^3 Pa) and
- N₂/H₂ (95vol%/5vol%; working pressure of 10^3 Pa).

3.4. Electrical analysis

Figure 3.5a shows the probe station equipped with hot chuck and connected with an Agilent 4156 semiconductor parameter analyzer (**Figure 3.5b**). Current-voltage (I - V) characteristics of the devices were measured using this equipment. Voltage was applied to the TE, whereas the BE was grounded. The substrate temperature was varied from RT to 96 °C. Temperature coefficient of resistance (TCR) in the devices was measured using a Qualitau MIRA EM tester (**Figure 3.5c**).

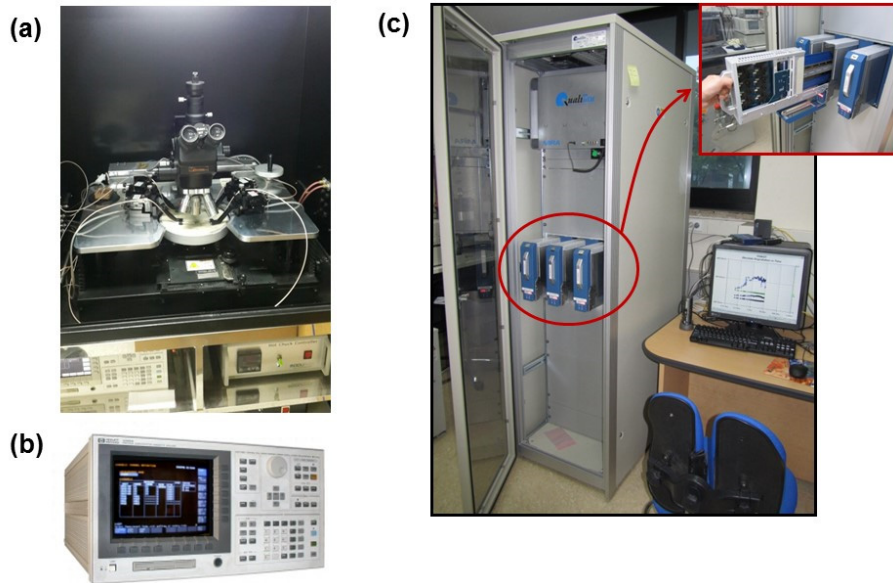


Figure 3.5 (a) Probe station used in this study. (b) Agilent 4156C semiconductor parameter analyzer. (c) Qualitau MIRA EM tester (C6020).

3.5. Microstructural and chemical analysis

The cross-sectional images of the devices as-fabricated and after annealing were taken using a JEOL JEM-2100F transmission electron microscope (TEM). The TEM samples were fabricated using a focused ion beam (FIB, SII NanoTechnology SMI3050SE). Scanning TEM-EDS (energy dispersive X-ray spectroscopy) composition profiles of the devices were also obtained.

An XPS (PHI-5000 Versa Probe, Phi Physical Electronics, Chanhassen, MN) was used to measure the changes in the compositions and chemical states of the elements in the multi-layer thin films (**Figure 3.3a**) that have the same dimension as the devices after annealing. In addition to XPS, time-of-flight secondary ion mass spectrometry (TOF-SIMS) (TOF-SIMS 5, ION-TOF GmbH, Münster, Germany) was utilized to measure the compositional changes in the multi-layer thin films.

3.6. Computation

The changes of density of states (DOS) in a-IGZO with respect to site location of Cu dopants based on the first-principles calculation using the VIENNA ab-initio simulation package (VASP) were calculated^[3,2,3,3]. A projector-augmented wave (PAW) pseudopotentials⁶³ and generalized gradient approximation (GGA)^[3,4] for exchange-correlation energy were used. The orbital dependent on-site energy (U) is employed for the metal (In,Ga,Zn, and Cu)-d electrons to correct the unphysical strong self-interaction of GGA^[3,4,3,5]. Amorphous structure of a-IGZO with stoichiometry of $n\text{In}:n\text{Ga}:n\text{Zn} = 1:1:1$ and 18 formula units of InGaZnO_4 using melt-quenching method via molecular dynamics (MD) simulations was modeled. Moreover, computational parameters were employed from ref. 3.6. The geometry of the final amorphous structure is fully optimized until the forces on each atom were converged to 0.05 eV/\AA at 0 K using 500 eV plane-wave cutoff energy and Γ -point only k-point sampling.

CHAPTER 4

Development of the Devices Able to Regulate Extrinsic Reactions of Amorphous Oxide Semiconductors

4.1. Introduction

The objective of this thesis is to identify the *intrinsic* and *extrinsic* doping mechanism in AOSs with respect to thermal history. For investigation of thermally driven doping mechanism in AOSs, regulation of additional reactions in AOSs such as redox reactions is prerequisite. In this study, structure of AOSs-based devices are designed to prevent *undesirable extrinsic* reactions and to measure the changes in electrical properties of AOSs solely induced by atomic rearrangement or migration. Electrode materials of the devices are rigorously selected based on Gibbs free energy of oxide formation and self-diffusivity.

4.2. Experiments

The devices and multilayer thin films, which is introduced in **Section 3**, were fabricated. The key process conditions of deposition of a-IGZO thin-film were as follows: 50-W RF power under working pressure of 5 mTorr, and the process gas flow rates of argon (Ar) and O₂ of 19 and 1 sccm (i.e., an O partial pressure of 3.3×10^{-2} Pa), respectively. Structural properties (i.e., roughness and density) and optical properties of as-deposited a-IGZO thin films were investigated using AFM, XRR, and UV-vis-NIR spectroscopy (**Section 3.2**). W was deposited on a-IGZO thin-film patches as TE material. To verify that Ta-Al layer can block interaction between a-IGZO and ambient, Ta-Al bilayer was not deposited on W TE of some of the devices. Annealing processes were conducted on the devices under 450 °C and annealing time was varied from 1 to 9 h. Annealing ambient conditions were also varied as vacuum (10^{-3} Pa), N₂ (working pressure of 10^{-1} Pa), N₂ (working pressure of 10^3 Pa), N₂/O₂ (95vol%/5vol%; working pressure of 10^3 Pa) and N₂/H₂ (95vol%/5vol%; working pressure of 10^3 Pa).

After annealing, microstructural analysis was conducted on the devices using TEM and XPS analysis was conducted on the annealed multi-layer thin films to observe the changes of composition profile changes and chemical states of the element.

I-V characteristics of the devices with Ta and the devices without Ta-Al after annealing were measured as voltage was applied to the TE, whereas the BE was grounded.

4.3. Characteristics of as-deposited oxide films

Investigation of structural properties, and optical properties of as-deposited a-IGZO thin-films is important because the SR phenomena would be dependent on the initial characteristics of the films^[1.35,1.45,1.50,4.1]. **Figure 4.1a** shows the roughness of as-deposited a-IGZO thin-films on the same substrate (W/Ta-Al/SiO₂/Si) as the devices using AFM. Both 40- and 160-nm-thick a-IGZO thin films have roughness values of less than 1 nm. The film density and the film roughness were measured using XRR as shown in **Figure 4.1b**. Although the a-IGZO film thickness increases from 40-nm to 160-nm, the film density is constant at a value of 5.8 g·cm⁻³ (the film roughness increases from 0.4 nm to 1.1 nm). The obtained film density is smaller than that of the single crystalline InGaZnO₄ (6.2 ~ 6.379 g·cm⁻³) and is similar to that of the pulsed-laser-deposited a-IGZO films (5.9 g·cm⁻³)^[4.2]. **Figure 4.2a** shows the transmittance (*T*) and reflectance (*R*) of 160-nm-thick a-IGZO films deposited on 1000-μm-thick quartz glass using UV-Vis-NIR spectroscopy. The shapes and the magnitudes of *R* and *T* are similar to those in previous reports, although the position of the peak valley is slightly different^[1.22,1.23]. The absorption spectra (*α*) presented in **Figure 4.2b** was obtained from the following equation^[1.22,1.23,4.1]:

$$\alpha = -\ln \left[\frac{T}{(I - R)d} \right] \quad (4.1)$$

Where *d* is the film thickness (160 nm). The optical bandgap (*E_g*) was extracted by applying the Tauc model $[(\alpha h\nu)^{1/2} \propto h\nu - E_g]$ ^[1.22,1.23,4.1], which yields a value of 3.14 eV, as shown in **Figure 4.3b**. Moreover, tail-like optical absorptions (as well as Lorentz-

Chapter 4: Development of the Devices Able to Regulate Extrinsic Reactions of Amorphous Oxide Semiconductors

type absorptions) are observed below the E_g . The exponential decay of α is related to the Urbach tail [$\alpha \propto \exp(h\nu / E_u)$]^[1,22,4,1], and the Urbach energy (E_u) yields a value of 0.20 eV. The obtained E_g and E_u are similar to those obtained in the previous report (E_g of 2.98 eV and E_u of 0.16 eV)^[1,22]. The values of E_g and E_u change with respect to the initial film quality and with post-annealing^[4,1]. In previous reports, the origin of tail-like absorption was determined to be the subgap state near the valence band maximum (VBM) composed of V_{OS} in the deep-donor states^[1,22,4,1], as confirmed by hard X-ray photoemission spectroscopy (HX-PES) analysis^[4,1]. Therefore, these results confirm that the as-deposited a-IGZO thin films in this study have V_{OS} in the deep donor states located near the VBM^[1,22,1,50,4,2].

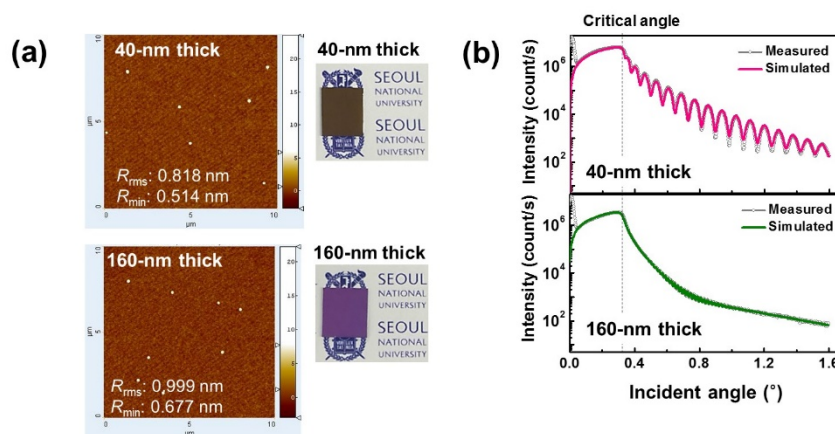


Figure 4.1 (a) AFM results of the as-deposited a-IGZO thin-films on the same substrate as the devices (top) and photographs of the 1-cm wide samples (bottom). (b) XRR spectra of IGZO thin-films deposited on Si wafers, which shows that the density of both the 40-nm and 160-nm-thick a-IGZO films is $5.8 \text{ g} \cdot \text{cm}^{-3}$.

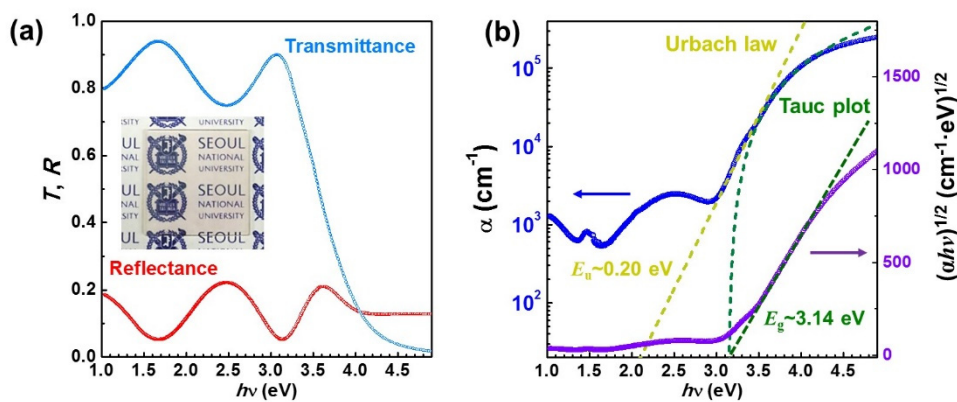


Figure 4.2 (a) Transmittance (T), reflectance (R), and (b) optical absorption spectra (α) of 160-nm-thick a-IGZO thin films deposited on quartz glass (3×3 cm²).

4.4. Microstructural changes

Figure 4.3 schematically shows the vertical structure of the devices and a cross-sectional TEM image of the devices in the as-fabricated state. Tungsten (W) as the non-reactive electrode material was selected, because it does not interact with nor diffuse into a-IGZO; its Gibbs free energy of oxide formation is higher than that of In_2O_3 , Ga_2O_3 , and ZnO (**Figure 4.4**)^[4.3]; and its melting temperature is sufficiently high^[1.41], thereby minimizing thermal diffusion into a-IGZO. The Ta-Al films on the top W electrode (TE) prevent interfacial interaction between a-IGZO and the ambient atmosphere because the native oxide formed passivates the film surface^[4.4]. The 160-nm-thick a-IGZO patches are covered with the top electrode (TE) consisting of the non-reacting W and the Ta-Al bilayer; thus, extrinsic reactions in addition to SR would be prevented during post-fabrication annealing.

Figure 4.5 shows high-resolution TEM images of the devices in the as-fabricated state (middle), after annealing at 400 °C for 1 h (left), and after annealing at 450 °C for 9 h. Moreover, and fast fast Fourier transform (FFT) analysis is conducted on a-IGZO thin films. The FFT area is marked by the white-dotted line. Under the most severe thermal stressing conditions in the experiments, i.e., annealing at 450 °C for 9 h, interface layers did not form and the amorphous phase was maintained not only in the bulk region but also in the W/a-IGZO interface regions.

Interestingly, the a-IGZO thickness was reduced from 162 nm to 152 nm (6.2% reduction) after annealing at 450 °C for 9 h, although these remarkable changes in the film thickness were not observed after annealing at 400 °C for 1 h. 6.2 % reduction would not be induced by experimental error due to the film roughness (**Figure 4.1**). Moreover, inter-diffusion between W and a-IGZO is not detected by EDS analysis as

Chapter 4: Development of the Devices Able to Regulate Extrinsic Reactions of Amorphous Oxide Semiconductors

shown in **Figure 4.6**. These results directly show that the free volume size reduction in a-IGZO was due to SR.

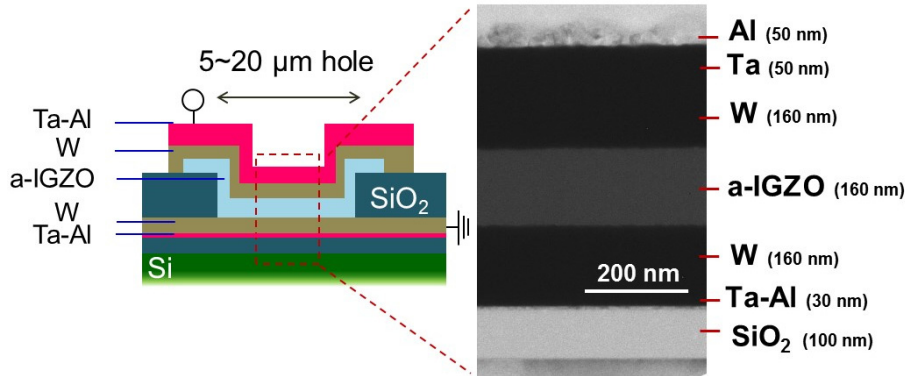


Figure 4.3 Schematic structure of the devices prevent extrinsic reactions used in this work. A cross-sectional TEM image of the devices in the as-fabricated state is also shown.

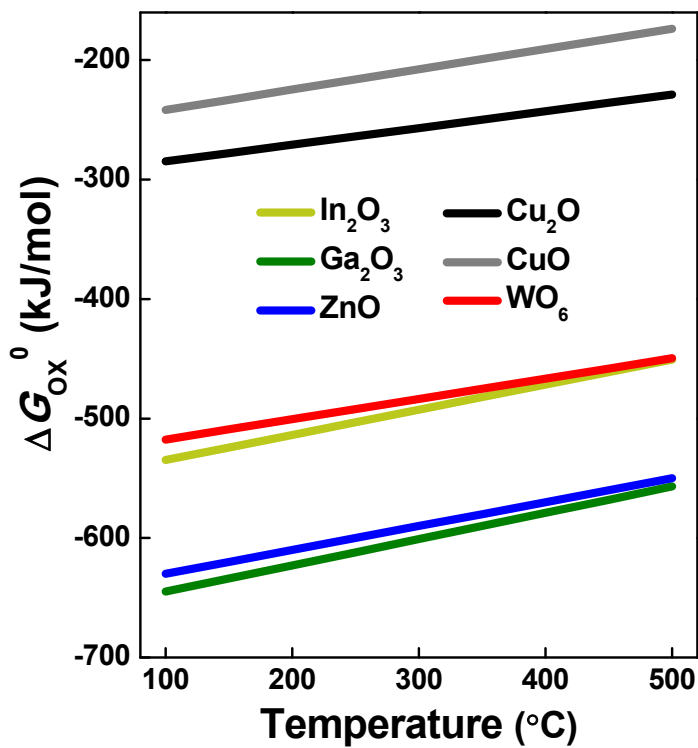


Figure 4.4 Gibbs free energy of oxide formation (ΔG_{ox}^0) of In, Ga, Zn, Cu, and W^[4.3].

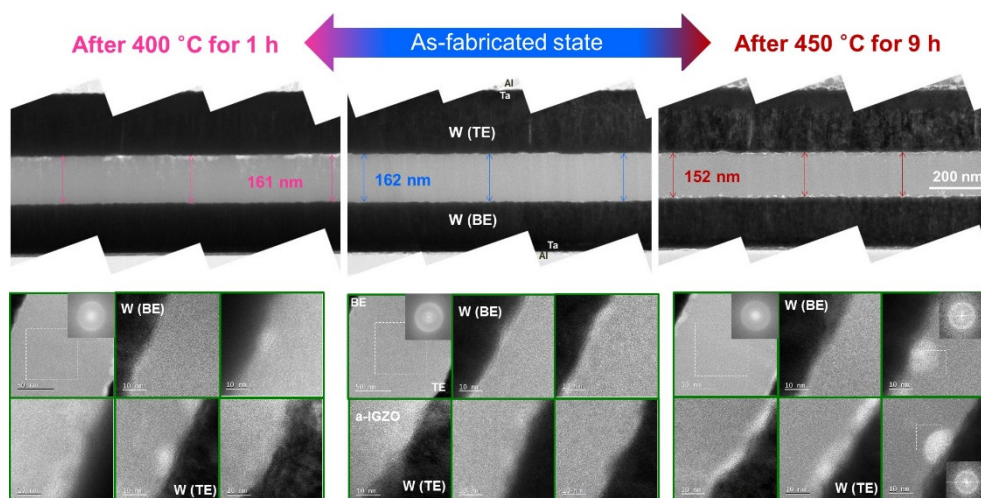


Figure 4.5 High-resolution TEM images and fast Fourier transform (FFT) diffractograms of the devices in the as-fabricated state (middle), after annealing at 400 °C for 1 h (left), and after annealing at 450 °C for 9 h (right). The FFT analysis area is marked by the white-dotted line.

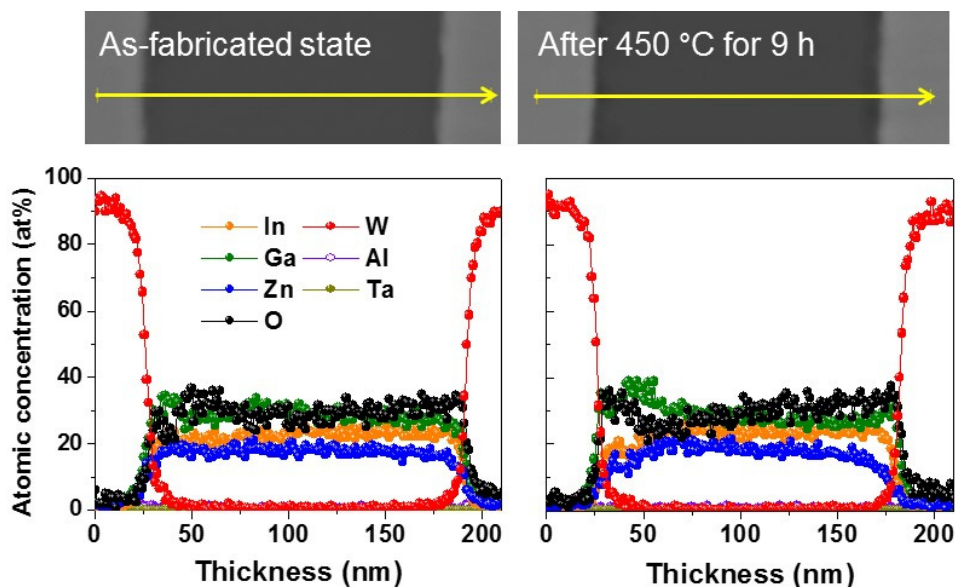


Figure 4.6 Magnified high-angle annular dark-field scanning TEM images (top) and EDS composition profiles of the devices along the arrow in the TEM images (bottom).

4.5. Chemical state changes

Figure 4.7 presents XPS composition profile of multilayer thin films (Al/Ta/W/a-IGZO/W/Ta/Al) in the as-fabricated state and after annealing at 450 °C for 9 h. The chemical composition of the deposited a-IGZO films was In:Ga:Zn=1:1.6:0.8 (an atomic ratio) and the values are nearly constant after annealing. Moreover, inter-diffusion was not detected, even though XPS composition analysis is more accurate than EDS analysis^[4.5,4.6]. After annealing, the shapes of the O 1s spectra, In 3d_{5/2} spectra, Ga 2p_{3/2} spectra, Zn 2p_{3/2} spectra, and W 4f_{7/2} spectra of a-IGZO were nearly identical to those of the as-fabricated state. Thus, changes in the chemical states of In, Ga, Zn, O (or V_O), and W in the a-IGZO were not detected (**Figure 4.8**). This finding suggests that a significant change in the V_O concentration did not occur during annealing.

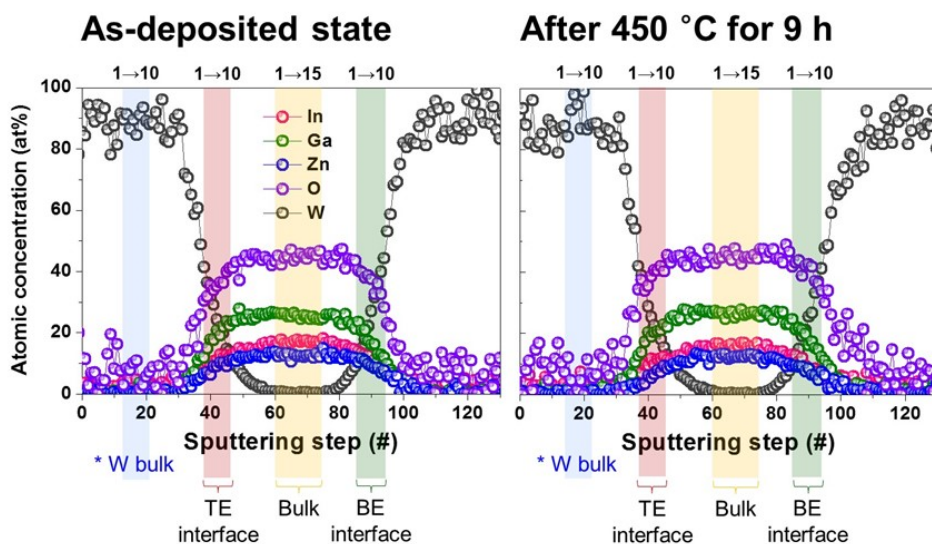


Figure 4.7 Composition XPS profiles of the Ta-Al/W/a-IGZO/W/Ta-Al thin films in the as-fabricated state (left) and after annealing at 450 °C for 9 h (right).

Chapter 4: Development of the Devices Able to Regulate Extrinsic Reactions of Amorphous Oxide Semiconductors

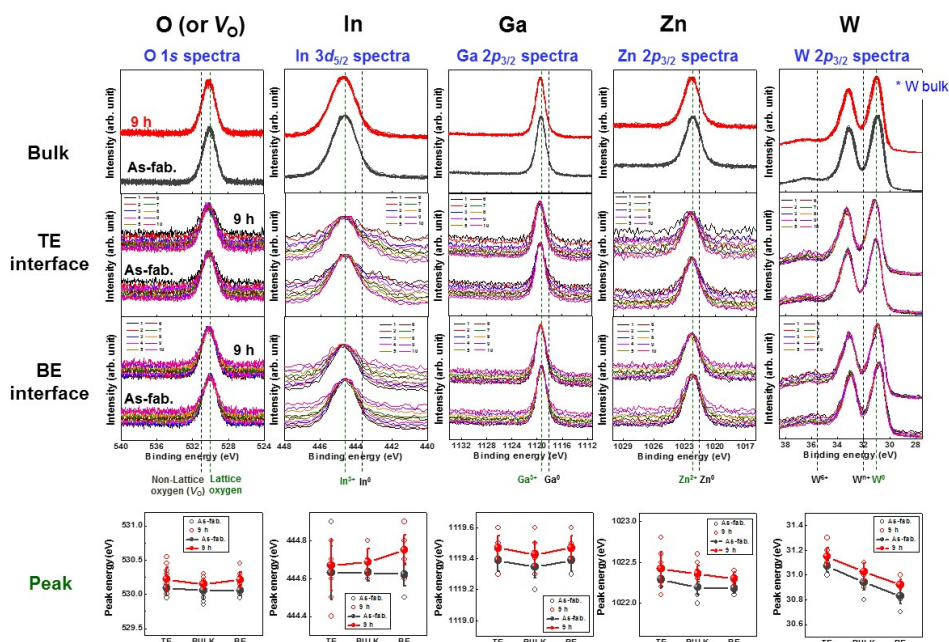


Figure 4.8 XPS results of O (V_O), In, Ga, Zn, and W in a-IGZO thin films. The location of each XPS data point in the depth profiles was marked in Figure 4.7(1→10 or 1→15). The XPS peaks are cited from refs. [1.36,4.7-4.11].

4.6. I - V characteristics changes

Figure 4.9a shows the representative I - V characteristics of the devices without Ta-Al and with Ta-Al in the as-fabricated state. When the Ta-Al passivation layer is not covered with the TE, the initial electrical conductance is lower than that of the devices covered with the Ta-Al bilayer. The Ta-Al bilayer is therefore inferred to reduce the contact resistance of the devices^[4.12]. Regardless of the Ta-Al passivation layers, rectifying behavior is observed. This behavior indicates that the electrical conduction of the devices is limited by the Schottky barrier at the W/a-IGZO contact. Ideally, a Schottky barrier is formed at the a-IGZO/W interface because the electron affinity of a-IGZO^[2.6] is lower than the work function of W^[4.13]. When a negative bias is applied to the TE, the electrical conductance is much higher than that under positive bias conditions, indicating that although the devices have a symmetric structure, an effective Schottky barrier is formed at the a-IGZO/BE interface rather than at the TE/a-IGZO interface. The Lower barrier height at TE interface than that at the BE interface may be due to the generation of interface states (e.g., O-deficiency-related defects and metal-induced gap states) during TE deposition^[2.17]. Therefore, the dominant conduction mechanism of the devices as fabricated is attributed to the Schottky barrier at the BE interface. The corresponding energy band diagram is depicted in **Figure 4.10a**.

The electron affinity of a-IGZO (χ_{a-IGZO}) is calculated using a simple linear relation between the electron affinities of In_2O_3 , Ga_2O_3 , and ZnO ^[2.6]. For the a-IGZO thin-film patches in the devices, the molar percentages of In_2O_3 , Ga_2O_3 , and ZnO are 0.24, 0.38, and 0.38, respectively, as shown in **Figure 4.7**. The value of χ_{a-IGZO} was found to be 3.99 eV. Because the work function of the metal W is 4.55 eV^[4.13], ideal the Schottky barrier height (Φ_B) at the W/a-IGZO interface is 0.56 eV. E_{FM} is the Fermi energy level

Chapter 4: Development of the Devices Able to Regulate Extrinsic Reactions of Amorphous Oxide Semiconductors

of W , and E_C is the conduction band minimum of a-IGZO. The width of the depletion region (W_D) in the a-IGZO thin-film patches can be calculated using the following equation^[2.16],

$$W_D = \sqrt{\frac{2\varepsilon_{\text{IGZO}}\varepsilon_0 V_{\text{bi}}}{qN_D}}, \quad (4.2)$$

where $\varepsilon_{\text{IGZO}}$ is the relative dielectric constant (10 for a-IGZO^[2.6]), ε_0 is the permittivity of vacuum, N_D is the doping concentration (or the concentration of positively charged defects) in the depletion region, and V_{bi} is the built-in potential.

V_{bi} is expressed as^[2.16]

$$V_{\text{bi}} = \frac{1}{q} \left[\Phi_B + k_B T \ln \left(\frac{N_D}{N_C} \right) \right], \quad (4.3)$$

Where q is the electron charge, k_B is the Boltzmann's constant, T is the absolute temperature N_C is the effective density of conduction band states ($5 \times 10^{18} \text{ cm}^{-3}$ for a-IGZO^[2.6]). According to the value of N_D in a-IGZO, the ideal W_D at RT is calculated as shown in **Figure 4.10b**. If N_D is below the value of $\sim 5 \times 10^{16} \text{ cm}^{-3}$, the W_D is wider than the physical thickness (160 nm) of the a-IGZO thin-film patches in the devices.

Carrier transport mechanisms at the Schottky contact are attributed to both thermionic emission and field emission (i.e., tunneling), and the contribution of the latter increases with higher carrier concentration in the semiconductors and/or defect density at the Schottky contact^[2.17]. When field emission is the dominant conduction mechanism, the current in the reverse bias regime exhibits exponential behavior as a function of the

Chapter 4: Development of the Devices Able to Regulate Extrinsic Reactions of Amorphous Oxide Semiconductors

applied voltage, whereas weak-voltage-dependent-reverse current is observed under thermionic emission^[2.17,2.18]. Because the devices in the as-fabricated states indicate that the reverse current is weakly dependent on the applied voltage, thermionic emission dominates the conduction mechanism.

The I - V characteristics of Schottky-thermionic emission under forward bias conditions with $V > 3k_B T / q$ are^[2.16,2.17]

$$I_{\text{FORWARD}} = I_s \exp\left(\frac{qV - I_{\text{FORWARD}} R_s}{nk_B T}\right), \quad (4.4)$$

where I_s is the saturation current, n is the ideality factor, and R_s is the series resistance of the devices. I_s is expressed as^[2.16,2.17]

$$I_s = AA^* T^2 \exp\left(-\frac{\Phi_B}{k_B T}\right), \quad (4.5)$$

where A is the contact area and A^* is the effective Richardson constant (theoretically $=40.8 \text{ Acm}^{-2}\text{K}^{-2}$ for a-IGZO^[2.6]). When the Schottky diode parameters of the devices are compared, the R_s value of devices without Ta-Al is much larger than those of the devices with Ta-Al, whereas the differences in Φ_B and n are negligible (**Figure 4.9b**). Therefore, the difference in R_s induces the difference in the I - V characteristics between devices with and without Ta-Al. Because R_s includes the contact resistance of the devices, this finding supports the finding that the contact resistance of the devices with Ta-Al is smaller than that of the devices without Ta-Al.

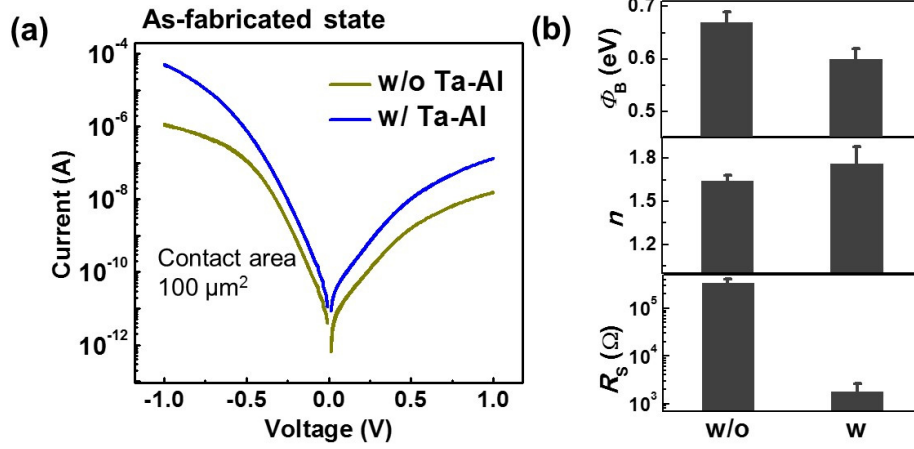


Figure 4.9 (a) Typical I - V characteristics of the devices with Ta-Al layer and the device without Ta-Al in the as-fabricated state. (b) Schottky diode parameters for the devices: Schottky barrier (Φ_B), ideality factor (n), and series resistance (R_s).

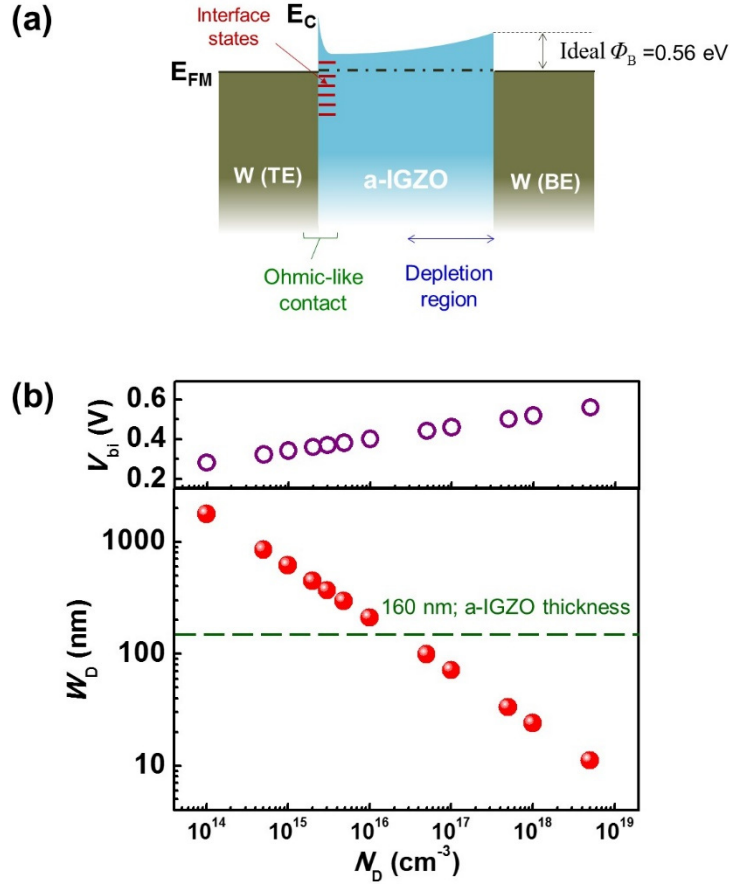


Figure 4.10 (a) Schematic energy band diagram of the W/a-IGZO/W structures. (b) The variation in V_{bi} and W_D with respect to N_D in a-IGZO thin films at RT.

Chapter 4: Development of the Devices Able to Regulate Extrinsic Reactions of Amorphous Oxide Semiconductors

Figure 4.11a shows the typical I - V characteristics of the devices with and without Ta-Al after annealing at 450 °C. When the Ta-Al bilayer is covered with the TE, the I - V characteristics become symmetric with increasing electrical conductance. This behavior indicates that dominant conduction mechanism of the devices is not Schottky thermionic conduction anymore. Details of the changes in dominant conduction mechanism changes are consulted in **Section 5**.

I - V characteristics of the devices with Ta-Al are not affected by ambient atmosphere conditions; vacuum (10^{-3} Pa), N_2 ambient (working pressure of 10 and 10^3 Pa, respectively), N_2/O_2 (95vol%/5vol%), and N_2/H_2 (95vol%/5vol%). However, the devices without Ta-Al produce asymmetric I - V curves and the electrical conductance is larger than that of the devices with Ta-Al under reducing ambient atmosphere (**Figures 4.11a and 4.11b**). As annealing time increases from 1 to 4 h, electrical conductance of the devices without Ta-Al increases more, while that of the devices with Ta-Al remains constant (**Figure 4.11c**). In particular, the electrical conductance in the negative bias region is much higher than that in the positive bias region. These results suggest that when the self-passivated Ta-Al bilayer is not covered with a W electrode, a reduction in the a-IGZO occurs starting from the TE/a-IGZO interface, consequently increasing n_e in the a-IGZO in addition to the SR-driven increase in the concentration of V_{OS} in the shallow-donor state. Because n_e in the a-IGZO is non-uniformly distributed (i.e., n_e in the a-IGZO gradually decreases from the TE interface to the BE interface because a O diffusion profile forms due to the reduction reaction at the TE interface), asymmetric I - V curves are generated. The devices without Ta-Al show the highest electrical conductance after annealing under N_2/H_2 ambient, which may be induced by the additional inclusion of H donor in a-IGZO^[1,51]. Interestingly, electrical conductance as well as the degree of asymmetry of the devices without Ta-Al decreased under N_2/O_2

Chapter 4: Development of the Devices Able to Regulate Extrinsic Reactions of Amorphous Oxide Semiconductors

ambient (i.e., oxidizing ambient). After annealing under N_2/O_2 ambient, the color of W TE became dark (i.e., oxidation of W), whereas that of Ta-Al was not changed as shown in **Figure 4.12**. These results strongly support that a-IGZO in the devices without Ta-Al interact with ambient atmosphere. Therefore, the Ta-Al passivation layer is an important factor in the investigation of the SR-driven doping effect because it successfully prohibits extrinsic reaction with the ambient atmosphere (e.g., redox reactions). Absolute concentration of V_{OS} in a-IGZO in the devices with Ta-Al remains effectively unchanged regardless of the post-fabrication annealing conditions and the dominant origin of the increase in electrical conductance as well as n_e is believed to be the changes in electronic states of V_{OS} in deep-donor or electron-trap states to shallow-donor states due to SR. The resultant devices show that the changes in electrical properties is not affected by annealing ambient. Moreover, composition profile and chemical state of the elements in the devices are not changed after annealing. These results strongly suggest that the fabricated devices effectively inhibit the extrinsic reactions in the a-IGZO and maintain absolute V_{OS} concentration in a-IGZO during annealing.

Chapter 4: Development of the Devices Able to Regulate Extrinsic Reactions of Amorphous Oxide Semiconductors

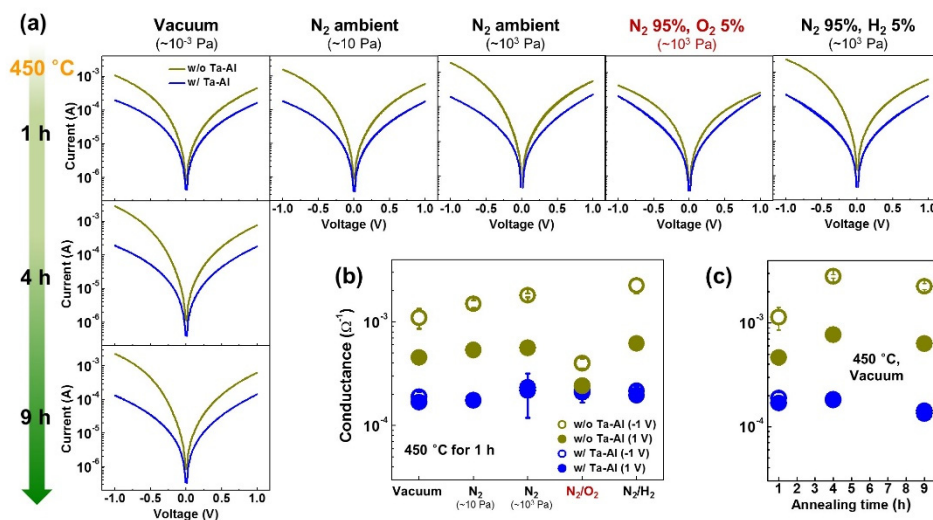


Figure 4.11 The changes in the (a) I - V characteristics and (b-c) electrical conductance in the devices without Ta-Al and with Ta-Al with respect to ambient atmosphere as well as annealing time at 450 °C.

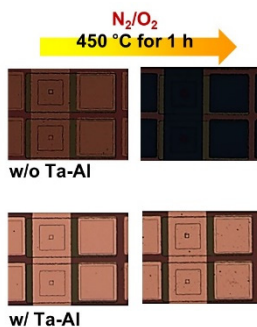


Figure 4.12 Plain optical images of the devices after at 450 °C for 9 h under N₂/O₂ ambient.

4.7. Summary

Structure of AOSs-based devices are designed to regulate *undesirable extrinsic* reactions and to measure the changes in electrical properties of AOSs solely induced by atomic rearrangement or migration. After annealing at 450 °C for 9 h, which condition is the severe thermal stressing conditions in our experiments, neither interface reactions, crystallization, nor interdiffusion occurred in the a-IGZO, which was confirmed using TEM analysis. Changes in the chemical states of In, Ga, Zn, O (or V_O), and W in the a-IGZO were not detected after annealing by XPS. When the Ta-Al bilayer was not covered with TE, I - V characteristics after annealing were affected by ambient atmosphere. Electrical conductance of the devices without Ta-Al under reducing ambient is higher than that of the devices under oxidizing ambient. However, the changes in I - V characteristics of the devices with Ta-Al appear negligible with respect to annealing ambient atmosphere. These results strongly suggest that the fabricated devices effectively inhibit the extrinsic reactions in the a-IGZO and maintain absolute V_O concentration in a-IGZO during annealing.

Interestingly, the a-IGZO film thickness was reduced by 6.2 % after annealing at 450 °C for 9 h. These results directly show that the densification (i.e., free volume size reduction) in a-IGZO occurs due to SR.

In addition to verification of the performance of the devices, chemical states, structural properties, and optical properties of as-deposited a-IGZO thin-films used in the devices as well as multi-layer thin-films were investigated. Chemical composition of the deposited a-IGZO films was In:Ga:Zn=1:1.6:0.8 (an atomic ratio) measured by

Chapter 4: Development of the Devices Able to Regulate Extrinsic Reactions of Amorphous Oxide Semiconductors

XPS. Roughness of a-IGZO thin films are less than 1-nm for both 40- and 160-nm-thick films, although the substrate is composed of Ta-Al/SiO₂/Si substrate as the same configuration of the devices. The film density and optical band gap of the films are 5.8 g·cm⁻³ and 3.14 eV. Moreover, tail-like optical absorptions are observed beneath the band gap. This confirms that subgap states (e.g., deep donor states near the valence band maximum, continuous trap level) primarily exist in a-IGZO.

CHAPTER 5

Structural Relaxation-Driven Intrinsic Doping

5.1. Introduction

V_{OS} as an *intrinsic* dopant in AOSs, have various electronic states, either shallow-donor, deep donor, or electron trap state, and are determined by the local atomic structure^[1.3,1.22,1.24]. Because SR can affect the V_O electronic states by changing the local atomic conditions, n_e is changed by the degree of SR through the changes in the electronic state of V_{OS} . Therefore, understanding the effects of SR on n_e and the concentration of V_{OS} in the shallow-donor state is important for developing device-level a-IGZO applications and reliable resistance to thermal stress. Here, we investigate the change in the electronic states of V_{OS} in a-IGZO due to SR without ambient artifacts by using the devices able to prevent extrinsic reaction as we developed (**Section 4**). Based on the annealing conditions, the devices exhibited different conduction mechanisms, i.e., Schottky-thermionic, Ohmic, and Poole-Frenkel conduction. In this study, SR-driven doping effect was quantified by analyzing the conduction mechanism of the devices after their exposure to various annealing conditions.

5.2. Experiments

Devices used in this section are same as the devices in **Section 4**. The devices were annealed at temperatures between 300 and 450 °C for up to 16 h under vacuum (10^{-3} Pa) condition. For the annealing process, the temperature increased at a heating rate of 5 °C/min from RT to the target annealing temperature, followed by maintenance of the target temperature for the specified duration. After annealing, the I - V characteristics of the devices were measured with respect to the substrate temperature. The substrate temperature was varied from RT to 96 °C. At each annealing condition, 10-50 devices were considered to evaluate the changes in the electrical properties of a-IGZO.

5.3. I - V Characteristics changes

Figure 5.1 presents the semi-logarithmic I - V curves of the devices in the as-fabricated state and that the devices after annealing at 300 °C for 1 h, all of which were measured at RT. Rectifying behavior is observed in as-fabricated devices. This behavior indicates electrical conduction is dominated by Schottky barrier at the W/a-IGZO contact. Details of the energy band diagram of the devices are shown in **Figure 4. 10 in Section 4**. After annealing at 300 °C for 1 h, the asymmetric I-V curves were maintained; however, the electrical conductance of the devices increased relative to the as-fabricated state. This finding indicates that the conduction of the devices was still dominated by the Schottky barrier at the BE interface but that the barrier height decreased after the annealing^[2,17,5.1,5.2]. The Schottky barrier height decreased because the concentration of V_{OS} in the shallow-donor state (N_{DS}) in the a-IGZO increases after annealing; thus, the net positive charges in the depletion region increased^[2,17,5.1,5.2]. Because changes in the

concentration of O (or V_{OS}) in the a-IGZO is prohibited in the devices during annealing, neutral V_{OS} in the deep-donor state in the a-IGZO would be transformed into a positively charged shallow-donor state, increasing the N_{DS} .

A remarkable counter figure-eight hysteretic I - V loop is observed in the voltage range from -1 to 1 V after annealing. This characteristic shape of I - V hysteresis indicates that the Schottky barrier height or width at the BE interface is modulated with respect to the bias polarity in association with electron trapping/detrapping in the vicinity of BE interface^[5.1]. Under a negative bias, electron detrapping occurs, and net positive charges in the depletion region increase, causing decrease in the height or width of the Schottky barrier and increased electrical conductance. However, when a positive bias is applied, positively charged electron-trap states become neutral as electrons are captured, increasing the height or width of the Schottky barrier. This result indicates electron trap sites as well as V_{OS} in the shallow-donor state dominate the positively charged depletion region. Because the hysteresis disappeared under the voltage range of -0.2 to 0.2 V, the degree of the Schottky barrier height/width modulation was dependent on the magnitude of current. In the as-fabricated state, as the voltage sweep range increased produce more current in the devices, the I - V curves also exhibited counter figure-eight hysteretic behavior as observed in **Figure 5.2**. This finding suggests that a sufficient number of V_{OS} act as electron traps in the a-IGZO to affect electrical conduction in both the as-fabricated and even post-annealing at 300 °C for 1 h

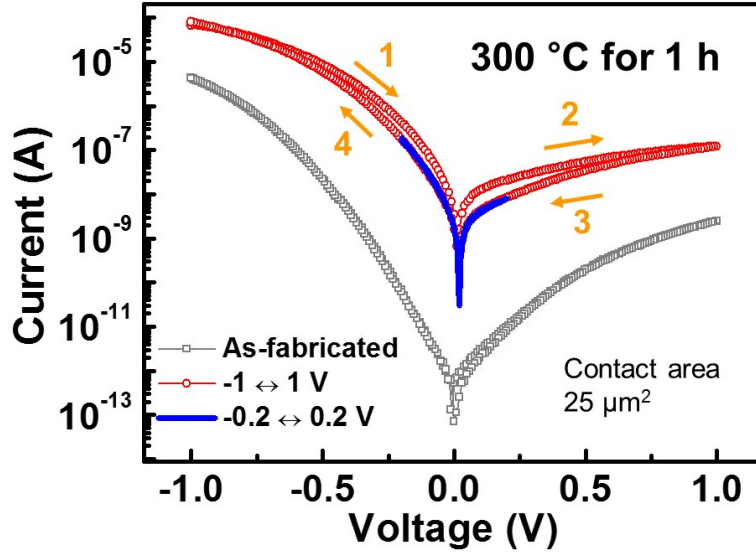


Figure 5.1 The representative current-voltage (I - V) characteristics of the devices in the as-fabricated state and after annealing at 300 °C for 1 h (measured at RT). In the as-fabricated state, rectifying I - V curves are observed even though the devices have a symmetric structure. After annealing at 300 °C for 1 h, counter figure-eight hysteric I - V curves are observed in the voltage range from -1 to 1 V.

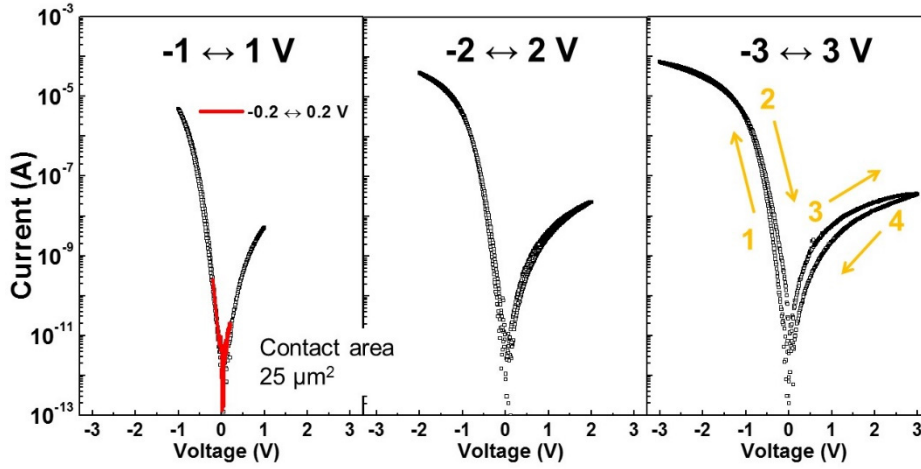


Figure 5.2 The changes in the I - V characteristics of the devices in the as-fabricated state as a function of the voltage sweep range (measured at RT). In the voltage sweep range of -3 V to 3 V, a counter figure-eight hysteric loop is clearly observed. As the voltage sweep range increases, the hysteresis area increases.

Figure 5.3 presents a map of the I - V curves of the devices with respect to the post-fabrication annealing conditions, in which the temperature was varied from 300 °C to 450 °C for 1 to 16 h. At 300 °C, the rectifying and hysteretic I - V characteristics and similar electrical conductance are observed even after an annealing time of 16 h. As the annealing temperature increases to 400 °C, the electrical conductance of the devices increases more than at 300 °C. Moreover, the hysteresis of the I - V curves disappeared after annealing for 1 h. These results suggest that as the annealing temperature increases to 400 °C, the N_{DS} increases, whereas the concentration of V_{OS} that act as electron traps become negligible with respect to the V_{OS} in the shallow-donor state. Previous studies report that extra subgap states located ~ 0.2 eV below the conduction band minimum (E_C) induce hysteretic I - V behavior in as-fabricated a-IGZO thin-film transistors (TFTs)^[1,42]. Moreover, the post-annealing process annihilates the subgap states, resulting in the enhancement of the electrical performance of the TFTs, including the disappearance of the hysteresis^[1,42]. Therefore, V_{OS} in the electron trap states are the origin of the extra subgap states in a-IGZO and are annihilated during post-fabrication annealing through SR.

At an annealing temperature of 400 °C, the asymmetry of the I - V curves decreases with longer annealing time. Symmetric I - V curves appeared after an annealing duration longer than 9 h, beyond which the I - V characteristics changed little up to 16 h. At 450 °C, symmetric I - V curves were observed after annealing for only 1 h, and the electrical conductance increased even further. These I - V characteristics were maintained up to an annealing time of 9 h. The I - V characteristics can be summarized as follows. The electrical conductance of the devices increases at higher annealing temperatures. Symmetric I - V curves appeared with annealing temperature higher than 400 °C. The changes in the electrical properties of a-IGZO due to SR appear to be determined by the

Chapter 5: Structural Relaxation-Driven Intrinsic Doping

annealing temperature rather than the annealing time; the annealing time-independent behavior can be another piece of evidence that time-dependent extrinsic reactions (e.g., diffusion of impurities, redox reactions) did not occur during annealing.

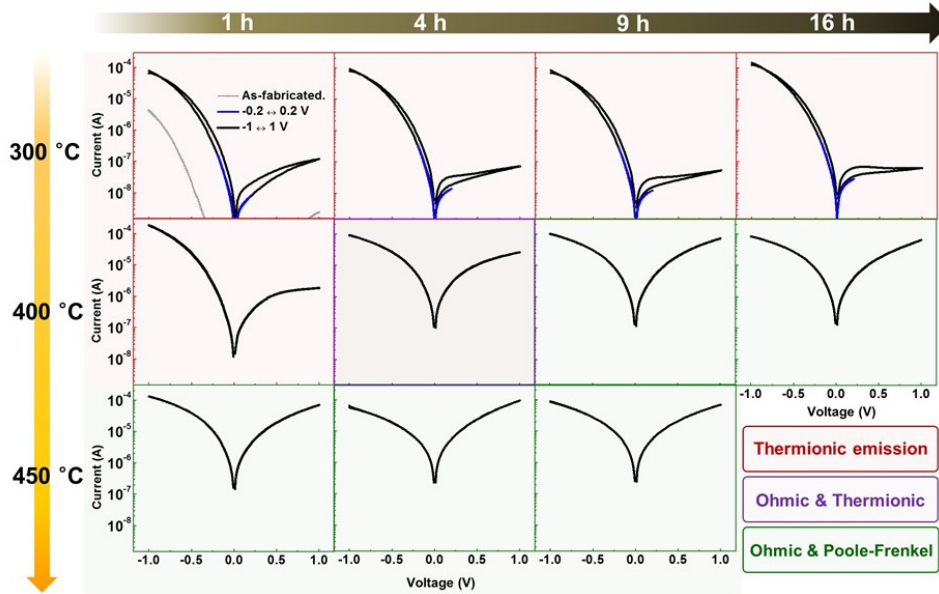


Figure 5.3 I - V map of the devices considering both the annealing temperatures from 300 to 450 °C and the annealing times from 1 to 16 h. The contact area of the devices was 25 μm^2 . After annealing at 300 °C, the rectifying and hysteretic behaviors with similar electrical conductance are observed even after the annealing time of 16 h. After annealing at 400 °C, the hysteresis disappears with an increase in the electrical conductance, and the I - V curves become symmetric as the annealing time increases. When the I - V curves become symmetric, the I - V characteristics are nearly constant regardless of further annealing. After annealing at 450 °C, symmetric I - V curves are observed even after an annealing time of 1 h.

5.4. Conduction mechanism analysis

5.4.1. Schottky-thermionic emission

At an annealing condition of 300 °C, the dominant conduction mechanism of the devices is related to overcoming the Schottky barrier at the BE interface as noted above. Reverse bias conduction is weakly dependent on applied voltage. Thus, dominant conduction mechanism of the devices after annealing at 300 °C is Schottky-thermionic emission likewise in the case of as-fabricated devices (**Figure 4.9 in Section 4**). **Figure 5.4** shows the change in the Schottky diode parameters, including the Schottky barrier height (Φ_B), ideality factor (n), and series resistance (R_s) of the devices after annealing based on thermionic theory under forward bias condition^[2,16]. After annealing at 300 °C, the Φ_B decreased with n increasing compared with that in the as-fabricated state, implying increased contribution of the field emission on the Schottky conduction^[4,15]. Therefore, certain V_{OS} at the deep-donor level are transformed into shallow donors and/or electron traps after annealing, and the n_e in a-IGZO and/or the defect density at the vicinity of the BE interface increases. This finding is consistent with the explanation of the origin of the increased electrical conductance in the annealed devices relative to that of as-fabricated. Furthermore, decrease in the R_s of the devices after being annealed at 300 °C may indicate that the n_e in a-IGZO increases relative to the as-fabricated state due to annealing-related SR.

The variation in Φ_B based on the applied voltage history appears to agree with the origin of the counter figure-eight I - V curve. The V_{OS} in the electron-trap state significantly affect the net positive charges in the depletion layer in the vicinity of the a-IGZO/BE interface. The increase in Φ_B and the decrease in n associated with the

application of a positive bias demonstrates that the net positive charges in the depletion region decrease as electron trapping occurs. Based on such characteristic changes in the Schottky parameters, Φ_B to decrease and n to increase with further annealing time are expected. However, the corresponding kinetics becomes dramatically retarded after an annealing time of 1 h. Therefore, the SR effects on the electrical properties of a-IGZO are primarily related to the annealing temperature rather than the annealing time. To quantify N_{DS} in the a-IGZO after annealing at 300 °C, the I - V characteristics under the reverse bias condition have been considered. When the applied voltage is higher than the value of $3k_B T/q$, the reverse current ($I_{REVERSE}$) is given by^[2,16]

$$I_{REVERSE} = I_s \exp \left(\frac{0.34 q (q / \varepsilon_{IGZO} \varepsilon_0)^{3/4} N_D^{1/4} (V + V_{bi} - k_B T / q)^{1/4}}{k_B T} \right), \quad (5.1)$$

where k_{bB} is Boltzmann's constant, q the electron charge, T the absolute temperature, I_s the saturation current, ε_{IGZO} the relative dielectric constant (10 for a-IGZO^[2,6]), the permittivity of vacuum, V_{bi} the built-in potential, and N_D the concentration of the positively charged defects in the depletion region. The value of N_D was extracted using equations (4.2), (4.3), and (5.1) and the values of Φ_B and $I_{REVERSE}$ at 0.2 V ($>3k_B T/q$) from the non-hysteretic I - V curves in the voltage range from -0.2 to 0.2 V. **Figure 5.5** shows the dependence of $I_{REVERSE}$ at 0.2 V and Φ_B of the devices after annealing at 300 °C for 1 h on the contact area and substrate temperature. Although $I_{REVERSE}$ at 0.2 V increases with the contact area and the substrate temperature, the value of N_D remains relatively constant. Therefore, the dominant conduction mechanism of the devices corresponds to thermionic emission. Slight changes in N_D with respect to the contact area and substrate temperature may be induced that the conduction mechanism of the

devices deviated from ideal thermionic emission theory; the value of n is larger than 1, and I_{REVERSE} does not exhibit a linear relationship with the contact area (i.e., the slope of the solid lines in **Figure 5.5** are 0.85 and 0.72 for the devices after annealing at 300 °C for 1 h and at 400 °C for 1 h, respectively). After annealing at 300 °C for 1 h, the N_D in the a-IGZO of the devices was determined to be $9.98 (\pm 2.52) \times 10^{15} \text{ cm}^{-3}$. In addition to 1 h, the N_D for the a-IGZO following annealing at 300 °C for a range of annealing times up to 16 h is shown in **Figure 5.11**. Similar to the I - V characteristics, the N_D is nearly constant with further annealing, suggesting that the SR effect on the N_D in a-IGZO is not dependent on the annealing time. At the annealing condition of 400 °C, thermionic emission is the dominant conduction mechanism up to an annealing time of 4 h. Compared with 300 °C, Φ_B decreased whereas n increased (**Figure 5.4**). These results suggest that higher N_D values are expected in a-IGZO at annealing temperatures of 400 °C^[2,17]. The N_D in the a-IGZO after annealing at 400 °C for 1 h was determined to be $3.28 (\pm 1.32) \times 10^{16} \text{ cm}^{-3}$ (**Figure 5.5**). Thus, as the annealing temperature increased from 300 °C to 400 °C, the N_D increased approximately 3 times due to SR. Based on the observed hysteretic behavior, the extracted N_D value after annealing at 300 °C represents the summation of the N_{DS} and the concentration of V_{OS} in the electron-trap state. After annealing at 400 °C, however, the hysteresis disappears, and the N_D corresponds to N_{DS} . With increasing annealing time up to 4 h, Φ_B decreases and n increases (**Figure 5.4**) and The N_{DS} value is calculated to be $9.43 (\pm 4.77) \times 10^{16} \text{ cm}^{-3}$ at RT (**Figure 5.11**). In addition to the analysis of the reverse current characteristics, investigation of the capacitance (C) characteristics in the Schottky diodes is an effective method for extracting N_{DS} values and trap energy levels from semiconductors^[2,16,5,3]. C - V characteristics of the devices are introduced in **Section 5.5**.

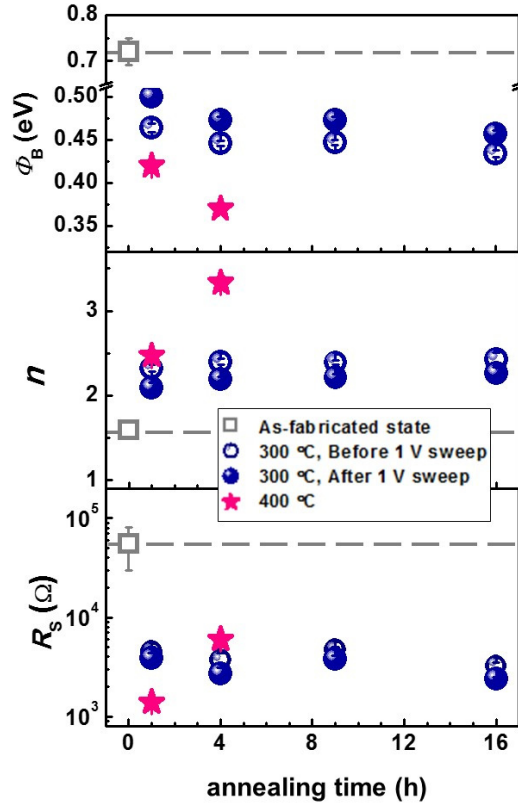


Figure 5.4 The variations in the Schottky diode parameters in the devices after annealing at 300-400 °C: Schottky barrier (Φ_B), ideality factor (n), and series resistance (R_s) at RT. The contact area of the devices was 25 μm^2 .

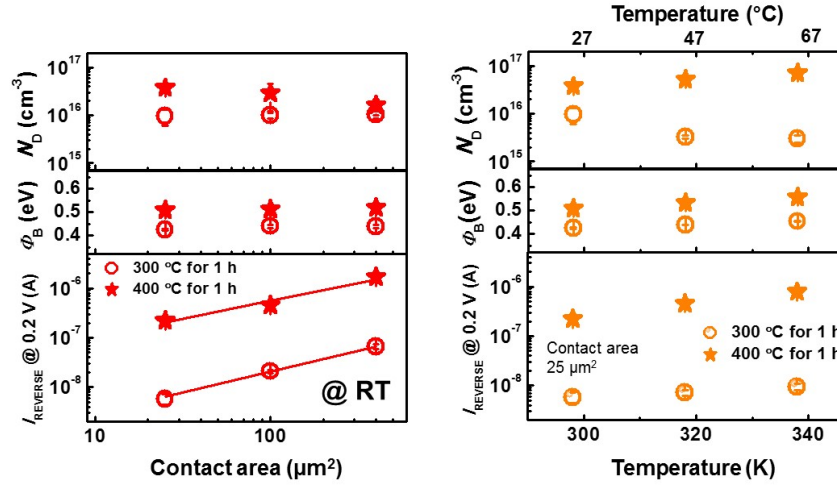


Figure 5.5 Dependence of the reverse current (I_{REVERSE}), Φ_B , and the concentration of positively charged defects in the depletion region of a-IGZO (N_D) on the contact area (left) and temperature (right).

5.4.2. Ohmic and Poole-Frenkel conduction

The devices after annealing at 400 °C for 4 h exhibit Ohmic conduction in the low voltage region (<0.07 V) as shown in **Figure 5.6a**. The slope of the double-logarithmic I - V curve is close to 1, whereas the slope of the devices after 400 °C for 1 h deviate from 1. Moreover, the devices that exhibit symmetrical I - V curves also follow Ohmic conduction in the low voltage region. As the applied voltage increased, the conduction mechanism transformed to non-Ohmic conduction. The symmetric I - V curve can be explained by the change of the Schottky contact resistance at the TE/a-IGZO interface to a value similar to that of the a-IGZO/BE interface or the transition of the predominate conduction mechanism to bulk-limited conduction. The candidates responsible for such non-Ohmic and bulk-limited conduction mechanisms in the devices are Poole-Frenkel (P-F) conduction and space-charge limited-current (SCLC)^[2,16]. Considering the magnitude of the applied electric fields in the a-IGZO thin-film patches and the temperature dependence of the electrical conductance (**Figures 5.8a and 5.8b**), the conduction mechanisms based on tunneling can be neglected^[2,16]. The P-F conduction is given as^[2,19,2,20]

$$I_{\text{P-F}} \propto E \exp \left[\frac{1}{rk_{\text{B}}T} \left(q \sqrt{\frac{qE}{\pi \epsilon_{\text{IGZO}} \epsilon_0}} - \Phi_{\text{PF}} \right) \right], \quad (5.2)$$

where E is the applied electric field (approximately V divided by 160 nm), Φ_{PF} is the P-F barrier, and r is a constant ranging from 1 to 2. **Figure 5.6b** presents the $\log(I/V)$ vs. \sqrt{E} plot for the devices under positive bias conditions. The parameter r is derived from the slope of the $\log(I/V)$ vs. \sqrt{E} curve in the range from 22.5 to

62.5 kV/cm. The devices after annealing at 400 °C for 1 and 4 h are not well fitted by the orthodox P-F conduction theory. However, since r for the devices showing symmetric I - V curves varies between 1 and 2, P-F conduction is the dominant conduction mechanism for the devices that exhibit symmetric I - V curves in the high voltage region (0.36-1.0 V). Thus, the conduction mechanism of the devices with symmetric I - V characteristics can be expressed as follows: (i) In the low-field region, thermally excited electrons from V_{OS} in the shallow-donor state primarily flow above the E_C . (ii) As the magnitude of E increases, the free electrons from V_{OS} in the shallow-donor state, assisted by the electric field and P-F conduction, become predominant. To determine the dominant mechanism of the devices that exhibit nonpolar electrical conductance whether exhibiting the SCLC mechanism or not, the applied voltage range was increased to create large increases in the conductance of the devices, as shown in **Figure 5.7a**. The electrical conductance of the devices after annealing at 450 °C for 9 h sharply increased at a voltage of 4.3 V. **Figures 5.7b** and **5.7c** present double-logarithmic I - V plots and the slopes of the corresponding curves, respectively. In the low-voltage region (<0.07 V), the conduction mechanism is Ohmic conduction, as noted in the main text. As the voltage increases, the value of $d\log(I)/d\log(V)$ increases. After a sharp increase in the conductance, the devices exhibit Ohmic conduction, not $I \propto V^2$. These results suggest that the SCLC mechanism is not the dominant conduction mechanism of the devices.

The conduction mechanism consists of Ohmic conduction in the low-field region and P-F conduction in the high-field region, which is analogous to reports on the conduction mechanisms of several amorphous materials including a-IGZO^[2,20,5,4,5,5]. Because the Φ_{PF} corresponds to $E_C - E_D$ where E_D is the location of the donor energy level^[2,20], the

energy level of the V_{OS} at the shallow-donor states can be estimated from the temperature dependence of the P-F current.

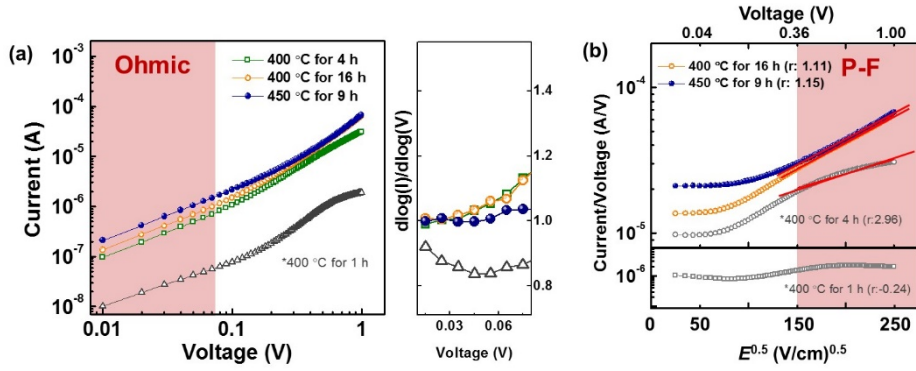


Figure 5.6 (a) Double logarithmic I - V plots and the slope of the corresponding plots to determine the Ohmic conduction. (b) $\log(I/V)$ - $E^{0.5}$ plots to identify the P-F conduction.

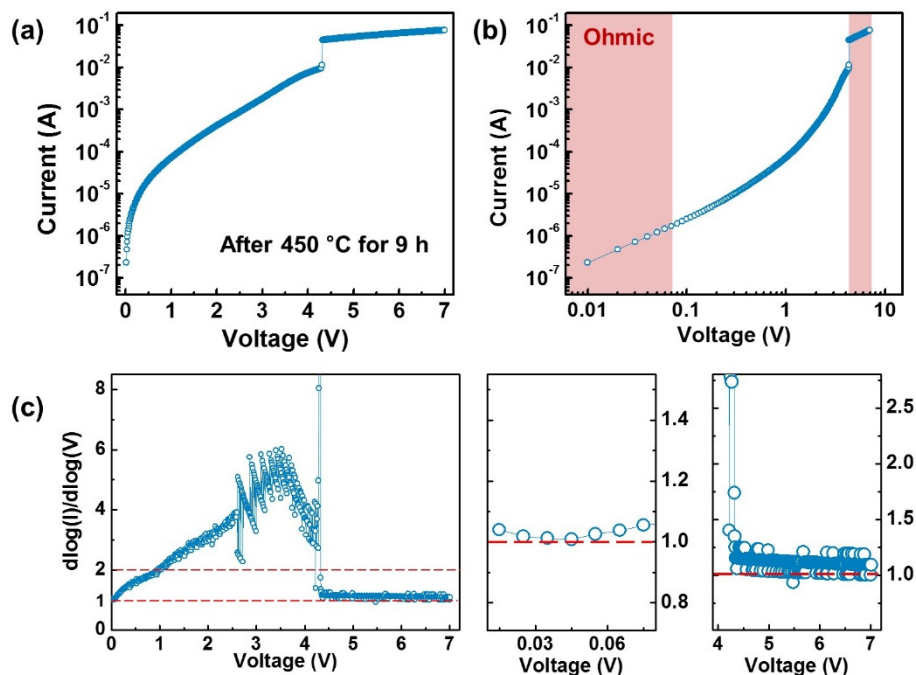


Figure 5.7 Representative I - V characteristics of the devices after annealing at 450 °C for 9 h. **(a)** semi-logarithmic plot, **(b)** double-logarithmic plot, and **(c)** the slope of the corresponding double-logarithmic I - V curve.

5.4.3. Extraction of free electron/doping concentration

Figure 5.8a shows the temperature dependence of the Ohmic resistance in the devices. As the annealing temperatures increase, the resistance decreases. The Arrhenius equation fits these values well. The temperature dependence of the Ohmic resistance is primarily affected by the change in n_e in a-IGZO^[2,17,2,18]. The value of n_e is expressed as^[4,15]

$$n_e = N_C \exp\left(\frac{E_F - E_C}{k_B T}\right), \quad (5.3)$$

where E_F is the Fermi level. Thus, the slope of the solid lines in **Figure 5.8a** represent $(E_F - E_C)/k_B T$, and n_e in a-IGZO at RT can be estimated to be N_C as reported in ref. 4.13. **Figure 5.9** shows the value of n_e in a-IGZO after annealing at 400 and 450 °C, respectively. After annealing at 400 °C for 4 h, the values of n_e at RT is calculated to be $4.56 (\pm 1.52) \times 10^{16} \text{ cm}^{-3}$ based on the results of the changes in the Ohmic resistance (**Figure 5.8a**). At an annealing time of 16 h, the value of n_e scarcely changes [$4.72 (\pm 0.65) \times 10^{16} \text{ cm}^{-3}$]. However, at the higher annealing temperature of 450 °C (for 9 h), the slope of the resistance changes decreases (**Figure 5.8a**), and the value of n_e increases to $4.53 (\pm 1.14) \times 10^{17} \text{ cm}^{-3}$. Therefore, with higher annealing temperatures, N_{DS} increases because V_{OS} in the deep-donor or electron-trap states are transformed into shallow donors due to SR. Thus, n_e is more strongly affected by the annealing temperature than the annealing time.

In addition to the Ohmic resistance, the P-F parameter Φ_{PF} and the P-F current (at 1 V) are plotted with respect to the substrate temperature in **Figure 5.8b**. The constant

value of r regardless of the temperature demonstrates that P-F conduction is the dominant conduction mechanism for the devices. The Φ_{PF} was extracted from the slope of the solid lines in **Figure 5.8b**. After annealing at 400 °C for 16 h, the Φ_{PF} was determined to be 0.12 (± 0.01) eV, and Φ_{PF} exhibits a lower value of 0.11 (± 0.01) eV after annealing at 450 °C for 9 h (**Figure 5.9**). These extracted values are similar to those in the previous reports on the donor energy levels in a-IGZO (~ 0.11 eV)^[5,6]. Moreover, the shallower donor energy levels associated with higher Φ_{PF} values can be explained by the screening effect^[5,6,5,7]. Therefore, the estimated value of the energy level of V_{OS} at the shallow-donor state through analysis of P-F conduction is highly reliable. Because the value of $E_{\text{C}}-E_{\text{D}}$ is higher than the value of $k_{\text{B}}T$, the field-enhanced thermal excitation of free electrons (i.e., P-F conduction) is possible.

Because the location of E_{F} and E_{D} are known, the value of N_{DS} in a-IGZO after annealing at 400-450 °C can be estimated as follows. The actual donation of the free electrons from the shallow donors states at a given substrate temperature is given by^[2,16]

$$n_{\text{e}} = N_{\text{DS}} \left[1 / \left(1 + \exp \left(\frac{E_{\text{F}} - E_{\text{D}}}{k_{\text{B}}T} \right) \right) \right]. \quad (5.4)$$

It should be noted that pre-exponential constant was modified from 2 to 1 considering that major electron donor is V_{O} which can 2 electrons, not 1 electron^[1,24].

Based on the results in **Figure 5.9**, N_{DS} in a-IGZO after annealing at 400-450 °C is extracted. The cumulative distribution of N_{DS} in a-IGZO (as well as the electrical parameters related to N_{DS}) is shown in **Figure 5.10** and **Figure 5.11** presents N_{DS} in a-IGZO according to post-fabrication annealing conditions. The value of N_{DS} in a-IGZO after annealing at 400 °C is $\sim 10^{17} \text{ cm}^{-3}$ and increases to $\sim 10^{19} \text{ cm}^{-3}$ as the annealing

temperature increases to 450 °C. The exact value of N_{DS} in a-IGZO after annealing at 300 °C could not be estimated because the estimated value of N_D is the summation of and the V_O concentration in the electron-trap state. Nevertheless, we suggest that the increases as the annealing temperature increases, because of SR. The SR-driven doping effect is weakly affected by the annealing time and strongly affected by the annealing temperature. Because SR causes a reduction in the free volume size in amorphous materials^[1.37,1.38,1.49], we conclude that the microscopic origin of the SR-driven doping effect is related to increase in the concentration of V_O s located in the dense network, and more V_O s at the deep-donor or electron-trap states changed to the shallow-donor state. From the kinetics perspective, the atomic mobility (i.e., inverse of viscosity) in amorphous materials increases with increasing annealing temperature, which follows an Arrhenius relationship^[1.38]. In this regard, at higher annealing temperatures, a greater reduction in free volume size is expected in the limited time, as illustrated in **Figure 1.10**. Therefore, the thin films of a-IGZO increase in density as the annealing temperatures increases because of SR, as shown in **Figure 4.5**.

The saturation behavior of the SR-driven doping effect indicates that the reduced free volume size is strongly determined by the annealing temperature rather than the annealing time. The free volume reduction likely occurs in a manner similar to the densification kinetics of porous amorphous films^[2.15], in which most of the densification is completed during the early stage of the annealing process with a sharp decrease in the densification rate as a function of annealing time. Similarly, the degree of film densification is determined by the annealing temperature rather than the annealing time. The atomic mobility of amorphous materials is related to the free volume size as well as the thermal energy, and the mobility decreases with decreases in the free volume size^[1.38,1.39]. Thus, the weak annealing time dependence of SR-driven doping suggests

that the atomic mobility in a-IGZO further decreases during SR and that the reduction rate of the free volume size becomes negligible. These SR results may provide a key to determining the origin of changes in the conduction mechanism, i.e., from thermionic emission to Ohmic and P-F conduction at low and high fields, respectively. Ideally, as n_e increases to the order of 10^{17} cm^{-3} , thermionic emission should be the predominant conduction mechanism^[2,16]. At 400 °C, although N_{DS} in a-IGZO was nearly constant with increasing annealing time, a transition in the conduction mechanism was observed. We believe that significantly more SR is expected at the interfaces (between a-IGZO and the W electrode) than in the bulk a-IGZO because atomic mobility at interfaces is generally higher than that in the bulk^[1,41]. Likewise, the crystallization of a-IGZO occurs at the interface under lower temperatures than in the bulk a-IGZO^[1,37]. This phenomenon may result in sufficiently high n_e at the interface, which in turn leads to a negligible Schottky barrier, thereby facilitating electrical conduction.

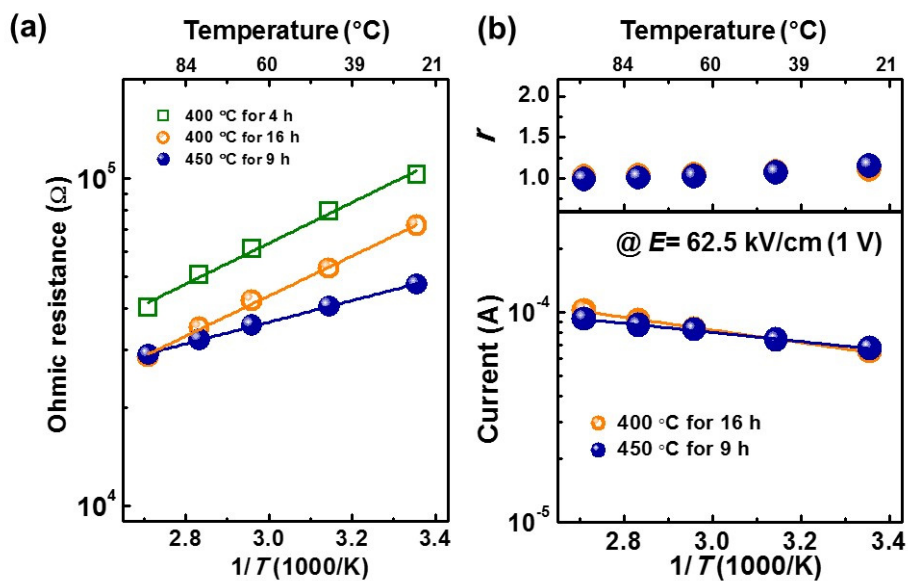


Figure 5.8 Arrhenius plots of (a) Ohmic resistance and (b) the current at $E=62.5$ kV/cm with the P-F parameter, r .

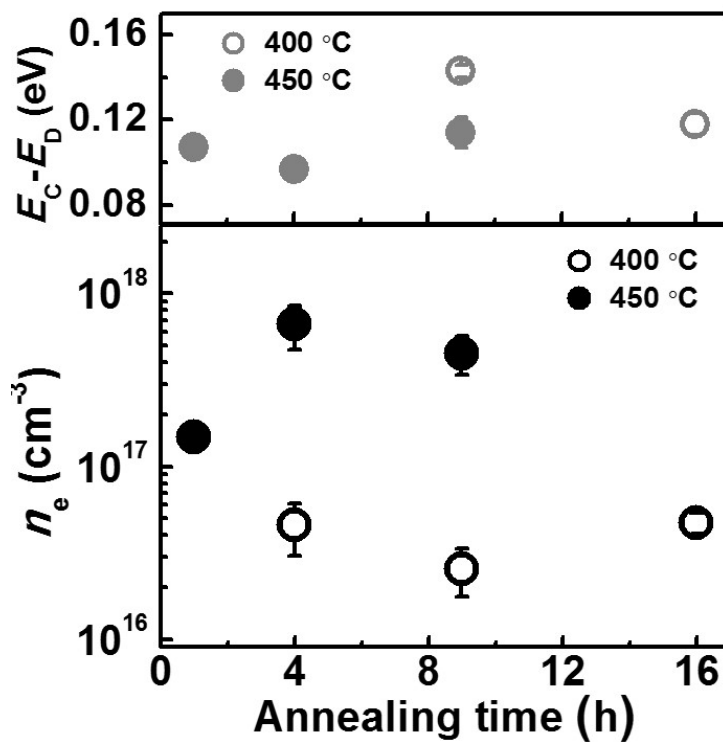


Figure 5.9 The changes in the free electron concentration (n_e) and shallow-donor energy level ($E_C - E_D$) of V_{OS} in a-IGZO after annealing at 400 and 450 °C.

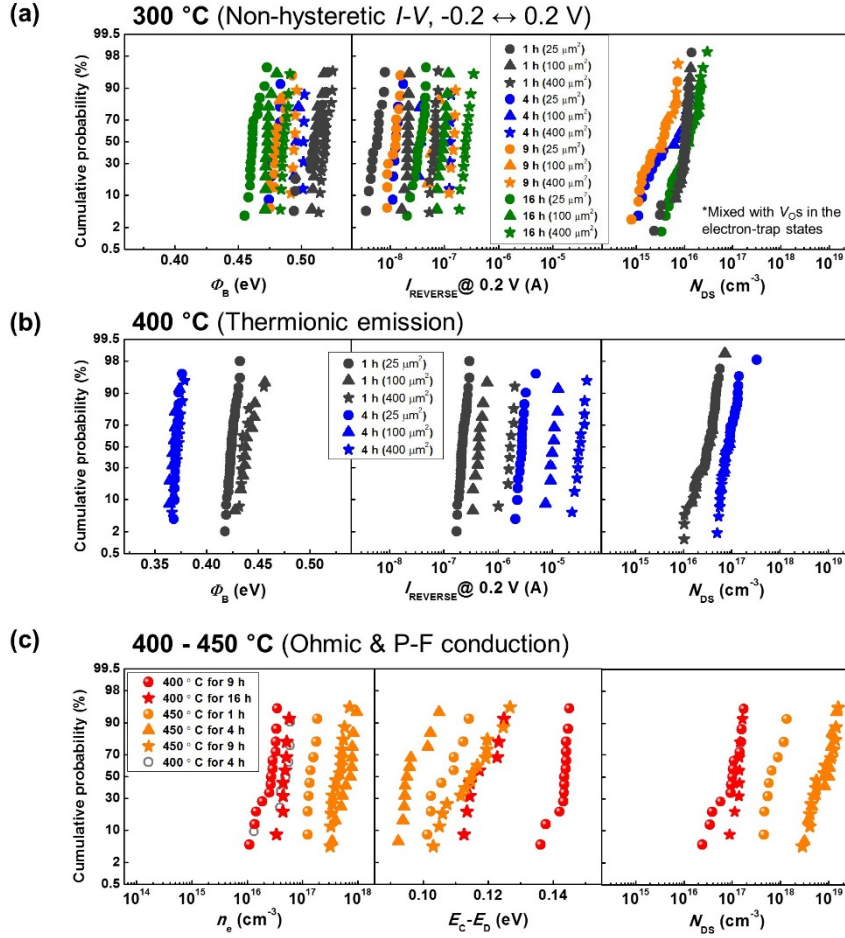


Figure 5.10 Cumulative distribution of the electrical parameters of the devices following the method described in the JEDEC standard JESD 37. Φ_B , I_{REVERSE} , and N_{DS} (or N_D) of the Schottky conducting devices **(a)** after annealing at 300 °C and **(b)** after annealing at 400 °C. **(c)** n_e , $E_C - E_D$, and N_{DS} of the devices that show Ohmic and Poole-Frenkel conduction at low and high voltages, respectively.

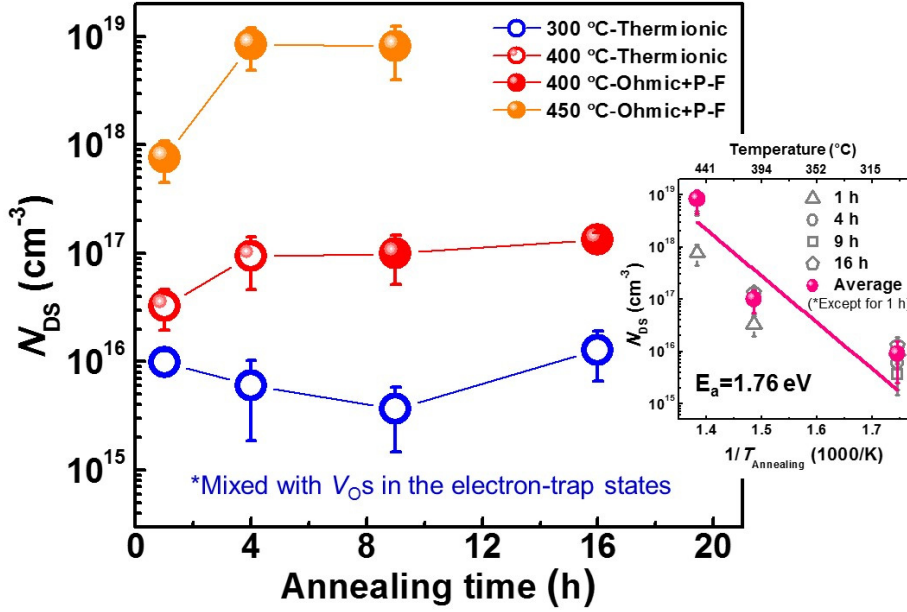


Figure 5.11 The V_O concentration at the shallow-donor state (N_{DS}) in a-IGZO with respect to post-fabrication annealing conditions.

In addition to the devices composed of 160-nm thick a-IGZO, the devices composed of 40-nm-thick a-IGZO thin-film patches were conducted the same experiments^[4,28]. Although the initial characteristics of the I - V curves are different, the tendency of the changes in the conduction mechanism and N_{DS} with respect to post-fabrication annealing conditions are similar to those in the devices made from 160-nm-thick a-IGZO thin-film patches (**Figure 5.12**)^[5,8]. Therefore, these results concerning the SR-driven doping effect represent universal characteristics of a-IGZO.

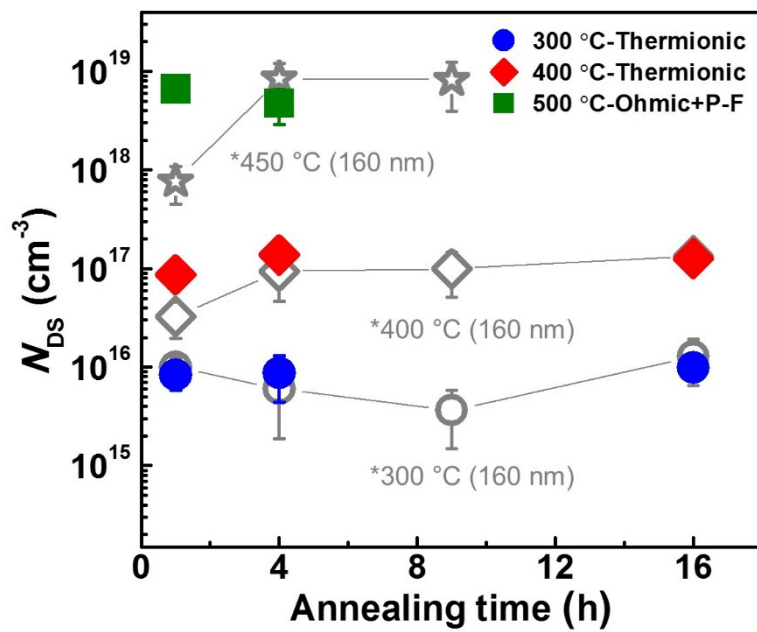


Figure 5.12 N_{DS} values in a-IGZO for the 40-nm devices with respect to post-fabrication annealing conditions.

The inset in **Figure 5.11** presents an Arrhenius plot of N_{DS} . We consider the average values in our experiments, except the 1 h results. Then, using **Figure 5.11**, the activation energy (E_a) was found to be approximately 1.60 eV. Because the occurrence of SR accompanies internal atomic rearrangement, ionic bonding energy in a-IGZO may be responsible for the calculated activation energy. The average bond energies in a-IGZO are reported to be 2.0, 1.7, and 1.5 eV for Ga-O, In-O, and ZnO, respectively^[1,34]. During annealing, SR results in the densification of the a-IGZO thin-films (**Figures 5.13 and 4.5**) and a decrease in the free volume size in a-IGZO in association with greater V_{OS} in the dense network. SR-driven doping effect is expressed in terms of the atomic rearrangement in the devices and the changes in the density of states in a-IGZO in **Figures 5.14a and 5.14b**, respectively. The density of states in a-IGZO in the as-deposited state was obtained from refs. 1.3 and 2.10. Therefore, V_{OS} in the deep-donor or electron-trap states are transformed to the shallow-donor state. In this respect, SR-driven doping can be used to tune the electrical conductivity of amorphous oxide semiconductors. The fact that the SR-driven doping effect exhibited a stronger dependence on the annealing temperature than on the annealing time may be used to optimize the resistance of electronic devices to thermal stress.

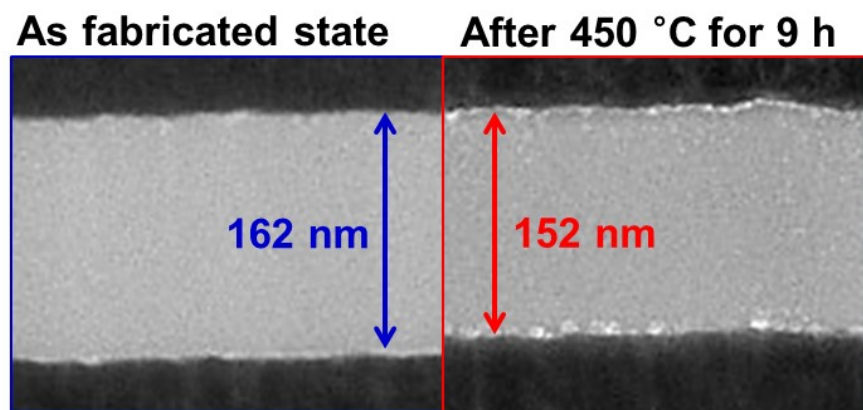


Figure 5.13 Thickness changes in a-IGZO thin-film patches after annealing at 450 °C for 9 h. 6.2% thickness reduction was observed by HRTEM.

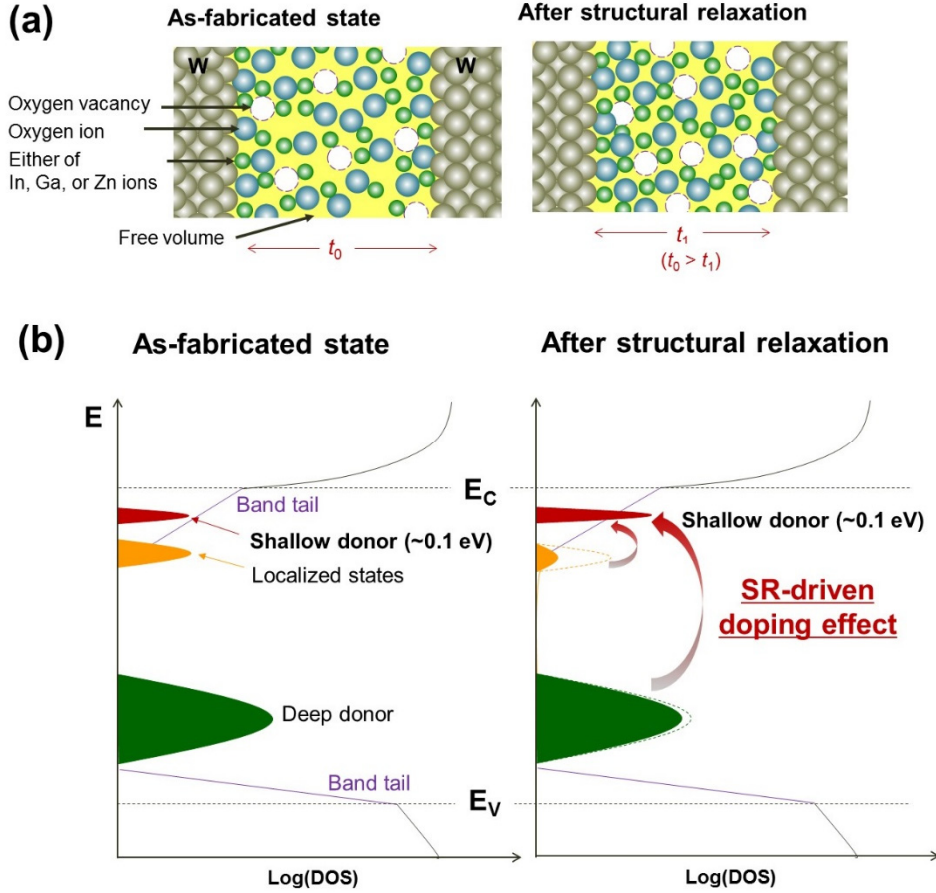


Figure 5.14 Illustrations of the **(a)** atomic rearrangement of a-IGZO in the devices and **(b)** the change of density of states (DOS) in a-IGZO due to SR. The configuration of DOS in a-IGZO in the as-fabricated state was obtained from refs. 1.3 and 2.10.

5.5. C - V characteristics of the Schottky conducting devices

Figure 5.15 shows the schematics of the cross-sectional view of the devices. The main purpose of our study is unravelling the structural relaxation (SR) effect on the electronic state of V_{OS} in amorphous oxide semiconductors without extrinsic reactions. To prevent the interaction of a-IGZO with the ambient atmosphere, the top electrode (TE) area is large enough to cover the a-IGZO thin-film patches. Furthermore, a 500-nm-thick SiO_2 layer was used to prevent an electrical connection between the TE and the bottom electrode (BE). The overlapping area between the TE and BE is $(110 \times 110) \mu m^2$ and causes a bias to be applied on not only (1) the a-IGZO in the square hole region but also on (2) a-IGZO/ SiO_2 multilayers and (3) on the SiO_2 isolation layer (**Figure 5.15**). As a result, the devices are composed of (1) Schottky diodes, (2) metal/oxide/semiconductor (MOS) capacitors, and (3) metal/oxide/metal (MOM) capacitors, and the C characteristics of the devices are affected by Schottky diodes, MOS capacitors and MOM capacitors (i.e., *parasitic* capacitance).

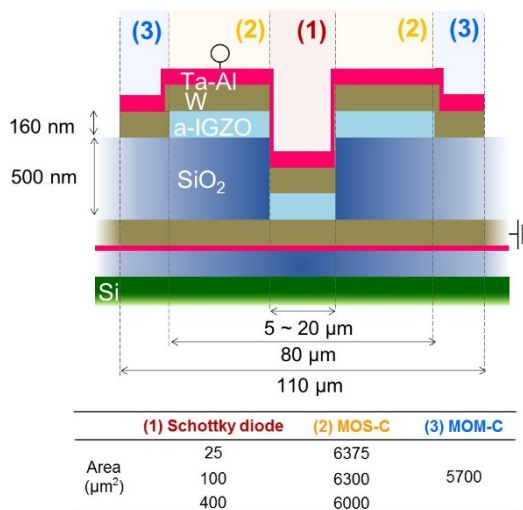


Figure 5.15 Schematics of the cross-sectional view of the devices. Because the devices are designed to prevent extrinsic reactions, three different capacitors [(1) Schottky diode, (2) MOS capacitor, and (3) MOM capacitor] are connected in parallel.

Figure 5.16 depicts the energy band diagram of the (1) Schottky diodes, (2) MOS capacitors, and (3) MOM capacitors based on the band parameters of W^[4,13], SiO₂^[5,9,5,10] and a-IGZO^[2,5]. A notable fact is that the TE/a-IGZO interface forms an Ohmic-like contact (i.e., poor Ohmic contact). Although Φ_B at the TE interface is lower than that at the BE interface due to the interface states induced by the TE formation process^[2,17], the contact resistance is quiet high and interfacial capacitance ($C_{\text{Interface}}$) would exist, as shown in **Figure 5.16**. When poor Ohmic contact is formed at the TE interface and exists at the TE interface, the accurate C characteristics of the Schottky diodes cannot be measured^[5,11-5,13]. Thus, high-quality Ohmic contacts are needed to utilize the C characteristics of the devices for the investigation of N_D ^[5,11-5,13] and the trap energy level^[5,3]. In general, high-quality Ohmic contacts at the metal oxide semiconductors are formed by interfacial redox reactions^[2,17]; when an easily oxidized metal (e.g., Ti or Al) contacts the metal oxide semiconductors, it uptakes the oxygen from the metal oxides and generate V_{OS} at the metal/oxide interfaces. As a result, N_D is locally increased at the interface, and the contact resistance decreases^[2,17]. However, the post-annealing process to induce SR can cause continuous redox reactions at the high-quality Ohmic contacts, which affects the changes in the bulk properties of the amorphous oxide thin-films in addition to the SR effect. Therefore, poor Ohmic contact formation at the inert metal electrode (W)/a-IGZO interface is inevitable in when investigating the SR effect and suppresses the interaction between the metal electrodes and a-IGZO.

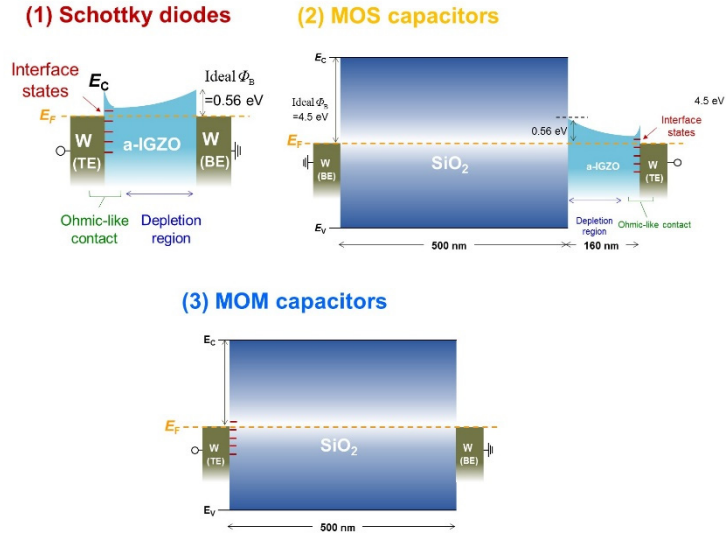
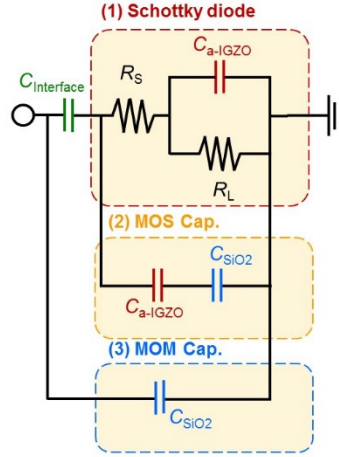


Figure 5.16 Schematic energy band diagrams of the capacitors. High-quality Ohmic contacts are not formed at TE/a-IGZO interfaces.

Figure 5.17 presents the equivalent circuits of the devices in this work. (1) Schottky diodes, (2) MOS capacitors, and (3) MOM capacitors are connected in parallel manner. Schottky diodes consist of a junction capacitance ($C_{a\text{-IGZO}}$), a leakage resistance (R_L), and a series resistance (R_S). The MOS capacitor is serially connected with $C_{a\text{-IGZO}}$ and the SiO_2 isolation layer (C_{SiO_2}). The $C_{\text{Interface}}$ at the TE/a-IGZO contact may also be non-negligible. Therefore, extraction of the accurate values of N_D and the trap energy level in a-IGZO would be difficult to determine from the C characteristics of the devices due to parasitic capacitance and poor Ohmic contacts. To verify our predictions, we calculated and measured the C - V characteristics of the devices, as shown in **Figures 18-20**.



- C_{a-IGZO} : Capacitance of the depletion region in a-IGZO thin-film patches
 - C_{SiO2} : Capacitance of 500-nm-thick SiO_2 layer
 - R_L : Leakage resistance of Schottky diodes
 - R_S : Series resistance of Schottky diodes
- * $C_{interface}$: Capacitance of interface states at TE/a-IGZO contact

Figure 5.17 Equivalent circuits of the device. Interfacial capacitance at the TE/a-IGZO contact may also affect the C characteristics of the devices in addition to the Schottky diodes, MOS capacitors, and MOM capacitors.

Figure 5.18 presents the calculated C - V characteristics of the devices with respect to the Schottky contact area. The total capacitance of the devices was calculated by the parallel connection of the three devices, the Schottky diodes, MOS capacitors, and MOM capacitors, and $C_{\text{Interface}}$ was neglected for simplification of the calculations. C_{SiO_2} , which is a component of the MOS capacitors and MOM capacitors, is $6.9 \times 10^{-9} \text{ F} \cdot \text{cm}^{-2}$, the dielectric constant of SiO_2 is $3.9^{[5,9]}$ and the layer thickness is 500 nm. The $C_{\text{a-IGZO}}$ is given as follows^[2,16]:

$$C_{\text{a-IGZO}} = \frac{A \epsilon_{\text{IGZO}} \epsilon_0}{W_D}. \quad (5.5)$$

where A is the Schottky contact area ($25\text{-}400 \mu\text{m}^2$) and W_D is the depletion width. $C_{\text{a-IGZO}}$ is dependent on the W_D in a-IGZO, which is changed by the applied voltage (V) and is expressed as follows^[2,16]:

$$W_D = \sqrt{\frac{2 \epsilon_{\text{IGZO}} \epsilon_0}{q N_D} (V_{\text{bi}} - V - k_B T / q)}. \quad (5.6)$$

Under the forward and reverse bias conditions, W_D decreases and increases, respectively. When $N_D = 1.0 \times 10^{17} \text{ cm}^{-3}$ and $\Phi_B = 0.37 \text{ eV}$, a-IGZO thin-film patches are fully depleted at the reverse voltage of 2 V, and the depletion region vanishes at the forward voltage of 0.25 V (**bottom in Figure 5.18a**). When $N_D = 1.2 \times 10^{16} \text{ cm}^{-3}$ and $\Phi_B = 0.50 \text{ eV}$, the a-IGZO thin-film patches are already fully depleted without bias application, and the depletion region vanishes at a forward voltage of 0.35 V (**bottom in Figure 5.18b**).

When equation (5.5) is integrated with equations (4.3) and (5.6), $A^2/C_{\text{a-IGZO}}^2$ can be expressed as

$$\frac{A^2}{C_{\text{a-IGZO}}^2} = \frac{2[(\Phi_{\text{B}} + k_{\text{B}}T \ln(N_{\text{D}} / N_{\text{C}}))/q - V - k_{\text{B}}T / q]}{q\epsilon_{\text{IGZO}}\epsilon_0 N_{\text{D}}}. \quad (5.7)$$

Thus, N_{D} and Φ_{B} can be derived from the slope of the $A^2/C_{\text{a-IGZO}}^2$ - V curve and V -intercept value, respectively^[2,16]. However, $C_{\text{a-IGZO}}$ values are small or comparable to the capacitances of the MOS capacitors and MOM capacitors (**middle in Figure 5.18**). This means that the measured total C values of the devices are not dominated by the Schottky diodes. When the $A^2/C_{\text{a-IGZO}}^2$ - V curves are plotted from the total C values, the slopes of the curves and V -intercept values are deviated from the Schottky diodes only (**top of Figure 5.18**). Therefore, the values of N_{D} and Φ_{B} extracted from C - V results from the devices may be inaccurate due to parasitic capacitance.

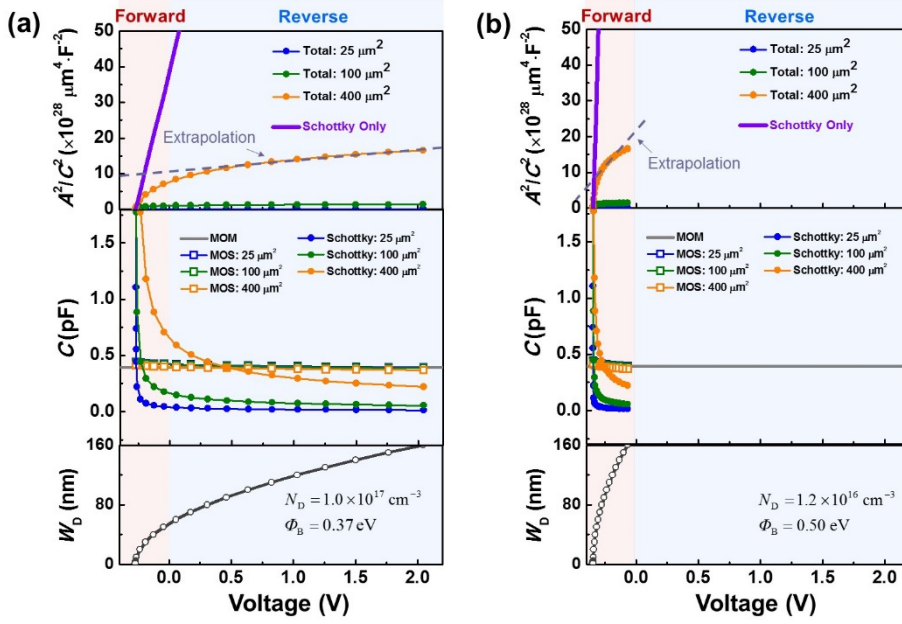


Figure 5.18 Changes of W_D in a-IGZO thin-film patches (bottom), C of MOM, MOS capacitors and Schottky diodes (middle), and A^2/C^2 in the devices with respect to applied bias (top) **(a)** N_D of $1.0 \times 10^{17} \text{ cm}^{-3}$ and Φ_B of 0.37 eV. **(b)** N_D of $1.2 \times 10^{16} \text{ cm}^{-3}$ and Φ_B of 0.50 eV. The total C of the devices is significantly affected by the MOM and MOS capacitances which are comparable or larger than C of the Schottky diodes. Therefore, the values of N_D and Φ_B extracted from the A^2/C^2 - V curves are inaccurate.

Figure 5.19 shows the I - V and the corresponding C - V results of 25-400 μm^2 devices in the as-fabricated state, measured by an Agilent 1500A semiconductor device parameter analyzer. Direct current (DC) I - V characteristics were measured under the same conditions used for **Section 5.2**. When the C - V characteristics are measured, the alternating current (AC) voltage was swept from -1 to 1 V on the TE with a test signal of 50 mV at 0.01-1 MHz, and the BE was grounded. As the contact area increases, the electrical conductance increases, maintaining the rectifying behavior (**Figure 5.19a**). Moreover, the electrical conductance increases linearly with the Schottky contact area, as shown in the inset of **Figure 5.19a**. This suggests that the Schottky conductance dominantly affects the electrical conductance of the devices. However, the corresponding C - V characteristics of the devices are weakly dependent on the contact area (**Figure 5.19b**). Although, the C value of the 400 μm^2 devices is larger than that of the 25- and 100- μm^2 devices, the percent increase is smaller than that of the contact area. The Weak dependence of C on the Schottky contact area would be induced by the parasitic capacitances of the devices (**Figure 5.18**). Moreover, the measured C values are one order of magnitude larger than the calculated C values, which implies that the significantly affects the total capacitance of the devices. Interestingly, “negative” C values are obtained at the forward bias region for only the 25 μm^2 devices. This behavior have been observed at Schottky diodes with poor Ohmic contacts^[5.13], which suggests that the devices have poor Ohmic contacts. As the Schottky contact area increases, negative C values are not measured. As the contact area increases, the contact resistance decreases^[5.13], resulting in a decrease in the effect of poor Ohmic contacts on the C - V characteristics of the devices.

The C - V curves are converted into A^2/C^2 - V curves, as shown in **Figure 5.19c**. Only the 400 μm^2 -devices show that the A^2/C^2 value decreases as the forward bias increases, and

the value is saturated under the reverse bias condition. Based on equation (5.7), the value is $1.3 \times 10^{19} \text{ cm}^{-3}$ and Φ_B is 0.98 eV. These results are inconsistent with the from Hall measurement ($<10^{16} \text{ cm}^{-3}$) and Φ_B from I - V analysis ($0.72 \pm 0.02 \text{ eV}$). Moreover, the saturation of the A^2/C^2 value under the reverse bias condition implies that the depletion region is fully depleted to 160 nm, which is the physical thickness of the a-IGZO thin-film patches. If the N_D and Φ_B values are the same for the C - V results, W_D is 9.28 nm, which is much thinner than the thickness of the a-IGZO patches in the devices (160 nm). This means that the A^2/C^2 value should increase with the reverse bias. Thus, N_D and Φ_B are overestimated from the C - V results, affected by not only parasitic capacitances but also by the poor Ohmic contacts of the devices. Therefore, the extraction of N_D and Φ_B through C - V measurement is not appropriate in this study.

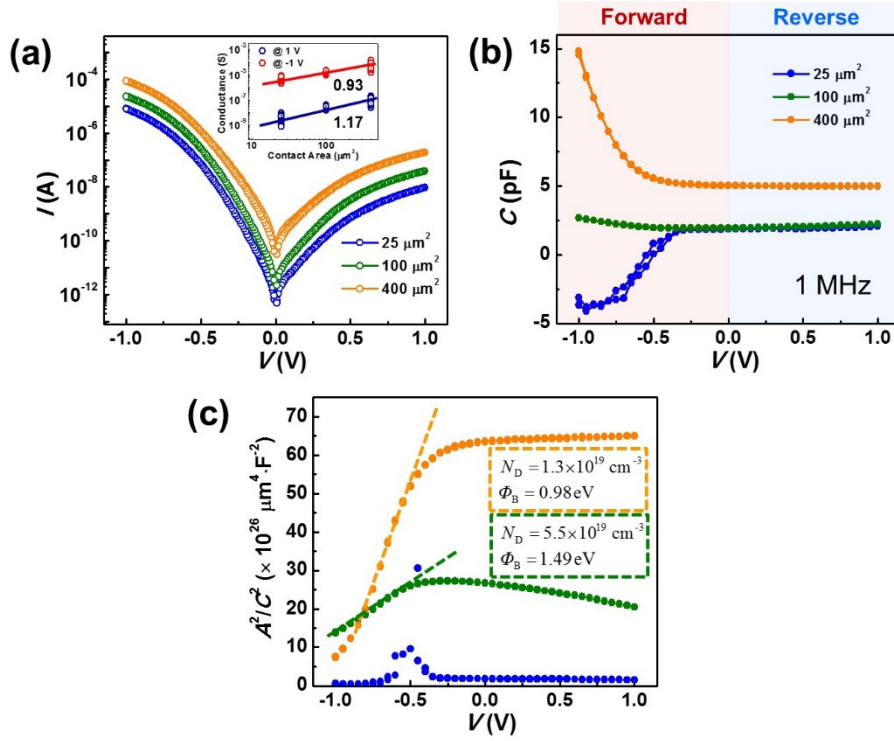


Figure 5.19 (a) I - V and the corresponding (b) C - V characteristics of the as-fabricated devices with regard to contact area (measured at RT and an AC frequency of 1 MHz). The inset in Figure 5.19a shows the contact area dependence of the electrical conductance at ± 1 V. (c) A^2/C^2 - V plots to extract N_D and Φ_B .

In addition to the as-fabricated devices, the I - V and C - V results of the devices after annealing at 300 °C for 1 h and at 400 °C for 1 h are shown in **Figure 5.20**. After annealing, the electrical conductance increases, and it is strongly dependent on the Schottky contact area. However, the obtained C values of the 25- and 100- μm^2 devices are negligibly affected by the contact area or the applied bias. Although the C in 400 μm^2 devices increases as a forward bias is applied, the shapes of the A^2/C^2 - V curves are non-linear. Convex regions are even observed for the devices annealed at 300 °C for 1 h. Non-linear A^2/C^2 - V curves imply that the interface states at the TE/a-IGZO contact (even in a-IGZO/BE contact) exaggerate the C value^[5.11-5.13]. N_D and Φ_B are extracted from the local linear region of the curves (0 ~ 0.25 V for the devices after annealing at 300 °C for 1 h and -0.4 ~ 0 V for the devices after annealing at 400 °C for 1 h). Both devices show that N_D is approximately around 10^{18} cm^{-3} , which is much larger than the values from the I - V analysis (**Figure 5.11**) and the Φ_B values also deviate from the I - V results. We believe that the extraction of accurate N_D and Φ_B is difficult, although the devices were annealed because parasitic capacitances and poor Ohmic contacts still exist.

Interestingly, the devices after annealing at 300 °C for 1 h show hysteretic C - V curves, whereas the hysteresis was not observed for the devices after annealing at 400 °C for 1 h. The C values of the devices under the increasing voltage sweep direction (-1 → 1 V) are larger than those under the decreasing voltage sweep condition (1 → -1 V). These results support our suggestion in the manuscript that as electron trapping/detrapping occurs at V_{OS} in the electron trap states, hysteretic I - V curves are observed. Under the increasing voltage sweep condition, electron detrapping occurs at the Schottky contact under a negative bias region (i.e., decrease of W_D or Φ_B), resulting in an increase in the electrical conductance of the device. On the other hand, the electrical conductance of the

devices decreases under the decreasing voltage sweep direction because W_D increases (and Φ_B increases) due to electron trapping. The tendency of the decrease/increase of with respect to the voltage sweep direction is consistent with the direction of hysteretic C - V curves. Thus, charge trapping/de-trapping occurs at V_{OS} in the electron trap states upon sweeping the DC or AC voltage, which not only affects the electrical conductance of the devices but also C_{a-IGZO} . Although the exact N_D and Φ_B values could not be obtained from the C - V curves of the devices, evidence of electron trapping/detrapping phenomena at the Schottky contacts could be found in the C - V results. **Figure 5.20c** shows the changes of the C - V characteristics of the devices with respect to the bias frequency. As the bias frequency decreases from 1 MHz to 1 kHz, the measured C value increases. This also suggests the presence of poor Ohmic contacts^[5,12,5,13].

In conclusion, the extraction of N_D (as well as the trap energy level) in a-IGZO by analyzing the C characteristics of the devices that exhibit Schottky conduction is difficult because the C characteristics of the devices are affected not only by the Schottky diodes but also by the parasitic capacitance (e.g., MOS-, MOM capacitors, and $C_{Interface}$) and poor Ohmic contacts. However, the I - V characteristics of the devices are dominated by the Schottky diode component. Therefore, we believe that a precise reverse current analysis of the Schottky conducting devices is the best way to investigate the changes of in a-IGZO due to SR.

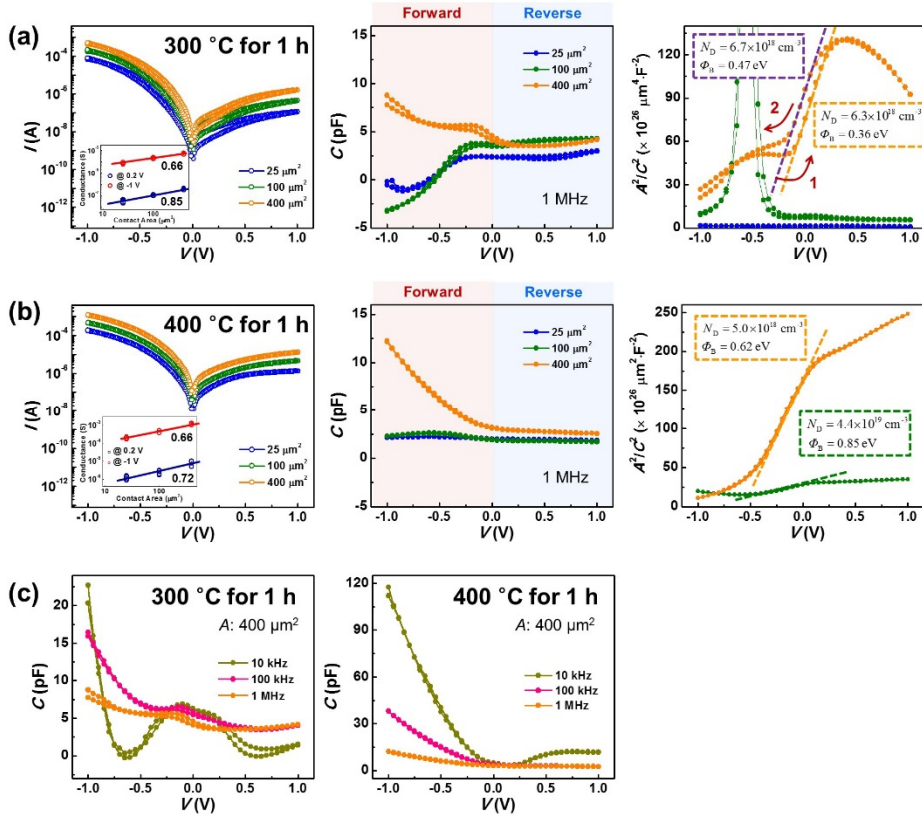


Figure 5.20 I - V , C - V , and A^2/C^2 - V results in the devices after annealing (a) at 300 °C for 1 h and (b) at 400 °C for 1 h. (c) Frequency dependence of C - V characteristics in the devices.

5.6. Effect of H dopant

Oxide semiconductors such as ZnO and a-IGZO contain large amount of unintentional H dopant ($>10^{20} \text{ cm}^{-3}$)^[1,45,1,51]. Some authors suggest that major electron donor in oxide semiconductors is H, not V_O ^[5,14]. Moreover, PECVD-SiO₂ films, which are used to isolation layer on the devices, also have non-negligible H impurities^[5,15]. Influence of H dopant on the experimental results of SR-driven intrinsic doping effect are considered as follows.

1) In **Section 4**, when Ta-Al layer is not covered with a W electrode, electrical conductance of the devices is higher than that of the devices without Ta-Al after annealing at 450 °C in vacuum condition (10^{-3} Pa) (**Figure 4. 11**). One remarkable point is that H impurities easily diffuse out from a-IGZO even annealing temperature of 200 °C^[1,27,2,10]. It means that the H concentration in a-IGZO thin-film patches in devices without a Ta-Al layer would decrease during annealing under vacuum ambient. If H impurities significantly affect the electrical properties of a-IGZO, the electrical conductance of the devices without the Ta-Al layer will decrease after annealing. However, the electrical conductance of the devices without Ta-Al increased, even more than that for the devices with a Ta-Al bilayer. These results suggest that when Ta-Al layer is absent, V_{OS} are generated in a-IGZO during annealing, results in higher electrical conductance than that of the devices with Ta-Al. Moreover, the effects of H impurities on the electrical properties of a-IGZO are negligible compared with the V_{OS} .

2) If H doping in the a-IGZO thin-film patches in the devices occurs from the CVD-SiO₂ layer driven by diffusion and affects the electrical properties of the a-IGZO, the changes in the electrical properties of the devices show an annealing time-dependent behavior because diffusion is a time-dependent process^[1.45,1.51]. However, the I - V characteristics of the devices showed a weak annealing time dependence (**Figure 4.11 and 5.11**). These results suggest that the influence of H diffusion from CVD-SiO₂ layers on the electrical properties of a-IGZO is negligible: Annealing time-independent behavior can be another piece of evidence that time-dependent extrinsic reactions (e.g., diffusion of impurities, redox reactions) did not occur during annealing.

3) **Figure 5.21** shows representative I - V characteristics of the devices with respect to O partial pressure during a-IGZO thin-film deposition ($P_{O_2, dep.}$) with same working pressure of chamber. According to the magnitude of $P_{O_2, dep.}$, electrical conductance of the devices are inversely changed. These results also suggest that V_{OS} significantly affect the conductivity of a-IGZO. If most of the H impurities ($>10^{20} \text{ cm}^{-3}$) act as shallow donors, a-IGZO becomes degenerate, and the I - V curves of the devices could show Ohmic behavior. However, dominant conduction mechanism of the as-fabricated devices is Schottky thermionic emission. H dopants may be compensated for by excess O (i.e., weakly bonded O) in a-IGZO^[1.45,1.51].

In summary, H dopants did not significantly affect the electrical properties of a-IGZO and that V_{OS} are the dominant doping impurities.

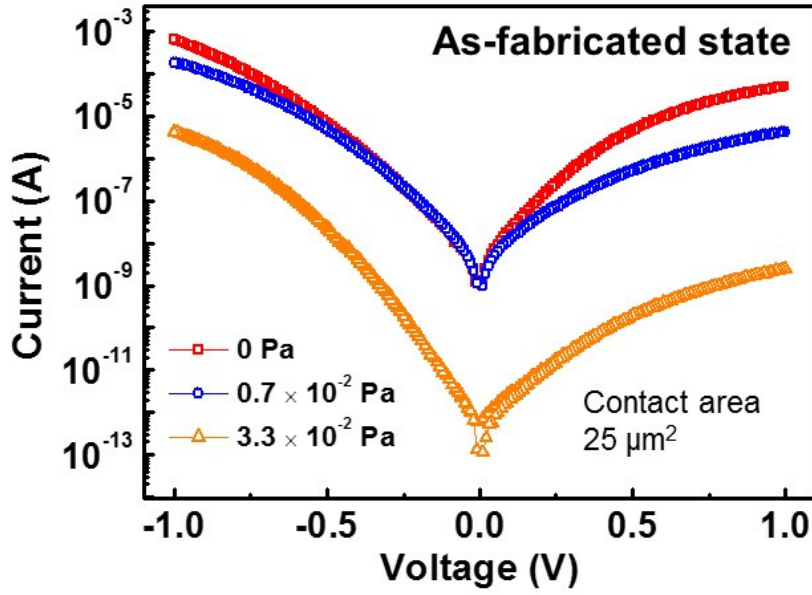


Figure 5.21 Representative I - V curves of the devices in the as-fabricated state with respect to the O partial pressure during a-IGZO thin-film deposition. Base pressure (10^{-5} Pa) and working pressure (0.5 Pa) conditions were same.

5.7. Summary

In summary, SR-driven increase in V_{OS} in the shallow-donor state in a-IGZO is demonstrated. From the measurement of the changes in electrical conductance and analyses of the conduction mechanism in the devices, we verified that SR drove the changes in the electronic state of V_{OS} from the deep-donor or electron-trap states to the shallow-donor state, and the energy level of the V_{OS} in the shallow-donor state was estimated to be approximately 0.1 eV. As the annealing temperature increased from 300 °C to 450 °C, N_{DS} in a-IGZO increases from $\sim 10^{16} \text{ cm}^{-3}$ to $\sim 10^{19} \text{ cm}^{-3}$ (from $< 10^{16} \text{ cm}^{-3}$ to $\sim 10^{18} \text{ cm}^{-3}$ for n_e , respectively). These results suggest a smaller size of free volume defects in a-IGZO exposed to higher annealing temperatures, as well as, more V_{OS} in the dense network and consequently higher N_{DS} values. The activation energy of N_{DS} formation (approximately 1.76 eV) can be attributed to the ionic bonding of a-IGZO. The SR-driven doping may offer new possibilities for controlling n_e in amorphous oxide semiconductors in addition to redox control. The strong dependence of SR-driven doping on the annealing temperature, rather than the annealing time, will play a critical role in achieving reliable thermal stress resistance in electronic devices. In future work, we hope to investigate the effects of the initial V_O concentrations (i.e., the degree of oxygen non-stoichiometry) on the SR-driven concentration increases in V_{OS} in the shallow-donor states.

CHAPTER 6

Dynamical Changes in Cu Doping Effect

6.1. Introduction

Cu has been considered as one of the most important material for development *p*-type oxide semiconductors. However, *p*-type characteristics of Cu dopant are solely observed at crystalline oxides, not amorphous phase (**Section 1.2.3**). To unravel the exact electronic states of Cu in amorphous oxide semiconductors (AOSs), veiled doping mechanism of Cu in AOSs should be disclosed. In this study, we report diffusion behavior of Cu in AOSs and effect of Cu dopant on electrical properties of AOSs with respect to the thermal annealing conditions. Moreover, we suggest that Cu doping control is an effective methodology to generate and to tune the resistive switching (i.e., reversible electrical breakdown) characteristics in AOSs.

6.2. Experiments

Devices used in this section have same basic structure of the devices in **Section 4**. Although a-IGZO deposition conditions are same for the **Section 5**, a-IGZO film thickness is reduced from 160-nm to 40-nm to observed Cu doping effect more clearly. **Figure 6.1** depicts the vertical structured Cu/a-IGZO/W devices (the Cu devices). Cu diffusion into a-IGZO occurs from Cu top electrode (TE) and diffused Cu accumulate in the bulk of a-IGZO because both SiN_x isolation layer and W bottom electrode (BE) act as Cu diffusion barrier^[6,1,6,2]. In **section 5**, doping concentration (N_D) as well as free electron concentration (n_e) in a-IGZO thin-film patches in the W/a-IGZO/W devices (the W devices) increases after annealing due to structural relaxation (SR). As the changes in electrical properties of the Cu devices were compared with that of the W devices, Cu doping effect and SR-driven doping effect on the electrical properties of a-IGZO could be separated. The devices were annealed at temperatures between 300 and 500 °C for up to 100 h under vacuum (10^{-3} Pa) condition. Further details of annealing conditions are consulted in **Section 3.3**. After annealing, the I - V characteristics of the devices were measured with respect to the substrate temperature (**Section 3.4**). At each annealing condition, 10-30 devices were considered to evaluate the changes in the electrical properties of a-IGZO.

The changes of density of states (DOS) in a-IGZO with respect to site location of Cu dopants were calculated based on the first-principles calculation using the VIENNA ab-initio simulation package (VASP) as note in **Section 3.6**. Moreover, the changes in compositional and chemical characteristics of a-IGZO due to Cu diffusion using transmission electron microscopy (TEM), secondary ion mass spectroscopy (SIMS), and X-ray photoelectron spectroscopy (XPS) as noted in **Section 3.5**.

6.3. I - V Characteristics changes

Figure 6.2 shows the semi-logarithmic I - V curves of the devices (contact area of $25 \mu\text{m}^2$) in the as-fabricated state measured at room temperature (RT). Voltage was applied to the TE, whereas the BE was grounded. Initially, both devices show asymmetric I - V curves and electrical conductance (G) of the W devices is higher than the Cu devices. Rectifying behavior indicates that electrical conduction of the devices is not limited by the bulk resistance of a-IGZO, but strongly affected by the Schottky barrier at metal/a-IGZO interface (i.e., electrode-limited conduction)^[2,16]. As the G at negative bias is higher than that under positive bias, Schottky barrier height (Φ_B) at the a-IGZO/BE interface is higher than that at the a-IGZO/TE interface. Ideally, difference in Φ_B between both interfaces is negligible because the W devices are symmetric structure and the work function difference between W (4.55 eV) and Cu (4.65 eV) is small for the Cu devices^[4,13]. These phenomena would be induced by interface states at TE interface which were generated during TE deposition process, results in Φ_B decrease at TE/a-IGZO interface[□]. As initial free electron concentration (n_e) in a-IGZO thin-film patches in the devices is below 10^{16} cm^{-3} , dominant conduction mechanism of the devices is Schottky thermionic emission^[2,17,5,8]. Φ_B and ideality factor (n) values of the W devices are similar with the Cu devices, whereas series resistance (R_S) is smaller. R_S is the summation of contact resistance (R_C) at TE/a-IGZO interface and the bulk resistance of the undepleted region in the a-IGZO thin-film patches (R_{Bulk})^[2,16]. As a-IGZO thickness is too thin compared to the ideal length of depletion region at Schottky contact^[5,8], R_S is significantly affected by R_C rather than R_{Bulk} . These results imply that lower G of the W devices than that of the Cu devices is induced by higher R_C values in the Cu devices than that in the W devices, whereas a-IGZO/BE interface properties are

same for the both devices.

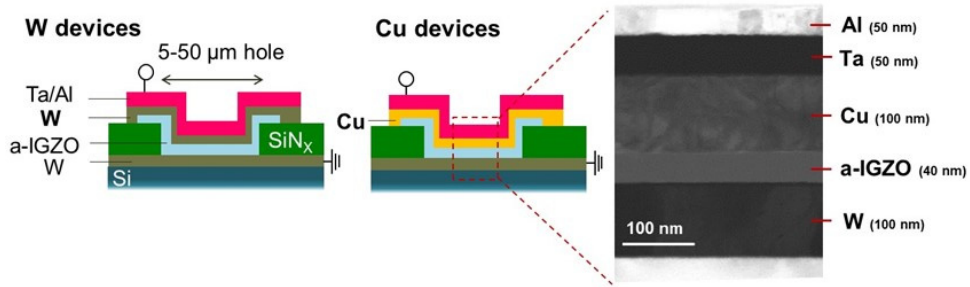


Figure 6.1 Schematic structure of the W devices and the Cu devices composed of 40-nm-thick a-IGZO thin-film patches. A cross-sectional TEM image of the Cu devices in the as-fabricated state is shown as well.

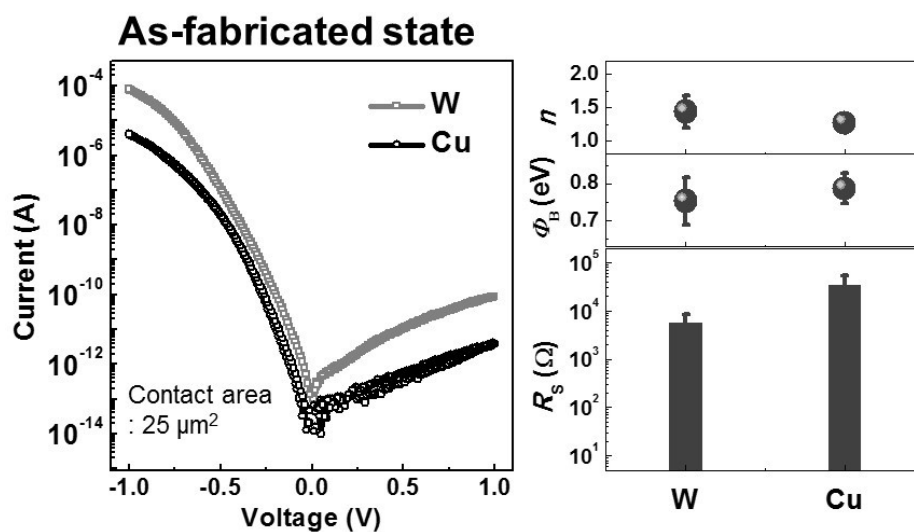


Figure 6.2 The representative I - V characteristics in the as-fabricated devices (measured at RT). Both devices show rectifying I - V behaviors.

Figure 6.3 presents a map of the I - V curves of the devices with respect to the post-fabrication annealing conditions, in which the temperature was varied from 300 to 500 °C for 1 to 100 h at maximum. G of the devices at ± 1 V is presented in **Figure 6.4**. After annealing at 300 °C for 1 h, both devices show increase of G compared with that in the as-fabricated state. Rectifying characteristics are maintained even after annealing time of 100 h. Remarkable fact is that G of the Cu devices increases with increasing annealing time, whereas that of the W devices is nearly unchanged. As annealing temperature increases to 400 °C for 1 h, G of the W and the Cu devices more increases. The W devices show weak annealing time dependence of G with maintenance of rectifying behavior even after annealing time of 25 h. For the Cu devices, the G is comparable (or slightly higher) to that of the W devices until the annealing time of 9 h. Interestingly, the G of the Cu devices decreases drastically after annealing for 16 h and I - V curves become symmetric. Moreover, deviations of G among each device become significantly wider; thus, G of the Cu devices become weakly dependent on the contact area. After annealing at 500 °C, G of the Cu devices more decreases even after annealing time of 1 h with wide deviation of G , whereas G of the W devices increases more and the I - V curves become symmetric. In **section 5**, the origin of annealing temperature-dependent increase of G of the W devices is SR-driven electron doping effect^[5,8]. As annealing temperature increases, N_D increases (i.e., increase of n_e) with thickness reduction of a-IGZO thin-film patches due to SR, without any observations of chemical reactions, crystallization, dependency of ambient conditions. A plausible origin of these phenomena is that V_{OS} in the deep donor or electron traps consequently transformed into V_{OS} in the shallow-donor state^[1,22,1.23]. Through I - V characteristics of the Cu devices are compared with that of the W devices, dominant electronic state of Cu dopant in a-IGZO can be determined as follows. i) At 300 °C, Cu dopant increases electrical conductivity

Chapter 6: Dynamical Changes in Cu Doping Effect

of a-IGZO which is proportional to diffusion time. ii) At 400 °C, dominant electronic state of Cu dopant in a-IGZO is altered with respect to annealing time. iii) At 500 °C, Cu dopant decreases electrical conductivity of a-IGZO even after annealing time of 1 h. In order to analyze the Cu doping effect in detail, conduction mechanism changes in the devices were analyzed as shown in **Section 6.4**.

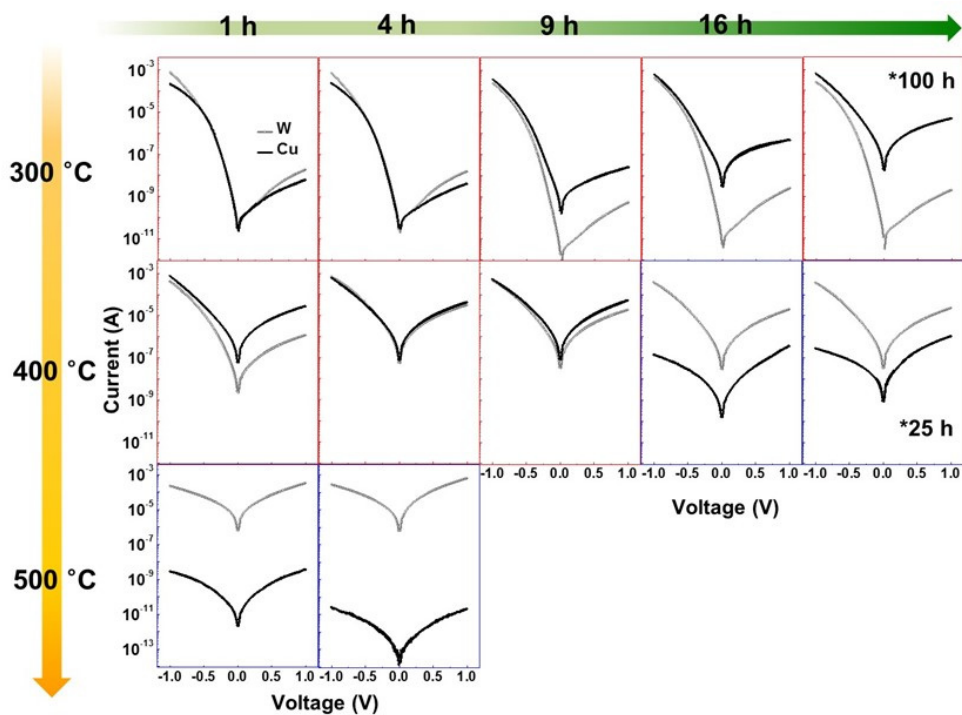


Figure 6.3 I - V map of the devices considering the both annealing temperature from 300 to 500 °C and the annealing time from 1 to 100 h. Contact area of the devices is 25 μm^2 .

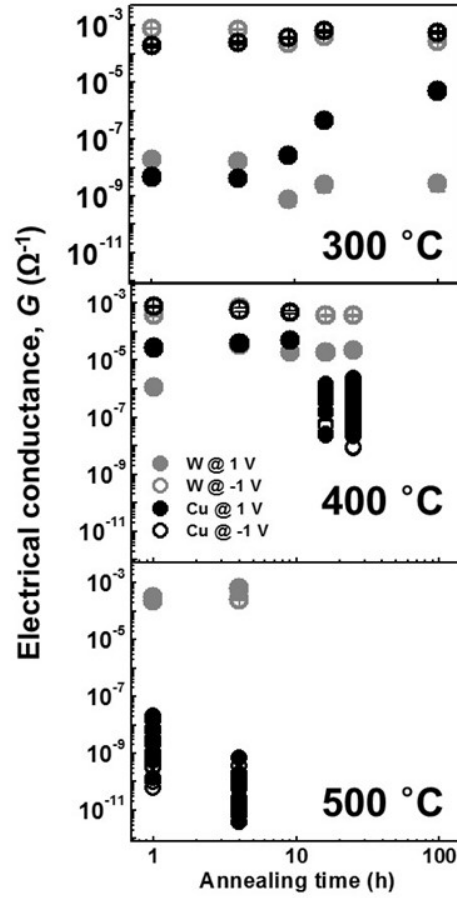


Figure 6.4 Electrical conductance (G) of the devices. I - V characteristics as well as G of the W devices is strongly affected by annealing temperature, but not on the annealing time. However, I - V characteristics and G of the Cu devices is altered by annealing time as well as annealing temperature.

6.4. Conduction mechanism analysis

Figure 6.5 presents the variations in Φ_B and n with regard to annealing conditions. After annealing at 300 °C, the values of Φ_B and n of the W devices are similar with the Cu devices until annealing time of 4 h. However, with more annealing time, Φ_B decreases and n increases for the Cu devices, whereas the W devices showed nearly constant values. Decrease of Φ_B with increasing n implies that N_D increases^[2,17]. N_D can be quantified through analyzing the reverse leakage current^[5,8], and the extracted values of N_D were shown in top in **Figure 6.5**. As annealing time increases from 1 to 100 h, N_D in the Cu devices increases from $\sim 10^{16}$ to $\sim 10^{17} \text{ cm}^{-3}$, whereas N_D in the W devices are nearly constant ($\sim 10^{16} \text{ cm}^{-3}$). These results strongly suggest that Cu dopant act as an electron donor under diffusion condition of 300 °C. N_D in the Cu devices significantly increases compared to that in the W devices between annealing time of 4 and 9 h. It implies that Cu dopant arrives at a-IGZO/BE interfaces within annealing time of 9 h (i.e., Cu diffusion length of 40 nm). Therefore, Cu diffusivity in a-IGZO is expected as $\sim 10^{15} \text{ cm}^2\text{s}^{-1}$ at 300 °C based on the equation of $L = \sqrt{D_{\text{Cu}} t}$ ^[1,41], and the estimated value is similar to the Cu diffusivity in several amorphous oxides^[1].

After annealing at 400 °C, N_D in the Cu devices increases to 10^{17} cm^{-3} even after annealing time of 1 h and the values are nearly unchanged up to 9 h. Cu diffusivity at 400 °C is also expected as $\sim 10^{14} \text{ cm}^2\text{s}^{-1}$ and activation energy can be roughly estimated as 0.9~1.2 eV. Although delicate estimation is more needed, estimated values are similar to the Cu diffusivity in SiO_2 ^[1,70,1,71]. N_D in the Cu devices after annealing at 400 °C is similar to that in the annealed Cu devices at 300 °C for 100 h. These results indicate that solubility limit of donor-state Cu in a-IGZO is $\sim 10^{17} \text{ cm}^{-3}$ at RT. Under annealing at 400 °C, Cu diffuses into a-IGZO enough to saturate solubility limit of donor-state Cu at

RT within annealing time of 1 h, while annealing time of over 100 h is needed at 300 °C. N_D in the W devices also increases to $\sim 10^{17} \text{ cm}^{-3}$ after annealing time of 4 h due to SR-driven doping effect and N_D values are nearly constant up to 25 h. However, N_D in the Cu devices after annealing time of 16 h could not be measured by thermionic emission theory, because I - V curves does not show rectifying behavior.

After annealing at 500 °C, both the W and the Cu devices show symmetric I - V curves. However, G of the W devices further increases whereas that of the Cu devices further decreases. In the previous report, alternation of I - V shapes of the W devices from asymmetric to symmetric indicate that dominant conduction mechanism is changed from thermionic emission to Pool-Frenkel (P-F) conduction (i.e., bulk-limited conduction) due to SR-driven doping effect^[5,8]. However, I - V characteristics of the Cu devices were not fitted well by the orthodox P-F conduction theory (**Figure 6.6 and 6.7a**). Tunneling-based conduction is not also dominant conduction mechanism, because G of the Cu devices show is dependent on substrate temperature (**Figure 6.7b**). Therefore, complex bulk-limited conduction mechanism is existed in the Cu devices that exhibit symmetric I - V curves. These results unprecedentedly report that dominant electronic state of Cu dopant in a-IGZO is not solely an electron donor, and Cu dopant also can decrease electrical conductivity of a-IGZO which is determined by annealing temperature as well as annealing time. Moreover, diffusivity of donor-state Cu in a-IGZO is roughly deducted which value is similar to the Cu in SiO₂. In addition to changes in electrical conduction properties of the devices, electrical breakdown characteristics with respect to Cu doping conditions were investigated shown below.

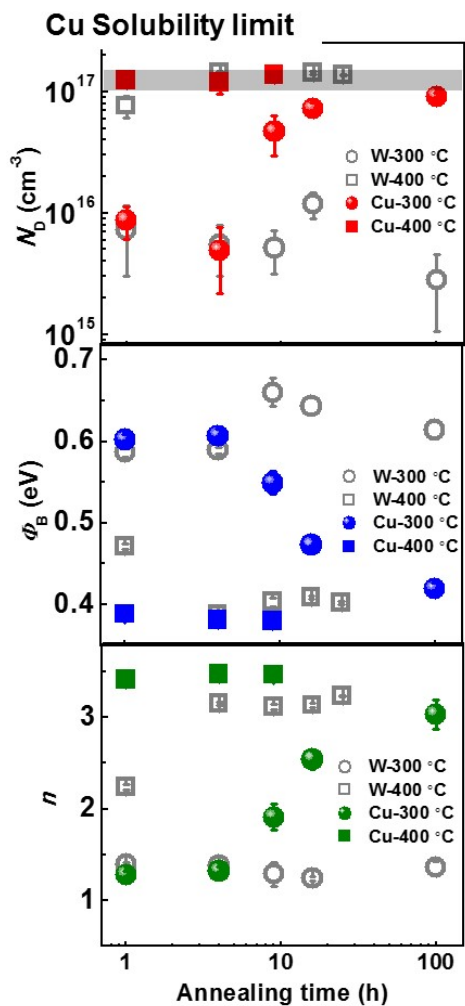


Figure 6.5 The variations of Φ_B , n , and N_D in the Schottky conducting devices with respect to annealing conditions.

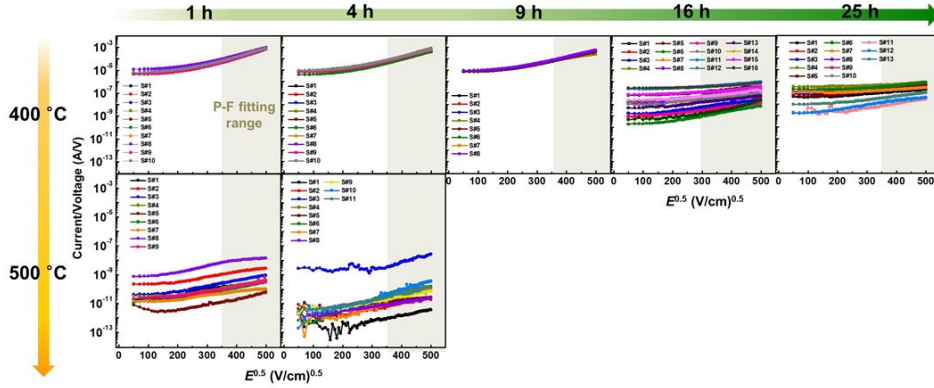


Figure 6.6 $\text{Log}(I/V)-E^{0.5}$ plots of the Cu devices after annealing at 400-500 °C to identify the P-F conduction.

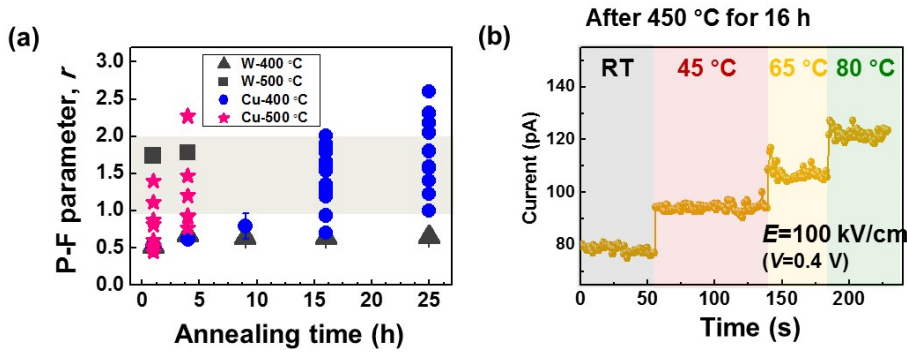


Figure 6.7 (a) P-F fitting results; P-F parameter, r . (b) Substrate temperature dependence of electrical conductance of the Cu devices after annealing at 450 °C for 16 h at $E=100$ kV/cm.

6.5. Electrical breakdown behavior

6.5.1. The origin of resistive switching

Figure 6.8 presents the typical electrical breakdown characteristics of the Cu devices after annealing at 300 °C. Firstly, positive voltage is swept on the Cu devices until the value of current reaches to 1 mA (i.e., compliance current, I_{CC}). It is called electroforming process^[6.3]. In the as-fabricated state, the current drastically increases under the voltage of around 7 V. When voltage with the same polarity side is swept again without limit to I_{CC} , the Cu devices show hard breakdown (HDBR) behavior; irreversible increase of G . After annealing time of 9 h, HDBR still occur at the Cu devices. However, when annealing time is exceeded to 16 h, the Cu devices show RS behavior. According to applied bias history, Low resistance state (LRS) of the Cu devices is reversibly changed to the high resistance state (HRS), SET \leftrightarrow RESET. In contrast to the Cu devices, the W devices only show HDBR behavior regardless of annealing time (**Figure 6.9a**). These results suggest that donor-state Cu dopants are the origin of RS behavior in the Cu devices. Unipolar RS mechanism (i.e., occurrence of RS at the same bias polarity) have been proposed that formation and rupture of conductive filaments (CF) which are composed of mobile ions in metal oxides^[6.3,6.4]. Thus, Cu ions in a-IGZO drift toward the BE when the electric field is applied (i.e., electrochemical migration) and contribute to form CF which interconnect TE and BE. The value of breakdown voltage in the Cu devices decreases as annealing time increases, whereas the values in the W devices are relatively constant (**Figure 6.11a**). These results imply that CF easily form in a-IGZO as Cu doping concentration increases.

Figure 6.9b presents the contact area dependence of resistance of the Cu devices after annealing time of 100 h. In addition to $25 \mu\text{m}^2$ devices, $4\text{-}2500 \mu\text{m}^2$ devices also show RS behavior. The value of resistance at LRS is independent on contact area, while the resistance at HRS as well as pristine state decreases as contact area increases.

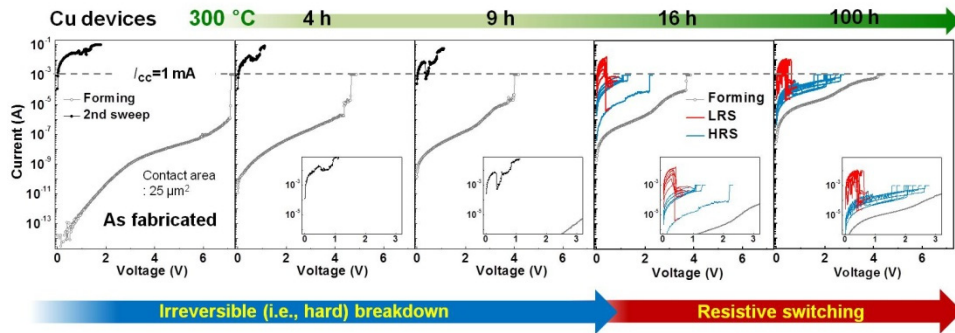


Figure 6.8 Electrical breakdown characteristics. The Cu devices showed hard breakdown in the as-fabricated state and after annealing at $300 \text{ }^{\circ}\text{C}$ for up to 9 h. However, RS behavior is observed after annealing time of 16 h.

These results support that RS occurs at localized region, not homogeneous RS^[2,33,2.35,6.5]. At HRS, the resistance of the Cu devices is predominated by bulk resistance of a-IGZO that corresponds to the ruptured region of CF, results in contact area dependent-resistance^[2.35,6.5]. **Figure 6.9c** shows the temperature dependence of resistance of the Cu devices and the W devices after breakdown at I_{CC} of 1 mA. The resistance value of the Cu devices at LRS linearly increases with increasing temperature, whereas that of the W devices after breakdown decreases. Thus, resistance of the Cu devices at LRS exhibits metallic characteristics, whereas conductive paths in the W devices have semiconducting characteristics^[2.35,6.5]. These results suggest that Cu is main component of metallic CF in the Cu devices, whereas conductive paths in the W devices are composed of V_{OS} , which exhibit semiconducting CF^[6.5,2.35]. Temperature coefficient of resistance (TCR) at LRS yields to $0.6 \times 10^{-3} \text{ K}^{-1}$, based on the equation ($R(T) = R_0[1 + \alpha(T - T_0)]$), where R_0 is the resistance at temperature T_0 , 273 K and α is the TCR^[2.25,6.6]. The extracted value is lower than the value of the pure Cu nanowire ($\alpha = 2.5 \times 10^{-3} \text{ K}^{-1}$)^[6.6]. It indicates that weak metallic CF are formed in a-IGZO which combined Cu with other defects, such as V_{OS} ^[2.25]. Since Cu ions are mobile, the Cu in a-IGZO would be located at the free volume rather than at the substitutional sites^[1.41,1.67]. Moreover, when Cu is located at the free volume, Cu would act as an electron donor ($\text{Cu} \rightarrow \text{Cu}^+ + e^-$) similar to the interstitial Cu in crystalline semiconductors^[1.66,1.67]. It is supported by computational simulation results of the changes in total and partial DOS in a-IGZO after Cu doping as shown in **Figures 6.9d and 6.10**. Without Cu doping, Fermi energy level (E_F) is located at valence band maximum (VBM) for stoichiometric a-IGZO (**Figure 6.9d**). When Cu located at the free volume is added, E_F shifts to above conduction band minimum (CBM). However, when Cu substitute In, Ga, or Zn, E_F is nearly unchanged (**Figure 6.10**).

Therefore, I - V characteristics changes and electrical breakdown behavior in the annealed Cu devices at 300 °C with computation results of DOS changes strongly suggest that diffused Cu is dominantly located at free volume in a-IGZO and it acts as mobile electron donor. It should be noted that when annealing time is shorter than 9 h, the Cu devices show HDBR likewise the W devices. This means that the Cu doping concentration and the distribution in a-IGZO in the corresponding annealing time is not enough to form stable CF during the voltage sweep at RT. Therefore, Cu doping conditions determine generation of RS and also may alter RS characteristics in a-IGZO. Alternation of RS characteristics with respect to Cu doping conditions was further investigated show below.

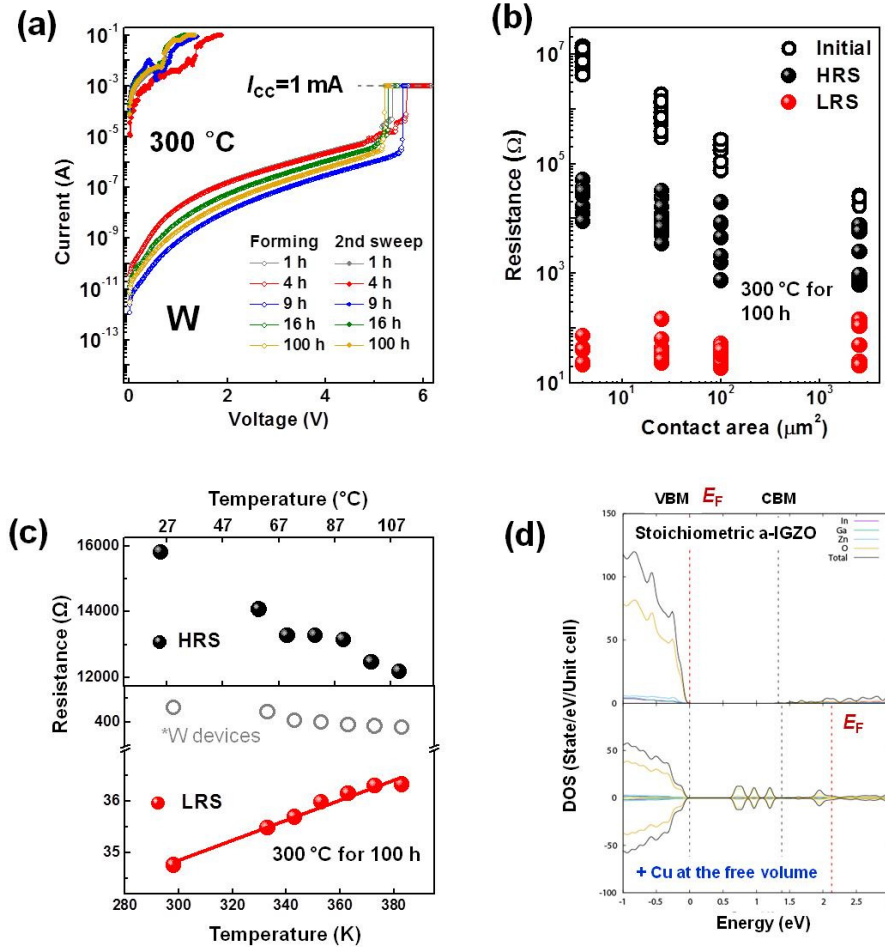


Figure 6.9 (a) Electrical breakdown characteristics of the W devices after annealing at 300 °C. (b) Contact area and (c) temperature dependence of resistance of the Cu devices after annealing at 300 °C for 100 h. The resistance values of the electrically-broken W devices with respect to substrate temperature are also included. (d) The DOS changes in stoichiometric a-IGZO due to Cu inclusion at the free volume.

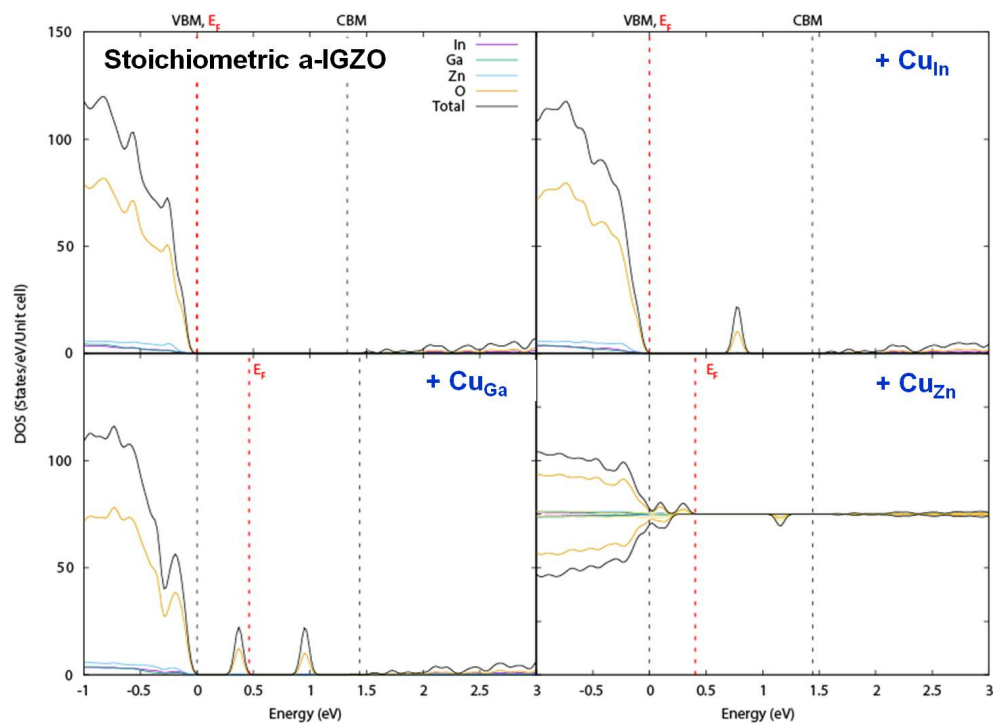


Figure 6.10 The DOS changes in stoichiometric a-IGZO due to Cu inclusion at the substitutional sites (i.e., In, Ga, or Zn).

6.5.2. Resistive switching characteristics

Figure 6.12 shows RS characteristics of the Cu devices (contact area of $4 \mu\text{m}^2$) after annealing at 400°C for 1 h and 16 h with respect to operating bias polarity. In addition to unipolar bias condition, negative unipolar bias, and bipolar bias (i.e., SET under positive bias, whereas RESET under negative bias) conditions were applied to operate RS in the Cu devices. Moreover, The cumulative distributions of RS performance (RESET power, resistance, and voltage) of the Cu devices were expressed as shown in **Figure 6.13** following the method described in the JEDEC standard JESD 37. At annealing condition of 400°C , annealing time of 1 h is enough to generate unipolar RS in the Cu devices (**top in Figure 6.12**), whereas the W devices occur HDBR regardless of annealing time (**Figure 6.11b**). These results are consistent with that donor-state Cu at the free volume is saturated at a-IGZO thin-films within annealing time of 1 h at 400°C . It is noted that G value is 5 mA, because Schottky reverse G of both the Cu and the W devices is too high to break down under I_{CC} of 1 mA. Remarkable point is that breakdown voltage or forming voltage (V_{FORM}) is more reduced than that of V_{FORM} in the annealed Cu devices at 300°C (**Figure 6.11a**). CF formation is affected by not only metal ion mobility but also redox rate of metal ions^[2,39]. Thus, larger Schottky reverse G may assist reduction of Cu ions and consequently CF is formed at lower voltage. After annealing time of 16 h, unipolar RS occurs at the Cu devices. It implies that although dominant electric role of Cu dopant is reduction in electrical conductivity of a-IGZO, donor-state Cu still exists in a-IGZO enough to generate RS. Low G would decrease the rate of CF formation, resulting in increase of V_{FORM} (**Figure 6.11a**). Compared to the annealed devices at 400°C for 1 h, mean resistance value (50% of cumulative probability) at HRS is higher, while the value of LRS is similar; LRS/HRS ratio

increases (**top in Figure 6.13**). However, switching uniformity of resistance as well as voltage get worse. RESET power consumption also increases. These results suggest that Cu-related defects which decrease electrical conductivity of a-IGZO deteriorate unipolar RS performance.

When negative bias applied during forming process, the annealed Cu devices at 400 °C for 1 h show HDBR (**middle in Figure 6.12**). This would be induced that contribution of Cu dopant on CF formation is reduced because Cu ions in a-IGZO drift to Cu electrode (i.e., backward Cu migration) and Cu ions from Cu TE are electrochemically suppressed^[2,29,2,35,2,39]. However, the annealed Cu devices at 400 °C for 16 h show unipolar RS behavior under negative bias conditions. Moreover, uniformity of resistivity at HRS is enhanced and RESET power consumption is reduced compared to unipolar RS characteristics (**middle in Figure 6.13**). Interesting point is that negative differential resistance (NDR) behavior is newly observed during SET process. The origin of voltage-controlled NDR (N-shape) is suggested that space charge region in active materials^[2,16,2,45,2,46,2,47]. During application of voltage, distribution or charge density in space charge region is altered due to charge trapping/detrapping and results in changes of resistance of active materials. Thus, these findings strongly suggest that Cu-related defects form space charge region in the bulk of a-IGZO and decrease electrical conductivity of a-IGZO. Moreover, Cu-related defects occur NDR-based RS, when CF formation composed of Cu mobile donor is suppressed by negative bias application.

In addition to unipolar bias condition, the Cu devices exhibit bipolar RS with enhanced RS endurance (**bottom in Figures 6.12 and 6.13**). When positive bias is applied during RESET, CF are partially destroyed Joule heating^[2,29,6,3]. Moreover, additional Cu migration into active materials concurrently occurs by electrochemical dissolution of Cu TE. Thus, continuous supply of Cu ions into a-IGZO thin-films causes

excess concentration of donor-state Cu and may deteriorate RS endurance. However, when negative bias is applied for RESET, electrochemical oxidation occurs at CF and assists CF rupture induced by Joule heating^[2,29,6,3]. Backward Cu migration also occurs during RESET process and may keep up concentration of donor-state Cu: It would be dominant origin of improvement of RS endurance. The annealed Cu devices at 400 °C for 16 h still show poorer switching uniformity and RESET power consumption compared to the Cu devices at 400 °C for 1 h. Interestingly, some of SET processes in the annealed Cu devices at 400 °C for 16 h show NDR behavior. Thus, CF formation and NDR concurrently occurs and causes poorer uniformity of RS.

Currently reported RS performance of the Cu devices is still poor for the commercialization as a RS devices and the more elaborated estimation of the RS performance (e.g., retention, pulse switching mode) is required^[2,29,6,3]. However, we believe that RS performance of a-IGZO could be enhanced through optimization of Cu doping conditions into a-IGZO: Further studies will be performed.

Remarkable points in this study are that Cu doping enables a-IGZO to have two-type RS characteristics according to the dominant electronic states. Moreover, dominant electronic states of Cu dopant in a-IGZO is changed according to annealing conditions. After annealing at 300 °C, mobile Cu donor is dominant even after annealing time of 100 h. However, Cu-related defects that form space charge region in a-IGZO are dominant after annealing at 500 °C for 1 h. At annealing temperature of 400 °C, dominant electric role of Cu dopants is altered according to annealing time. In-depth discussion about the origin of alternation of dominant electronic states of Cu dopant in a-IGZO based on microscopic observation of Cu distribution in a-IGZO and compositional-chemical analysis are shown below.

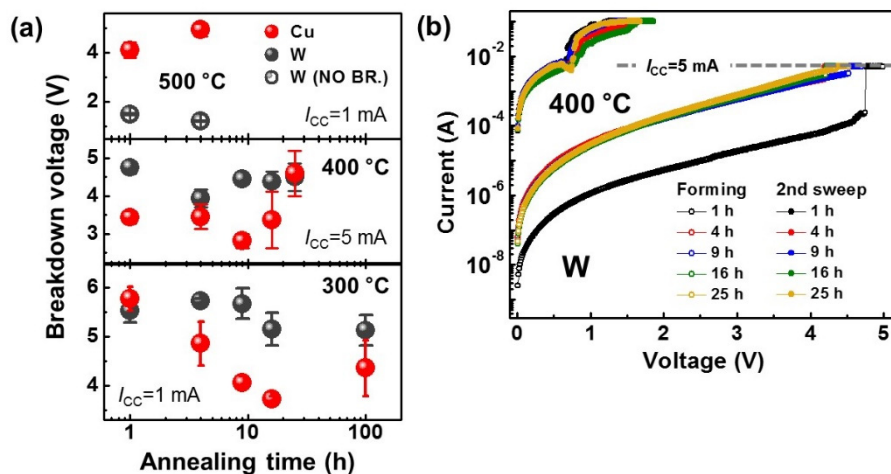


Figure 6.11 (a) Breakdown voltage of the Cu devices and the W devices. (b) Electrical breakdown characteristics of the W devices after annealing at 400 °C

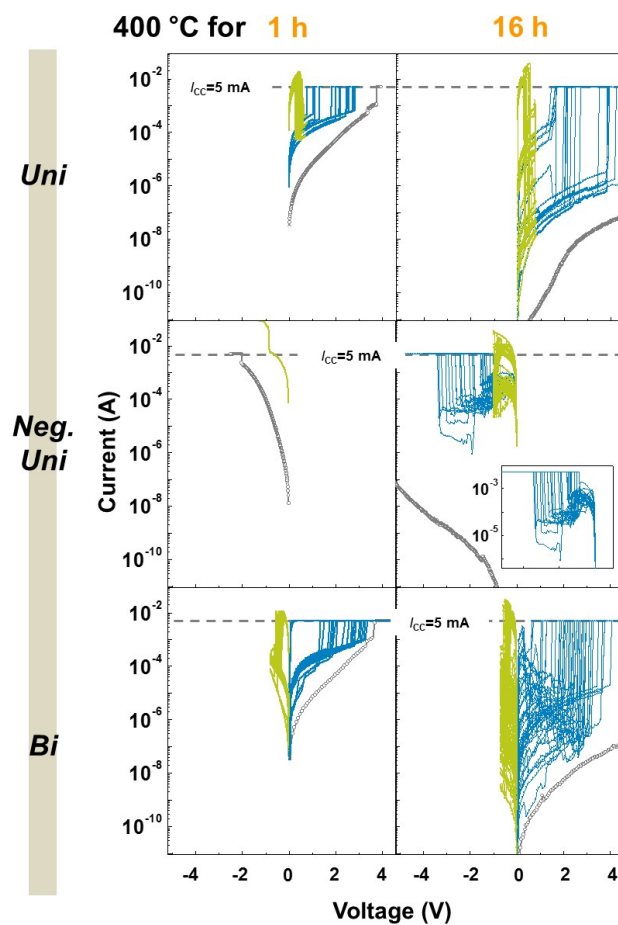


Figure 6.12 Resistive switching characteristics in the Cu devices after annealing at 400 °C for 1 h and 16 h with respect to operating bias polarity.

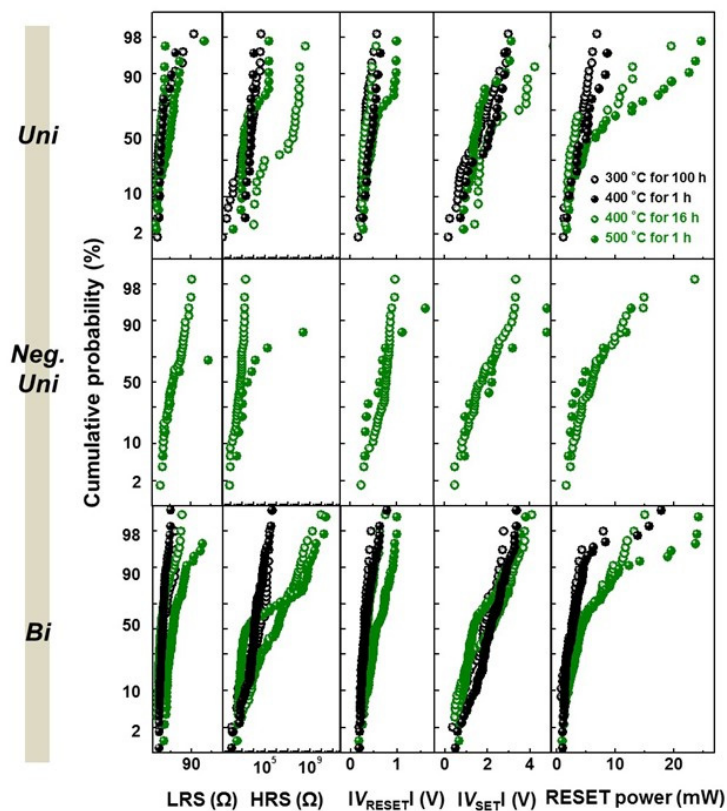


Figure 6.13 Cumulative distributions of the electrical resistance at LRS/HRS, SET/RESET voltage, and RESET power.

6.6. Microstructural and chemical analysis

Figure 6.14 shows the cross-sectional images of the devices measured by high-resolution transmission electron microscopy (HRTEM) and high-angle annular dark-field scanning transmission electron microscopy (HAADF-STEM) with respect to annealing conditions. After annealing at 400 °C for 1 h, a-IGZO is maintained amorphous phase determined by fast Fourier transform (FFT) diffractogram and Cu diffusion is not detected by energy dispersive X-ray spectroscopy (EDS). Although donor-state Cu diffused in a-IGZO as depicted in **Figure 6.17a**, Cu doping concentration is around 10^{17} cm^{-3} (**Figure 6.5**) which is the far below value than detection limits of EDS analysis ($\sim 10\text{-}1 \text{ at}\%$)^[4,5]. Interestingly, as annealing time increases to 16 h, Cu-rich clusters are detected in a-IGZO, which are non-uniformly distributed. As annealing temperature increases to 500 °C, Cu-rich clusters is formed in a-IGZO even after annealing time of 1 h, whereas the W devices show that a-IGZO maintained amorphous phase and interdiffusion does not occurred. Remarkable fact is that some of EDS results show that In concentration is relatively higher at the location of Cu-rich clusters than at a-IGZO bulk, whereas concentration of Ga or Zn is uniform. Identification of exact crystalline phase is difficult, because diffraction peaks indicate that Cu-rich clusters are polycrystalline. However, some diffraction patterns clearly show that Cu-rich clusters are $\text{Cu}_2\text{In}_2\text{O}_5$ or CuInO_2 as shown in **Figure 6.14**. Cu-In-O crystalline clusters, which are non-uniformly distributed, have p-type characteristics^[1,56]. Thus, bulk-heterogeneous *pn* junction is formed at a-IGZO (**Figure 6.17a**). These findings clearly show that microscopic origin of space charge region, which decreases electrical conductivity in a-IGZO and exhibit NDR in a-IGZO, is bulk-heterogenous *pn* junction.

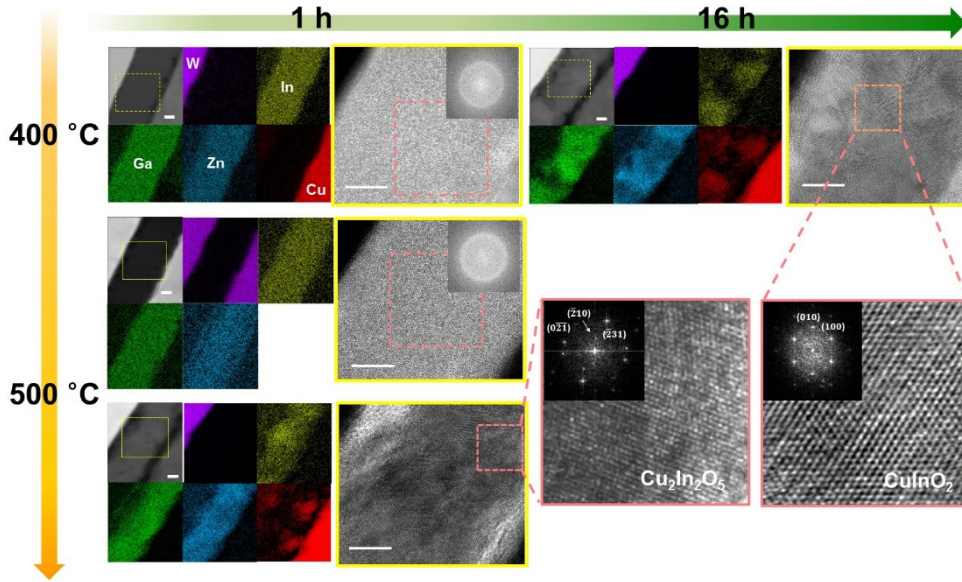


Figure 6.14 HAADF-STEM images, EDS map, HRTEM images, and FFT diffractograms of the devices with respect to annealing conditions. Scale bar, 10 nm. After annealing at 400 °C for 1 h, Cu diffusion were not detected. However, Cu-rich clusters are observed after annealing time of 16 h. As annealing temperature increases to 500 °C, Cu-rich clusters are observed even after annealing time of 1 h, whereas a-IGZO in the W devices maintain amorphous phase without inter-diffusion. Diffraction patterns indicate that Cu-rich clusters are Cu-In-O clusters.

For more delicate analysis of the changes in composition profile, SIMS analysis was conducted on Cu/a-IGZO thin-films as shown in **Figure 6.15**: detection limit of SIMS is $\sim 10^{-3}$ at%^[4,6]. After annealing at 400 °C for 1 h, remarkable changes of compositional profiles is not observed. However, when annealing time is elapsed to 16 h, Cu diffusion in a-IGZO is detected. At the same time, In diffuses into Cu thin-films, whereas composition profiles of Ga, Zn, and O were nearly constant. As annealing temperature increases to 500 °C (for 1 h), the more In diffuses into Cu thin-films as the more Cu diffusion occurs in a-IGZO. Therefore, In provides the most dominant substitutional diffusion site for Cu in a-IGZO.

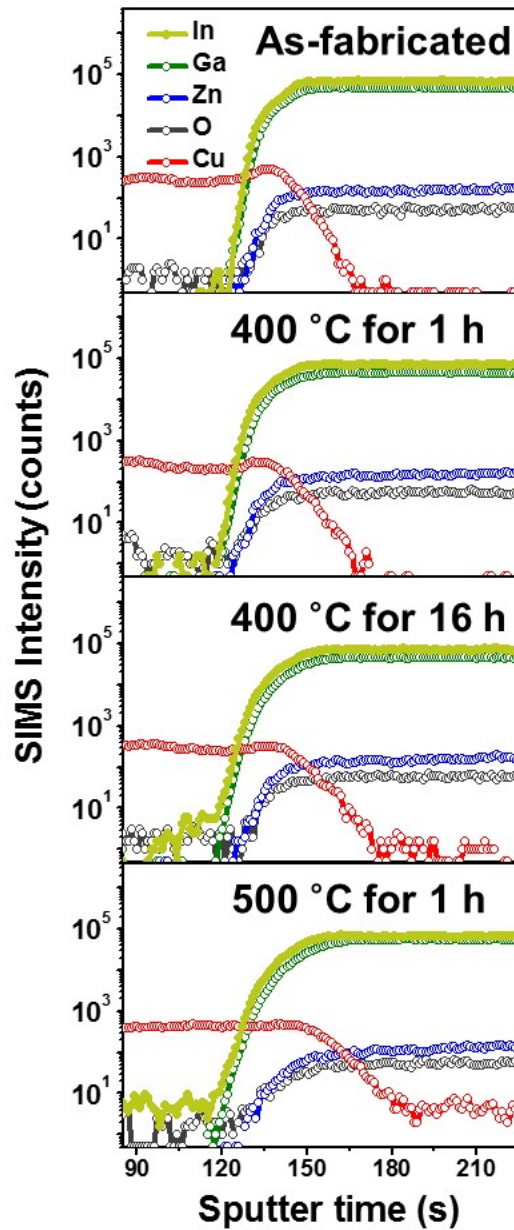


Figure 6.15 SIMS analysis of Cu/a-IGZO interfaces with respect to annealing conditions. Among In, Ga, and Zn, In is dominantly inter-diffused with Cu.

In addition to SIMS, XPS analysis was conducted on multi-layer-thin films which have the same stacks of the Cu devices to measure the changes in chemical state of In, Ga, Zn, and diffused Cu in a-IGZO as well as composition profile changes after annealing as shown in **Figure 6.16**. After annealing at 500 °C for 1 h, interdiffusion between Cu and a-IGZO is also observed (**Figure 6.16a**). Among In, Ga, and Zn, concentration of In significantly decreases. Moreover, XPS spectra of Ga, Zn, and O is nearly unchanged (**Figures 6.16d-6.16f**). However, XPS peaks are newly observed in $3d_{5/2}$ spectra of In in a-IGZO (**Figure 6.16c**). In the as-fabricated state, peak at 444.6 eV which corresponds to In^{3+} (In_2O_3)^[4,7] is solely observed. After annealing, a lower binding energy peak around 443.7 eV is additionally appeared which corresponds to metallic In^[4,7]. These results suggest that Cu diffuses in a-IGZO as substituting In, which in turn generates the metallic In. Metallic In clusters may formed in a-IGZO. **Figure 6.16b** present the Cu $2p_{3/2}$ spectra of diffused Cu in a-IGZO after the annealing. Satellite peak is not observed for Cu in a-IGZO in the range of 940-945 eV, which indicates that Cu^{2+} is negligible in a-IGZO bulk. The position of the main peak for Cu in a-IGZO is nearly same for Cu electrode (932.7 eV)^[4,9], which seems to be contradictory to TEM results because dominant chemical state of Cu in Cu-In-O clusters is Cu^+ ($2p_{3/2}$ peak at 932.5 eV), not metallic Cu^0 . However, remarkable point is that main peak of In, Ga, Zn, and O is positively shifted after the annealing (**Figure 6.16g**). Peak shift of elements has been observed when the surrounding bonding conditions are changed^[6,7,6,8]. Thus, Cu diffusion enough to form Cu-In-O clusters would changes initial bonding nature of a-IGZO. Similarly, XPS spectra of Cu in Cu-In-O clusters as dispersed phase in a-IGZO would be shifted: it is difficult to distinguish Cu^+ from Cu^0 in the dispersed phase due to peak shift as well as similar shapes of Cu^+ and Cu^0 spectra^[6,8]. Therefore, we believe that

Chapter 6: Dynamical Changes in Cu Doping Effect

XPS spectra support that the dominant chemical state of Cu in a-IGZO is expected to Cu^+ in Cu-In-O clusters.

In is the core element to form conduction band minimum (i.e., electron conduction path)^[1,6,1.24,4.2]. Therefore, decrease of In concentration in a-IGZO due to substitutional Cu also causes the reduction in electrical conductivity of a-IGZO in addition to bulk heterogeneous *pn* junction formation.

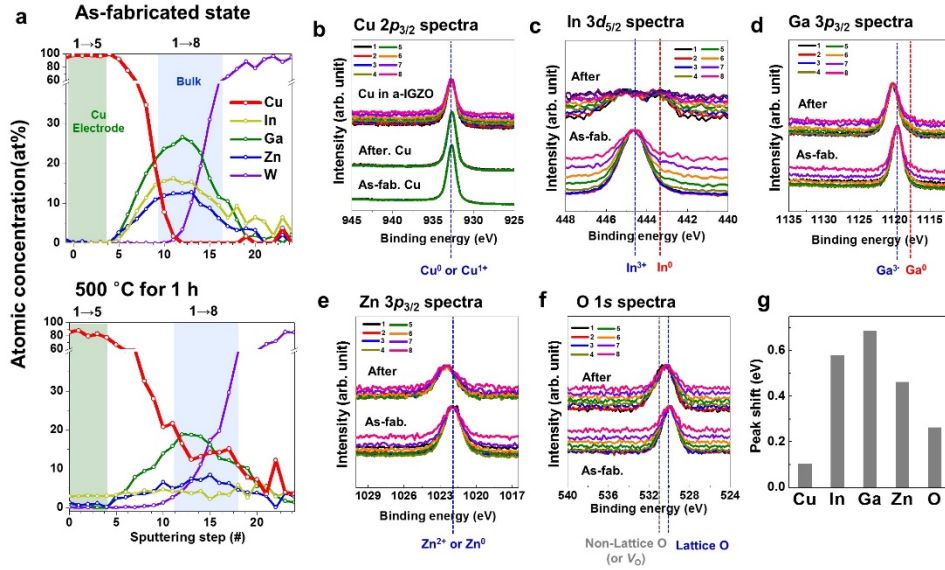


Figure 6.16 (a) Composition XPS profiles of the Ta-Al/Cu/a-IGZO/W/Ta-Al thin films in the as-fabricated state (top) and after annealing at 500 °C for 1 h (bottom). XPS results of (b) Cu, (c) In, (d) Ga, (e) Zn, and (f) O (V_O). (g) XPS peak shift of the elements after the annealing.

6.7. Cu diffusion modeling

Based on the results that In is the most preferred substitutional site for Cu instead of Ga and Zn, we further considered thermodynamic origin of substitutional Cu diffusion as shown below. It has been suggested that dopant may prefer to substitute the same valence cation in complex oxides^[1.60]. Because valence state of Cu can be same with Zn-, it seems that Zn is the most preferred substitutional site. However, when activation energy of substitutional Cu diffusion is considered, it is expected that substitutional Cu dominantly exchange with In following reasons. **Figure 6.17b** depicts the potential energy band diagram of Cu diffusion in terms of diffusion paths. Diffusion through free volume in amorphous materials is resemble with the interstitial diffusion in crystalline materials^[1.41]. To occur Cu diffusion through free volume, Cu solely should jump Gibb free energy for migration of the other site in the free volume (ΔG_m). In the case of substitutional Cu diffusion, however, cation vacant sites are essentially needed in addition to thermal energy enough to overcome ΔG_m . Thus, activation energy of substitutional diffusion is summation of ΔG_m and ΔG_f , ΔG_f is the Gibbs free energy of cation vacancy formation in a-IGZO. Formation of cation vacancy means that In-O, Ga-O, or Zn-O bonding is reduced to metallic In, Ga, or Zn. Thus, ΔG_f is strongly related to standard Gibbs free energy of oxide formation (ΔG_{OX}^0). Probability of cation vacancy formation would increase with increasing the value of ΔG_{OX}^0 . In the range of 300-500 °C, ΔG_{OX}^0 of In the highest values compared to that of Ga and Zn as shown in **Figure 4.4** (e.g., at 400 °C, ΔG_{OX}^0 of In, Ga, and Zn is -4.9, -6.0, and -5.9 eV, respectively)^[4.3]. Therefore, we believe that substitution of Cu into In in a-IGZO dominantly occurs, because In easily reduced compared to Ga or Zn, and subsequently forms substitutional site for Cu.

Notable fact is that although Cu dominantly substitutes In sites during annealing, Cu-In-O clusters are observed after annealing. Moreover, at annealing condition of 400 °C, dominant structural location of Cu is altered from the free volume to Cu-In-O clusters as annealing time is elapsed. We illustrate the diffusion kinetics of Cu in a-IGZO in terms of composition profile changes as shown in **Figure 6.17c**. At Cu/a-IGZO interface, concentration gradient (i.e., chemical potential gradient) of elements exist. C_X denotes the concentration of X(=Cu, In, Ga, or Zn)^[1,41,6,9]. Cu solubility in substitutional sites (S_{sub}) would be higher than Cu solubility at the free volume (S_{free}) because Cu at the free volume is not detected by EDS (**Figure 6.14**) and SIMS (**Figure 6.15**), whereas decrease of In concentration due to substitutional Cu is observed. Moreover, reduction in free volume due to SR^[5,8] may further decrease of S_{free} as depicted in **Figure 6.17a**. As noted above, Two paths are available for Cu diffusion in a-IGZO: free volume (i.e., interstitial sites) and substitutional sites. In general, interstitial diffusion is apt to be faster than substitutional diffusion because of relatively weak bonding of interstitials to neighboring atoms^[1,66,6,10]. Therefore, Cu at the free volume (Cu_i) predominates the electrical properties of a-IGZO at early stage in diffusion (**left in Figure 6.17c**) and dominant electronic states of Cu is an electron donor. However, with further annealing, substitutional Cu diffusion dominantly occurs using In sites, while concentration of Cu at the free volume become saturated (**middle in Figure 6.17c**). After annealing, as ambient temperature decreases to RT, dissolved Cu become supersaturated. As a result, substitutional Cu (Cu_s) and In form Cu-In-O clusters in the bulk of a-IGZO (**right in Figure 6.17c**).

Figure 6.17a summarizes the Cu doping kinetics in a-IGZO. At low temperature annealing (i.e., ≤ 300 °C in this study), Cu hardly substitute In, Ga, or Zn due to lack of thermal energy to overcome activation energy of $\Delta G_m + \Delta G_f$. Instead of

substitutional diffusion, Cu dominantly diffuses in a-IGZO through the free volume. After the annealing, most of Cu are still located at the free volume and Cu-In-O clusters are negligible. Cu located at the free volume act as an electron donor and could generate CF-based RS in a-IGZO. As annealing temperature increases enough to occur substitutional Cu diffusion, Cu dominantly substitutes In. Moreover, substitutional Cu and In form *p*-type Cu-In-O crystalline clusters after the annealing. Bulk-heterogeneous *pn* junction decrease electrical conductivity of a-IGZO and could generate charge trapping/detrapping-based RS. We believe that this unprecedented dynamic Cu doping in AOSs would provide a guideline to design new multi-functional AOSs through Cu doping and to understand the degradation of electrical performance in AOSs electronics due to Cu contamination.

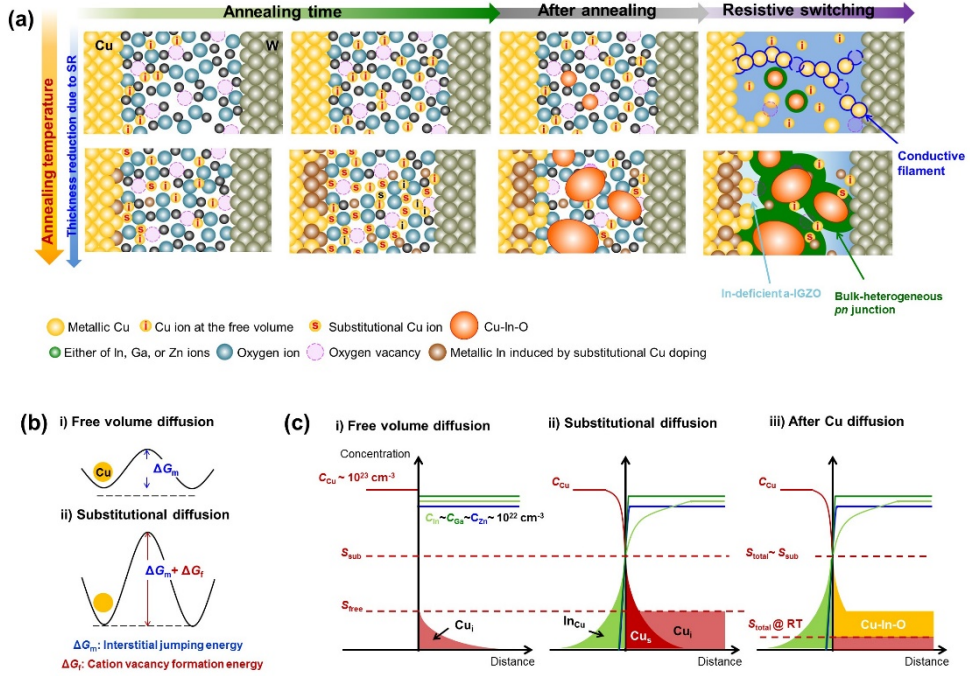


Figure 6.17 Cu doping kinetics in a-IGZO. (a) C atomic movement in the Cu devices according to annealing conditions. (b) Potential energy diagram of Cu diffusion. (c) Composition profile changes in Cu/a-IGZO contacts.

6.8. Summary

In conclusion, we reveal the Cu doping mechanism in a-IGZO and dynamical changes in Cu doping effect on electrical properties of a-IGZO. Cu diffusion occurs through two paths, free volume and substitutional sites. Because Cu diffusion at the free volume is faster than substitutional diffusion, Cu is dominantly located at the free volume in the early stage of annealing and has similar diffusivity with the Cu in SiO₂. Cu at the free volume acts as an electron donor and generates RS behavior based on electrochemical Cu migration. As annealing time is elapsed, substitutional Cu diffusion become predominant which prefer In to Ga or Zn. After annealing, supersaturated Cu forms *p*-type crystalline Cu-In-O clusters. Since bulk-heterogeneous *pn*-junction is formed with reduction of In concentration, electrical conductivity of a-IGZO decreases. Moreover, Cu-In-O clusters induce NDR-based RS in a-IGZO, which is the different RS mechanism to redox reactions of Cu ions. Our results can be readily expanded to universal Cu doping mechanism in AOSs and would enable researchers to develop RS devices based on Cu-doped AOSs.

CHAPTER 7

Conclusion

7.1. Summary of results

This study investigated the effect of thermally driven *intrinsic* and *extrinsic* doping on electrical properties of amorphous oxide semiconductors (AOSs) in terms of annealing temperature and annealing time. Moreover, underlying physics of thermally driven doping were unraveled. A through development of novel devices that enable to prevent unwanted reactions of AOSs with ambient, the changes in electrical properties of AOSs solely induced by atomic rearrangement or migration could be measured. W, which has high self-diffusivity and higher Gibbs free energy of oxide formation compared to In, Ga, or Zn, is appropriate for inert electrode materials. Moreover, W act as blocking layer for Cu diffusion and regulates Cu doping sites. Ta-Al cover effectively inhibits interaction of AOSs with ambient atmosphere.

Based on the novel devices, structural relaxation (SR)-driven *intrinsic* doping phenomena in AOSs were reported. Structural relaxation (SR), which is inherent phenomena in amorphous materials, slowly reduces the randomness of AOS atoms at temperatures below the glass transition temperature (T_g), which alters the electrical characteristics of a-IGZO. Electrical measurements revealed the relaxations increased

the concentration of shallow-donor-state oxygen vacancies (V_{Os}), enabling electron dopants to be added to a-IGZO without using redox chemistry. The activation energy of increase of concentration of V_{Os} in the shallow-donor state is approximately 1.76 eV, which can be attributed to the ionic bonding of a-IGZO.

SR-driven *intrinsic* doping, which is a chemical-free method for enhancing the conductivity of transparent transistor materials could benefit flat-panel and flexible displays. The temperature-dependent doping can be sustained for prolonged annealing times, making it a promising approach for enhancing the thermal stress resistance of flexible electronics.

The final focus of this study is to reveal the extrinsic Cu doping mechanism in AOSs. In the early stage of annealing, Cu dominantly diffuses into a-IGZO through the free volume and acts as an electron donor. Because Cu at the free volume could occur electrochemical migration, resistive switching (RS) characteristics are generated in Cu-doped a-IGZO. With further annealing, substitutional Cu become predominant which prefers In to Ga or Zn. After annealing, supersaturated Cu forms crystalline Cu-In-O clusters in a-IGZO. A bulk-heterogeneous *pn* junction in a-IGZO, induced by Cu-In-O clusters, decreases electrical conductivity of a-IGZO and generates negative differential resistance-based RS.

Dynamic Cu doping effect, which is dependent on the dominant structural location of Cu in AOSs, could provide guidelines for not only a new application of Cu-doped AOSs on RS devices but also estimation of reliability of AOSs electronics due to Cu contamination.

7.2. Future works and suggested research

7.2.1. Effect of O non-stoichiometry on SR-driven doping

In this thesis, SR-driven doping in AOSs are unprecedentedly reported based on novel devices able to regulate *extrinsic* reactions of AOSs with ambient atmosphere and electrodes. Moreover, V_{OS} is believed that the origin of SR-driven doping effect, whereas the influence of H dopant is negligible. However, undercoordinated atoms and weakly bond O (O_{wb}) also have the potential to affect SR-driven doping as introduced in **Section 2.1.2**.

SR-driven doping could also be interpreted in terms of undercoordinated atoms and O_{wb} as depicted in **Figure 7.1**. In the as-deposited state, significant amount of undercoordinated metal (M_{uc}) and O_{wb} is existed in AOS thin-films. Electronic state of M_{UC} is either shallow-donor state or electron trap states located at upper half of the bandgap and O_{wb} act as an electron trap. M_{UC} in the electron trap states and O_{wb} capture free electron from M_{uc} in the shallow-donor states (i.e., charge compensation). When structural densification occurs (i.e., SR), M_{uc} combine with O_{wb} , and changes to fully-coordinated M. Thus, concentration of M_{uc} and O_{wb} decreases during SR and degree of charge compensation decreases. As a result, doping concentration in AOSs increases as SR occurs. In **Section 5**, a-IGZO thin-films are deposited under $P_{O_2,dep.}$ of 3.3×10^{-2} Pa [i.e., $O_2/(Ar+O_2)$ volume ratio of 5%]. This condition could be considered as high $P_{O_2,dep.}$ value enough to form significant amount of O_{wb} ^[1,45].

For the verification of a new hypothesis, influence of initial O non-stoichiometry (i.e., O concentration) in AOSs on SR-driven doping will be investigated. When $P_{O_2,dep.}$ is low, concentration of O_{wb} decreases and consequently the degree of SR-driven doping

phenomena would decrease. This future work would not only reveal a novel mechanism of SR-driven doping effect, but also enable researchers to put an end to the debate about the origin of subgap states in AOSs.

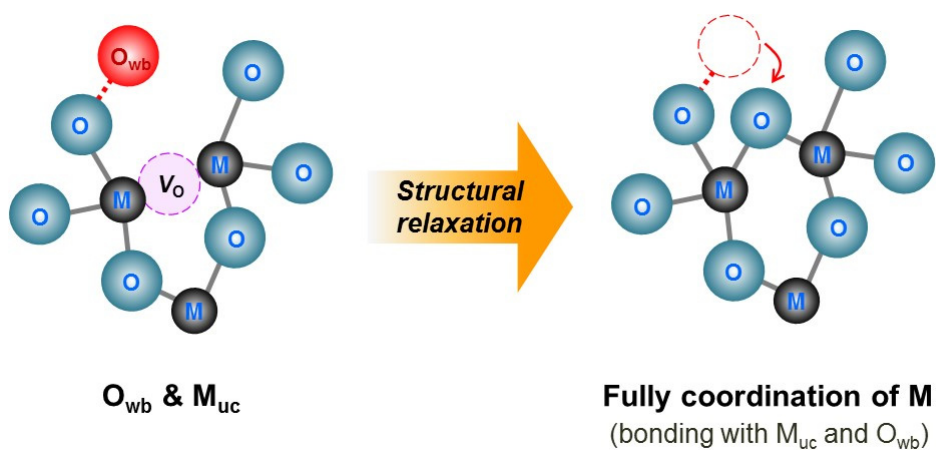


Figure 7.1 Schematics of atomic rearrangement during structural relaxation in AOSs. Reduction in density of O_{wb} as well as M_{uc} would be dominant mechanism of SR-driven doping.

7.2.2. Flexible Cu-doped AOSs memristor

AOSs are favorable to implementation of mechanically flexible memristors due to their microstructural merits likewise in the case of display technology. In this thesis, we demonstrated that Cu doping enable AOSs to become active materials in resistive switching (RS) devices (or memristor) as shown in **Section 6**. However, high temperature annealing (≥ 300 °C) process for Cu doping in AOSs is inadequate for fabrication of flexible memristors. Here we consider that Cu doping in AOSs could be possible through co-deposition process as depicted in **Figure 7.2a**. As Cu deposition rates or AOSs deposition rates is modulated during the deposition, Cu doping concentration and distribution may be controlled. Thus, co-deposition process may design the shape of conductive filaments (CF) and consequently modulate RS characteristics. Moreover, Y. Yang et al., reported that CF formation is affected by not only metal ion mobility but also redox rate of metal ions (**Figure 7.2c**)^[2.39]. Branched structure would be favorable for uniform RS and low redox rate is prerequisite for the structure. We believe that application of p-type conductors (e.g., $\text{Ge}_2\text{Sb}_2\text{Te}_5$)^[7.1], which have free electron as a minority carrier, on the counter electrode would secure low redox rate in the memristors (**Figure 7.2b**). In summary, we will demonstrate high performance-flexible AOSs memristors enabled by Cu doping control and application of p-type conductors on the counter electrodes. We hope that this future work would provide a crucial key to improvement RS uniformity enough to commercialize the RS devices-based electronics (e.g., non-volatile memory, logic, and neuromorphic chips)^[2.29].

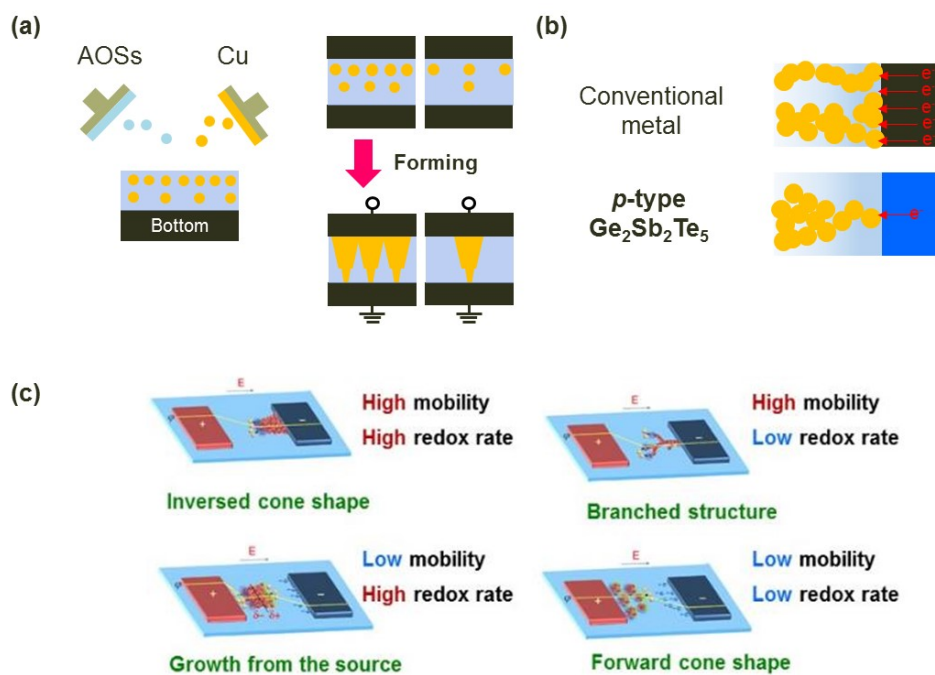


Figure 7.2 (a) Co-deposition process of AOSs with Cu. (b) Application of p -type $\text{Ge}_2\text{Sb}_2\text{Te}_5$ on the counter electrode. (b) CF growth dynamics determined by kinetic parameters: ion mobility and redox rate^[2,39].

References

- [1.1] J. F. Wager, “Transparent electronics”, *Science*, **300**, 1245 (2003).
- [1.2] K. Nomura et al., “Room-temperature fabrication of transparent flexible thin-films transistors using amorphous oxide semiconductors”, *Nature*, **432**, 488 (2004).
- [1.3] T. Kamiya et al., “Present status of amorphous In-Ga-Zn-o thin film transistors”, *Sci. Technol. Adv. Mater.*, **11**, 044305 (2011).
- [1.4] S. Lee et al., “Transparent semiconducting oxide technology for tough free interactive flexible displays”, *Proceeding of the IEEE*, **103**, 644 (2015).
- [1.5] T. Kamiya and H. Hosono, “Handbook of zinc oxide and related materials”, Taylor & Francis, Oxford, UK, p.13 (2012).
- [1.6] H. Hosono, “Ionic amorphous oxide semiconductors: Material design, carrier transport, and device application”, *J. Non-cryst. Solids*, **352**, 851 (2006).
- [1.7] J. Robertson, “Physics of amorphous conducting oxides”, *J. Non-cryst. Solids*, **354**, 2791 (2008).
- [1.8] T. Kamiya et al., “Material characteristics and applications of transparent amorphous oxide semiconductors”, *NPG Asia Mater.*, **2**, 15 (2010).
- [1.9] J. Jin et al., “Rollable transparent glass-fabric reinforced composite”, *Adv. Mater.*, **22**, 4510 (2010).
- [1.10] M.-J. Lee et al., "Low-temperature-grown transition metal oxide based storage materials and oxide Transistors for high-density non-volatile memory ", *Adv. Funct. Mater.*, **19**, 1587 (2009).
- [1.11] S. -M. Yoon et al., “Fully transparent non-volatile memory thin-film

- transistors using an organic ferroelectric and oxide semiconductor below 200 °C”, *Adv. Funct. Mater.*, **20**, 921 (2010).
- [1.12] Y. Chen et al., “High-speed pseudo-CMOS circuits using bulk accumulation a-IGZO TFTs”, *IEEE Electron Device Lett.*, **36**, 153 (2015).
 - [1.13] J. Zhang et al., "Flexible indium–gallium–zinc–oxide Schottky diode operating beyond 2.45 GHz ". *Nature Comm.*, **6**, 7561 (2015).
 - [1.14] J. K. Jeong et al., "Origin of threshold voltage instability in indium-gallium-zinc oxide thin film transistors”, *Appl. Phys. Lett.*, **93**, 123508 (2008).
 - [1.15] J.-S. Park et al., “Novel ZrInZnO thin-film transistor with excellent stability”, *Adv. Mater.*, **21**, 329 (2009).
 - [1.16] M.-G. Kim et al., “Low-temperature fabrication of high-performance metal oxide thin-film electronics via combustion processing”, *Nature Mater.*, **10**, 382 (2011).
 - [1.17] X. Liu et al., “Gate bias Stress-Induced Threshold Voltage Shift effect of a-IGZO TFTs with Cu gate”, *IEEE Trans. Electron Devices*, **61**, 4299 (2014).
 - [1.18] M. D. H. Chowdhury, “Effect of SiO₂ and SiO₂/SiN_x passivation on the stability of amorphous indium-gallium-zinc-oxide thin-film transistors under high humidity”, *IEEE Trans. Electron Devices*, **62**, 869 (2015).
 - [1.19] J. Robertson, “Properties and doping limits of amorphous oxide semiconductors”, *J. Non-cryst. Solids*, **358**, 2437 (2012).
 - [1.20] F. Funabiki et al., “Doping effects in amorphous oxides”, *J. Ceram. Soc. Jpn*, **120**, 447 (2012).
 - [1.21] S. Parthiban et al., “Amorphous boron-indium-zinc-oxide active channel layers for thin-film transistor fabrication”, *J. Mater. Chem. C*, **3**, 1661 (2008).

- [1.22] T. Kamiya et al., “Electronic structure of oxygen deficient amorphous oxide semiconductor $a\text{-InGaZnO}_{4-x}$: Optical analyses and first-principle calculations”, *Phys. Status solidi C*, **5**, 3098 (2008).
- [1.23] T. Kamiya et al., “Electronic structure of the amorphous oxide semiconductor $a\text{-InGaZnO}_{4-x}$: Tauc–Lorentz optical model and origins of subgap state”, *Phys. Status solidi A*, **206**, 860 (2009).
- [1.24] H. -K. Noh et al., “Electronic structure of oxygen-vacancy defects in amorphous In-Ga-Zn-O semiconductors”, *Phys. Rev. B*, **84**, 11205 (2011).
- [1.25] W. Körner et al., “Analysis of electronic subgap states in amorphous semiconductor oxides based on the example of Zn-Sn-O systems”, *Phys. Rev. B*, **86**, 165210 (2012).
- [1.26] W. Körner et al., “Generic origin of subgap states in transparent amorphous semiconductor oxides illustrated for the cases of In–Zn–O and In–Sn–O, cathodes”, *Phys. Status solidi A*, **212**, 1476 (2015).
- [1.27] H. J. Kim et al., “Role of incorporated hydrogen on performance and photo-bias instability of indium gallium zinc oxide thin film transistors”, *J. Phys. D: Appl. Phys.*, **46**, 055104 (2013).
- [1.28] Y. Hanyu et al., “Hydrogen passivation of electron trap in amorphous In-Ga-Zn-O thin-film transistors”, *Appl. Phys. Lett.*, **103**, 202114 (2013).
- [1.29] Y. Jung et al., “High performance and high stability low temperature aqueous solution-derived Li–Zr co-doped ZnO thin film transistors”, *J. Mater. Chem.*, **22**, 5390 (2012).

- [1.30] K.-H. Lim et al., “UV–Visible Spectroscopic Analysis of Electrical Properties in Alkali Metal-Doped Amorphous Zinc Tin Oxide Thin-Film Transistors”, *Adv. Mater.*, **25**, 2994 (2013).
- [1.31] J. Sun et al., “Significant improvement in electronic properties of transparent amorphous indium zinc oxide through yttrium doping”, *Europhys. Lett.*, **106**, 17006 (2014).
- [1.32] J. H. Jeong et al., “Origin of subthreshold swing improvement in amorphous indium gallium zinc oxide transistors”, *Electrochem. Solid-State Lett.*, **11**, H157 (2008).
- [1.33] T. Orui et al., “Charge compensation by excess oxygen in amorphous In–Ga–Zn–O Films deposited by pulsed laser deposition”, *J. Disp. Technol.*, **11**, 518 (2015).
- [1.34] T. Kamiya et al., “Subgap states, doping and defect formation energies in amorphous oxide semiconductor a-InGaZnO₄ studied by density functional theory”, *Phys. Status solidi A*, **207**, 1698 (2010).
- [1.35] T. Kamiya et al., “Origins of High Mobility and Low Operation Voltage of amorphous oxide TFTs: Electronic structure, electron transport, defects and doping”, *J. Disp. Technol.*, **5**, 273 (2009).
- [1.36] S. Jeong et al., “Role of gallium doping in dramatically lowering amorphous-oxide processing temperatures for solution-derived Indium Zinc Oxide thin-film transistors”, *Adv. Mater.*, **22**, 1346 (2010).
- [1.37] K. Ide et al., “Structural relaxation in amorphous oxide semiconductor, a-In-Ga-Zn-O”, *J. Appl. Phys.*, **111**, 073513 (2012).

- [1.38] A. I. Taub, "The kinetics of structural relaxation of a metallic glass", *Acta Metallurgica*, **28**, 1781 (1980).
- [1.39] S. Torquato, "Hard knock for thermodynamics", *Nature*, **405**, 521 (2000).
- [1.40] J. -Y. Cho, "*Phase Stability and Electrical Properties of Amorphous Materials for Electronic Devices Investigated by Mechanical Stress*", Ph D. Dissertation, Seoul National University, Seoul Korea.
- [1.41] D. A. Porter, "*Phase Transformation in Metals and Alloys*", Chapman & Hall, London, UK (1992).
- [1.42] M. Kimura et al., "Tran densities in amorphous-InGaZnO₄ thin-film transistors", *Appl. Phys. Lett.*, **92**, 133512 (2008).
- [1.43] W. Ou-Yang et al., "Controllable film densification and interface flatness for high-performance amorphous indium oxide based thin film transistors", *Appl. Phys. Lett.*, **105**, 163503 (2014).
- [1.44] H. Kim et al., "Low resistance Ti/Au contacts to amorphous gallium indium zinc oxides", *Appl. Phys. Lett.*, **98**, 112107 (2011).
- [1.45] T. Kamiya et al., "Roles of Hydrogen in Amorphous Oxide Semiconductor", *ECS Transactions*, **54**, 103 (2013)
- [1.46] K. Nomura et al., "Defect passivation and homogenization of amorphous oxide thin-film transistor by wet O₂ annealing", *Appl. Phys. Lett.*, **93**, 192107 (2008).
- [1.47] K. Nomura et al., "Origins of threshold voltage shifts in room-temperature deposited and annealed a-In-Ga-Zn-O thin-film transistors", *Appl. Phys. Lett.*, **95**, 013502 (2009).
- [1.48] D. Kang et al., "Amorphous gallium indium zinc oxide thin film transistors: Sensitive to oxygen molecules", *Appl. Phys. Lett.*, **90**, 192101 (2007).

- [1.49] S. R. Elliot, “*Physics of Amorphous Materials*”, John Wiley & Sons, Inc., New York, USA (1990).
- [1.50] H. Hosono et al., “Factors controlling electron transport properties in transparent amorphous oxide semiconductors”, *J. Non-Cryst. Solids*, **354**, 2796 (2008).
- [1.51] K. Nomura et al., “Effects of Diffusion of Hydrogen and Oxygen on Electrical Properties of Amorphous Oxide Semiconductor, In-Ga-Zn-O”, *ECS J. Solid State Sci. Technol.*, **2**, 5 (2013).
- [1.52] H. -K. Noh et al., “Effect of hydrogen incorporation on the negative bias illumination stress instability in amorphous In-Ga-Zn-O thin-film-transistors”, *J. Appl. Phys.*, **113**, 063712 (2013).
- [1.53] Y. Kanai, “Admittance Spectroscopy of Cu-doped ZnO Crystals”, *Jpn. J. Appl. Phys.*, **30**, 703 (1991).
- [1.54] S. J. Wen et al., “Transport Properties of Copper-Doped Indium Oxide and Indium Tin Oxide Ceramics”, *Phys. Stat. Sol., (a)*, **130**, 407 (1992).
- [1.55] H. Kawazoe et al., “P-type electrical conduction in transparent thin films of CuAlO₂”, *Nature*, **389**, 939 (1997).
- [1.56] S. Sheng et al., “p-type transparent conducting oxides”, *Phys. Stat. Sol., (a)*, **203**, 1891 (2006).
- [1.57] J. Robertson et al., “Limits to doping in oxides”, *Phys. Rev. B*, **83**, 075205 (2011).
- [1.58] S. Narushima et al., “A p-Type Amorphous Oxide Semiconductor and Room Temperature Fabrication of Amorphous Oxide p-n Heterojunction Diodes”, *Adv. Mater.*, **15**, 1409 (2003).

- [1.59] T. Kamiya et al., “Electrical Properties and Structure of p-Type Amorphous Oxide Semiconductor $x\text{ZnO} \cdot \text{Rh}_2\text{O}_3$ ”, *Adv. Funct Mater.*, **15**, 968 (2005).
- [1.60] J. E. Medvedeva et al., “Tuning the properties of complex transparent conducting oxides: Role of crystal symmetry chemical composition, and carrier generation”, *Phys. Rev. B*, **81**, 125116 (2010).
- [1.61] P. S. Yun et al., “Metal Reaction Doping and Ohmic Contact with Cu-Mn Electrode on Amorphous In-Ga-Zn-O Semiconductor”, *J. Electrochem. Soc.*, **158**, H1034 (2011).
- [1.62] Y.-H. Tai et al., “The Deterioration of a-IGZO TFTs Owing to the Copper Diffusion after the Process of the Source/Drain Metal Formation”, *J. Electrochem. Soc.*, **159**, J200 (2012).
- [1.63] J.-R. Lim et al., “Effects of Metal Electrode on the Electrical Performance of Amorphous In-Ga-Zn-O Thin Film Transistor”, *Jpn. J. Appl. Phys.*, **51**, 011401 (2012).
- [1.64] C.-K. Lee et al., “High performance Zn-Sn-O thin film transistors with Cu source/drain electrode”, *Phys. Status Solidi RRL*, **7**, 196 (2013).
- [1.65] J. Jeong et al., “Electrical characterization of a-InGaZnO thin-film transistors with Cu source/drain electrodes”, *Appl. Phys. Lett.*, **100**, 112109 (2012).
- [1.66] R. N. Hall et al., “Diffusion and Solubility of Copper in Extrinsic and Intrinsic Germanium, Silicon, and Gallium Arsenide”, *J. Appl. Phys.*, **35**, 379 (1964).
- [1.67] A. A. Istratov et al., “Physics of Copper in Silicon”, *J. Electrochem. Soc.*, **149**, G21 (2002).

- [1.68] H.-W. Yeon et al., “Cu Contamination of the nMOSFET in a 3-D Integrated Circuit under Thermal and Electrical Stress”, *Electrochem. Solid-Sate Lett.*, **15**, H157 (2012).
- [1.69] S. I. Kim et al., “High Reliable and Manufacturable Gallium Indium Zinc Oxide Thin-Film Transistors Using the Double Layers as an Active Layer”, *J. Electrochem. Soc.*, **156**, H184 (2009).
- [1.70] J. D. McBrayer et al., “Diffusion of Metals in Silicon Dioxide”, *J. Electrochem. Soc.*, **133**, 1242 (1986).
- [1.71] N. Banno et al., “Diffusivity of Cu Ions in Solid Electrolyte and Its Effect on the Performance of Nanometer-Scale Switch”, *IEEE Trans. Electron Devices*, **55**, 3283 (2008).
- [1.72] Y. Yang et al., “Observation of conducting filament growth in nanoscale resistive memories”, *Nature Comm.*, **3**, 732 (2012).
- [2.1] R. A. Street, “*Hydrogenated amorphous silicon*”, Cambridge University Press., New York, USA (1991).
- [2.2] J. Robertson et al., “Disorder and instability processes in amorphous conducting oxides” *phys. stat. sol. (b)*, **6**, 1026 (2008).
- [2.3] C. Århammar et al., “Unveiling the complex electronic structure of amorphous metal oxides” *Proc. Natl. Acad. Sci. U.S.A.*, **108**, 6355 (2011).
- [2.4] H.-H. Nahm et al., “Undercoordinated indium as an intrinsic electron-trap center in amorphous InGaZnO₄”, *NPG. Asia Mater.*, **6**, e143 (2014).
- [2.5] T.-C. Fung et al., “Two-dimensional numerical simulation of radio frequency sputter amorphous In–Ga–Zn–O thin-film transistors”, *J. Appl. Phys.*, **106**, 084511 (2009).

- [2.6] S. Sallis et al., “Origin of deep subgap states in amorphous indium gallium zinc oxide: Chemically disordered coordination of oxygen”, *Appl. Phys. Lett.*, **104**, 232108 (2014).
- [2.7] S. Sallis et al., “Deep subgap feature in amorphous indium gallium zinc oxide: Evidence against reduced indium”, *Phys. Status solidi A*, **212**, 1471 (2015).
- [2.8] W. Körner et al., “Origin of subgap states in amorphous In-Ga-Zn-O”, *J. Appl. Phys.*, **114**, 163704 (2013).
- [2.9] K. Nomura et al., “Depth analysis of subgap electronic states in amorphous oxide semiconductor, a-In- Ga-Zn-O, studied by hard x-ray photoelectron spectroscopy”, *J. Appl. Phys.*, **109**, 073726 (2011).
- [2.10] K. Ide et al., “Effects of excess oxygen on operation characteristics of amorphous In-Ga- Zn-O thin-film transistors”, *Appl. Phys. Lett.*, **99**, 093507 (2011).
- [2.11] H.-W. Zan et al., “Achieving High Field-Effect Mobility in Amorphous Indium-Gallium-Zinc Oxide by Capping a Strong Reduction Layer”, *Adv. Mater.*, **24**, 3509 (2012).
- [2.12] S. Aikawa et al., “Suppression of excess oxygen for environmentally stable amorphous In-Si-O thin-film transistors”, *Appl. Phys. Lett.*, **106**, 192103 (2015).
- [2.13] J. Robertson et al., “Light induced instability mechanism in amorphous InGaZn oxide semiconductors”, *Appl. Phys. Lett.*, **104**, 162102 (2014).
- [2.14] B.S.S. Daniel et al., “Thermal Relaxation and High Temperature Creep of Zr₅₅Cu₃₀Al₁₀Ni₅ Bulk Metallic Glass”, *Mechanics of Time-Dependent Materials*, **6**, 193 (2002).

- [2.15] J. Bang, "Densification kinetics of glass films constrained on rigid substrates", *J. Mater. Res.*, **10**, 1321 (1995).
- [2.16] S. M. Sze, "*Physics of Semiconductor Devices*", John Wiley & Sons, Inc., New York, USA (1981).
- [2.17] L. J. Brillson et al., "ZnO Schottky barriers and Ohmic contacts", *Applied Phys. Lett.*, **109**, 121301 (2011).
- [2.18] F. A. Padovani et al., "FIELD AND THERMIONIC-FIELD EMISSION IN SCHOTTKY BARRIERS", *Solid-State Ionics*, **9**, 695 (1966).
- [2.19] J. R. Yeargan et al., "The Poole-Frenkel Effect with Compensation Present", *J. Appl. Phys.*, **39**, 5600 (1968).
- [2.20] G. A. N. Connell et al., "Simplified Theory of Space-Charge-Limited Currents in an Insulator with Traps", *Physical Review*, **103**, 1648 (1956).
- [2.21] M. A. Lampert, "Theory of Poole-Frenkel conduction in low-mobility semiconductors", *Philosophical Magazine*, **26**, 541 (1972).
- [2.22] K. M. Kim et al., "Anode-interface localized filamentary mechanism in resistive switching of TiO₂ thin films", *Appl. Phys. Lett.*, **91**, 012907 (2007).
- [2.23] Q. Liu et al., "Resistive switching memory effect of ZrO₂ films with Zr⁺ implanted", *Appl. Phys. Lett.* **92**, 012117 (2008).
- [2.24] S. A. Mojarad et al., "A comprehensive study on the leakage current mechanisms of Pt/SrTiO₃/Pt capacitor", *J. Appl. Phys.*, **111**, 014503 (2012).
- [2.25] R. Waser, "*Nanoelectronics and information technology*", Wiley-VCH, Weinheim, Germany (2012).
- [2.26] D. B. Strukov et al., "The missing memristor found", *Nature*, **453**, 80 (2008).

- [2.28] F. Pan et al., “Nonvolatile resistive switching memories-characteristics, mechanisms and challenges”, *Progress in Natural Science: Materials International*, **20**, 1 (2010).
- [2.29] J. J. Yang et al., “Memristive devices for computing”, *Nature Nanotech.*, **8**, 13 (2013).
- [2.30] C. Schindler et al., “Electrode kinetics of Cu–SiO₂-based resistive switching cells: Overcoming the voltage-time dilemma of electrochemical metallization memories”, *Appl. Phys. Lett.*, **94**, 072109 (2009).
- [2.31] J.-Y. Chen et al., “Dynamic Evolution of Conducting Nanofilament in Resistive Switching Memories”, *Nano Lett.*, **13**, 3671 (2013).
- [2.32] J. J. Yang et al., “Memristive switching mechanism for metal/oxide/metal nanodevices”, *Nature Nanotech.*, **8**, 13 (2013).
- [2.33] Y. Aoki et al., “Bulk mixed ion electron conduction in amorphous gallium oxide causes memristive behaviour”, *Nature Comm.*, **5**, 3473 (2014).
- [2.34] D. Son et al., “Multifunctional wearable devices for diagnosis and therapy of movement disorders”, *Nature Nanotech.*, **9**, 397 (2014).
- [2.35] Y. C. Yang et al., “Fully Room-Temperature-Fabricated Nonvolatile Resistive Memory for Ultrafast and High-Density Memory Application”, *Nano Lett.*, **9**, 1636 (2009).
- [2.36] X. Guo et al., “Understanding the switching-off mechanism in Ag⁺ migration based resistively switching model systems”, *Appl. Phys. Lett.*, **91**, 133513 (2007).

- [2.37] J. W. McPherson, "Determination of the nature of molecular bonding in silica from time-dependent dielectric breakdown data", *J. Appl. Phys.*, **95**, 8101 (2004).
- [2.38] M. N. Kozicki et al., "A Low-Power Nonvolatile Switching Element Based on Copper-Tungsten Oxide Solid Electrolyte", *IEEE Trans. Nanotech.*, **5**, 535 (2006).
- [2.39] Y. Yang et al., "Electrochemical dynamics of nanoscale metallic inclusions in dielectrics" *Nature Comm.*, **5**, 4232 (2014).
- [2.40] K. Szot et al., "Switching the electrical resistance of XPS studies of individual dislocations in single-crystalline SrTiO₃", *Nature Mater.*, **5**, 312 (2006).
- [2.41] M.-J. Lee et al., "Electrical Manipulation of Nanofilaments in Transition-Metal Oxides for Resistance-Based Memory", *Nano Lett.*, **9**, 1476 (2009).
- [2.42] D.-H. Kwon et al., "Atomic structure of conducting nanofilaments in TiO₂ resistive switching memory", *Nature Nanotech.*, **5**, 148 (2010).
- [2.43] U. Russo et al., "Filament Conduction and Reset Mechanism in NiO-Based Resistive-Switching Memory (RRAM) Devices", *IEEE Trans. Electron Devices*, **56**, 186 (2009).
- [2.44] S.-J. Choi et al., "In Situ Observation of Voltage-Induced Multilevel Resistive Switching in Solid Electrolyte Memory" *Adv. Mater.*, **23**, 3272 (2011).
- [2.45] L. D. Bozano et al., "Organic Materials and Thin-Film Structures for Cross-point Memory Cells Based on Trapping in Metallic Nanoparticles", *Adv. Mater.*, **15**, 1933 (2005).
- [2.46] B. K. Ridley, "Specific Negative Resistance in Solids", *Proc. Phys. Soc.*, **82**, 954 (1963).

- [2.47] A. Laiho et al., “Tuning the electrical switching of polymer/fullerene nanocomposite thin film devices by control of morphology”, *Appl. Phys. Lett.*, **93**, 203309 (2008).
- [3.1] O. Bierwagen et al., “Causes of incorrect carrier-type identification in van der Pauw–Hall measurements”, *Appl. Phys. Lett.*, **93**, 242108 (2008).
- [3.2] P. E. Blöchl, “Projector augmented-wave method”, *Phys. Rev. B*, **50**, 17953 (1994).
- [3.3] J. P. Perdew, “Generalized Gradient Approximation Made Simple”, *Phys. Rev. Lett.*, **77**, 3865 (1996).
- [3.4] G. Kresse et al., “From ultrasoft pseudopotentials to the projector augmented-wave method”, *Phys. Rev. B*, **59**, 1758 (1999).
- [3.5] Y. Kang et al., “Band-structure calculations for the 3d transition metal oxides in GW”, *Phys. Rev. B*, **87**, 085112 (2013).
- [3.6] S. Lany, “The potential-sweep method: A theoretical analysis”, *Electrochim. Acta.*, **11** (3), 321-335, (1966).
- [4.1] K. Nomura et al., “Subgap states in transparent amorphous oxide semiconductor, In–Ga–Zn–O, observed by bulk sensitive x-ray photoelectron spectroscopy”, *Appl. Phys. Lett.*, **92**, 202117 (2008).
- [4.2] K. Nomura et al., “Local coordination structure and electronic structure of the large electron mobility amorphous oxide semiconductor In–Ga–Zn–O: Experiment and *ab initio* calculations”, *Phys. Rev. Lett.*, **75**, 035212 (2007).
- [4.3] I. Barin, O. Knacke, and O. Kubaschewski, “*Thermochemical Properties of Inorganic Substances*”, Springer, Berlin, Germany (1973).

- [4.4] F. P. Fehlner “*Low-Temperature Oxidation: The Role of Vitreous Oxides*”, John Wiley & Sons, Inc, New York, USA (1986).
- [4.5] P. K.-Kursula, “Accuracy, Precision and Detection Limits of SEM–WDS, SEM–EDS and PIXE in the Multi-Elemental Analysis of Medieval Glass”, *X-Ray Spectrom.*, **29**, 111 (2000).
- [4.6] R. E. Galindo et al., “Towards nanometric resolution in multilayer depth profiling: a comparative study of RBS, SIMS, XPS and GDOES”, *Anal Bioanal Chem.*, **396**, 2725 (2010).
- [4.7] F. Zhu et al., “Investigation of annealing effects on indium tin oxide thin films by electron energy loss spectroscopy”, *Thin Solid Films*, **359**, 244 (2000).
- [4.8] M. Passlack et al., “Ga₂O₃ films for electronic and optoelectronic applications”, *J. Appl. Phys.*, **77**, 686 (1995).
- [4.9] A. Hartmann et al., “Influence of Copper Dopants on the Resistivity of ZnO Films”, *Surface and Interface Analysis*, **24**, 671 (1996).
- [4.10] C. D. Wagner et al., NIST Standard Reference Database 20, Version 3.4 (web version), <http://srdata.nist.gov/xps/>, accessed: 4 (2015).
- [4.11] F. Y. Xie et al., “XPS studies on surface reduction of tungsten oxide nanowire film by Ar⁺ bombardment”, *J. Electron Spectrosc. Relat. Phenom.*, **185**, 112 (2012).
- [4.12] H.-K. Kim et al., “Formation of low resistance nonalloyed Al/Pt ohmic contacts on n-type ZnO epitaxial layer”, *J. Appl. Phys.*, **94**, 4225 (2003).
- [4.13] H. B. Michaelson, “The work function of the elements and its periodicity”, *J. Appl. Phys.*, **48**, 4729 (1977).

- [5.1] R. F. Pierret, “*Semiconductor Devices Fundamentals*”, Addison-Wesley, New York, USA (1996).
- [5.2] K. Shibuya et al., “Impact of Defect Distribution on Resistive Switching Characteristics of Sr_2TiO_4 Thin Films”, *Adv. Mater.*, **22**, 411 (2010).
- [5.3] D. K. Scrhoder, “*Semiconductor Material and Device Characterization*”, John Wiley & Sons, Hoboken, USA (1968).
- [5.4] R. L. Angle et al., “Electrical and Charge Storage Characteristics of the Tantalum Oxide-Silicon Dioxide Device”, *IEEE Trans. Electron Devices*, **25**, 1277 (1978).
- [5.5] H.-J. Chung et al., “Bulk-Limited Current Conduction in Amorphous InGaZnO Thin Films”, *Electrochem. Solid-Sate Lett.*, **11**, H51 (2008).
- [5.6] T. Kamiya et al., “Electronic Structures Above Mobility Edges in Crystalline and Amorphous In-Ga-Zn-O: Percolation Conduction Examined by Analytical Model”, *J. Disp. Technol.*, **5**, 462 (2009).
- [5.7] B. K. Meyer et al., “SHALLOW DONORS IN GaN-THE BINDING ENERGY AND THE ELECTRON EFFECTIVE MASS”, *Solid State Comm.*, **95**, 597 (1995)
- [5.8] H.-W. Yeon et al., “Structural-relaxation-driven electron doping of amorphous oxide semiconductors by increasing the concentration of oxygen vacancies in shallow-donor states”, *NPG Asia Mater.*, **Accepted** (2015).
- [5.9] M. Housa, “*High-k gate dielectric*”, Institute of Physics, Bristol, ENGLAND (2004).
- [5.10] V. V. Afanas’ev et al., “Electron energy barriers between (100)Si and ultrathin stacks of SiO_2 , Al_2O_3 , and ZrO_2 insulators ”, *Appl. Phys. Lett.*, **78**, 3073 (2001).

- [5.11] K. Mallik et al., “Schottky diode back contacts for high frequency capacitance studies on semiconductors”, *Solid-State Electronics*, **48**, 231 (2004).
- [5.12] A. Türüt et al., “Determination of the density of Si-metal interface states and excess capacitance caused by them”, *Physica B*, **179**, 285 (1992).
- [5.13] K Steiner, “Capacitance-Voltage Measurements on Schottky Diodes with Poor Ohmic Contacts”, *IEEE Trans. Instrum. Meas.*, **42**, 39 (1993).
- [5.14] A. Janotti et al., “Hydrogen multicenter bonds”, *Nature*, **6**, 44 (2007).
- [5.15] J. Lee et al., “The influence of the gate dielectrics on threshold voltage instability in amorphous indium-gallium-zinc oxide thin film transistors”, *Appl. Phys. Lett.*, **95**, 123502 (2009).
- [6.1] A. S. Lee et al., “Development and Characterization of a PECVD Silicon Nitride for Damascene Applications”, *J. Electrochem. Soc.*, **151**, F7 (2004).
- [6.2] Y. S.-Diamond, “*Advanced Nanoscale ULSI Interconnects: Fundamentals and Applications*”, Springer-Verlag, New York, USA (2009).
- [6.3] R. Waser et al., “Redox-Based Resistive Switching Memories –Nanoionic Mechanisms, Prospects, and Challenges”, *Adv. Mater.*, **21**, 2632 (2009).
- [6.4] W. Guan et al., “On the resistive switching mechanisms of Cu/ZrO₂:Cu/Pt”, *Appl. Phys. Lett.*, **93**, 223506 (2008).
- [6.5] N. Xu et al., “Characteristics and mechanism of conduction/set process in TiN/ZnO/Pt”, *Appl. Phys. Lett.*, **92**, 232112 (2008).
- [6.6] L. Q. Wang et al., “S Temperature dependence of the resistance of metallic nanowires of diameter ≥ 15 nm: Applicability of Bloch-Grüneisen theorem”, *Phys. Rev. B*, **74**, 035426 (2006).

- [6.7] T. Böske et al., “Cu-O network-dependent core-hole screening in low-dimensional cuprate systems: A high-resolution x-ray photoemission study”, *Phys. Rev. B*, **57**, 138 (1998).
- [6.8] J. P. Espinós et al., “Interface Effects for Cu, CuO, and Cu₂O Deposited on SiO₂ and ZrO₂. XPS Determination of the Valence State of Copper in Cu/SiO₂ and Cu/ZrO₂ Catalysts”, *J. Phys. Chem. B*, **106**, 6921 (2002).
- [6.9] N. Kimizuka et al., “Spinel, YbFe₂O₄, and Yb₂Fe₃O₇ Types of Structures for Compounds in the In₂O₃ and Sc₂O₃-A₂O₃-BO Systems [*A*: Fe, Ga, or Al; *B*: Mg, Mn, Fe, Ni, Cu, or Zn] at Temperatures over 1000 °C”, *J. Solid State Chemistry*, **60**, 382 (1985).
- [6.10] N. E. B. Cowern et al., “Experiments on Atomic-Scale Mechanisms of Diffusion”, *Phys. Rev. Lett.*, **67**, 212 (1991).
- [7.1] A. Pirovano et al., “Electronic Switching in Phase-Change Memories”, *IEEE Trans. Electron Devices*, **51**, 452 (2004).

요약(국문초록)

2 중 이상의 다양한 전이후(post-transition) 금속을 조합한 비정질 산화물반도체는 비정질 구조에 기인한 물리적 장점과 전이금속과 산소의 이온결합 특성에 따른 우수한 전기적·광학적 성질을 동시에 발현할 수 있는 물질이다. 무질서한 원자구조를 갖는 비정질 산화물 반도체는 오히려 규칙적인 원자구조를 갖는 결정질 산화물반도체보다 균일한 전기적 특성 및 우수한 기계적 유연성을 갖고, 전이금속의 s 오비탈에 의한 이온결합은 비정질상에서도 결정질상과 비슷한 전자구조를 유지할 수 있어서 공유결합 기반의 비정질 물질보다 우수한 전자 모빌리티를 갖고, 가시광선 영역에서 투명한 성질을 보인다. 즉 균일성, 기계적 유연성, 우수한 모빌리티, 투명성을 갖는 비정질 산화물 반도체를 기반으로 대면적, 유연, 투명 전자소자를 구현하려는 시도가 활발히 이루어지고 있다.

하지만 현재까지 비정질 산화물반도체의 전기적 성능 및 안정성을 완벽히 조절하지 못하고 있는 실정이다. 이는 비정질 산화물반도체의 전기적 성능 및 안정성을 결정짓는 인자인 도펀트의 도핑효과를 결정질 반도체의 경우와 달리 확실히 규명하지 못하고 있기 때문이며, 이러한 점이 비정질 산화물 반도체를 산업화하는 데 큰 장애물로 작용하고 있다. 비정질 산화물반도체 내 도펀트의 전자상태(electronic state)는 주위 국부적인 원자구조에 영향을 받기 때문에 비정질 상의 무질서도에 따라서 도핑효과가 달라질 수 있다. 비정질 구조는 열역학적으로 준안정상 구조이기 때문에 결정화가 일어나지 않는 온도에서도 구조가 변할 수 있는 가능성을 내포하고 있다. 게다가 비정질 산화물반도체의 주위환경과의 높은 반응성에 의해서 내인성(*intrinsic*) 도펀트 및 외인성(*extrinsic*) 도펀트의 양이 변화될 수 있기에 도펀트의 도핑효과를 정확히 규명하는 데 어려움이 있다.

그러므로 비정질 산화물반도체의 전기적 성능 및 안정성을 조절하기 위해서는 비정질 산화물반도체의 외부반응을 제한할 수 있는 상황에서 온도 및 시간의존적인 비정질 구조의 변화에 따른 도펀트의 도핑효과를 체계적으로 규명하는 것이 필요하다. 본 연구는 비정질 산화물반도체와 주위 환경과의 반응을 차단할 수 있는 전자소자를 개발하고 온도와 시간에 따른 비정질 산화물반도체의 전기적 특성 변화를 측정하여 내인성 및 외인성 도펀트의 전자상태 변화를 확인하였다. 이를 바탕으로 미세구조적인 측면인 비정질 무질서도 및 도펀트의 구조적 위치 변화를 연계시켜서 도핑 메커니즘을 규명하였다. 또한 외인성 도핑 농도 및 분포 조절을 통해서 비정질 산화물반도체의 저항이 전기적 응력에 따라 가역적으로 변화할 수 있는 성질을 구현하였다.

내인성 도펀트인 산소 공공(oxygen vacancy)은 주위 원자구조 환경에 따라서 전자상태가 shallow 도너(donor), deep 도너, 혹은 트랩으로 변화할 수 있다고 알려져 있다. 즉, 같은 양의 산소공공이 있더라도 비정질 산화물반도체의 구조적 무질서도에 따라서 비정질 산화물반도체의 전기적 특성이 결정되고, 비정질 구조 완화(structural relaxation)에 의해서 그 특성이 변할 수 있다. 본 연구에서는 어닐링 후에 비정질 In-Ga-Zn-O (IGZO)의 shallow 도너 농도변화를 측정하였다. 어닐링 온도가 300 에서 450 도로 증가함에 따라서 shallow 도너 농도가 1000 배 증가함을 확인했고, 이에 대한 활성화 에너지는 IGZO 의 결합에너지와 비슷한 1.60 eV 로 도출할 수 있었다. 450 도 9 시간 어닐링 후에 IGZO 박막의 두께가 6.3 % 감소한 것을 통해서, 비정질 구조완화에 의해서 IGZO 내 자유부피(free volume)가 감소함에 따라 deep 도너 혹은 트랩상태에 있던 산소 공공이 shallow 도너로 전자상태가 바뀌는 현상이 내인성 도핑 메커니즘임을 제안하였다.

외인성 도펀트인 구리는 결정질 산화물 반도체에서 물질의 전도타입을 n 형에서 p 형을 바꾸는데 중요한 역할을 하지만, 구리가 도핑된 결정질 산화물 반도체가 비정질 상태로 바뀌면 물질 고유의 p 형 전도특성이 사라지고 절연체 특성이

나타나는 것으로 보고되고 있다. 또한 현재까지 비정질 산화물반도체에서의 Cu 도펀트의 전자상태를 정확하게 규명하지 못하고 있는 실정이다. 본 연구에서는 다양한 어닐링 온도 및 시간에 따라 IGZO 내부로 Cu 를 확산시킨 후, IGZO 의 전기적 특성변화, 화학적 상태 변화 및 미세구조변화를 관찰하였다. Cu 확산방식은 크게 침입형(interstitial)과 치환형(substitutional)으로 나눌 수 있는데, 낮은 어닐링 온도에서는 침입형 확산이 발생하고, 어닐링 후에는 침입형 공간에 있는 Cu 도펀트가 shallow 도너 역할을 하는 것을 확인하였다. 또한 침입형 공간에 위치한 Cu 는 전계에 의해서 IGZO 내부로 이동이 용이하고, 이러한 특성으로 인해서 침입형 Cu 가 도핑된 IGZO 에 가역적 저항변화 현상이 발현되었다. 치환형 확산이 발생할 수 있는 온도조건에서도 침입형 확산이 치환형 확산보다 속도가 빠르기 때문에 어닐링 초기에는 침입형 공간에 위치한 Cu 의 농도가 치환형 Cu 농도보다 많다. 하지만 어닐링 시간이 길어짐에 따라서 자유부피공간에 위치한 Cu 보다 치환형 Cu 농도가 더 많아진다. Cu 는 IGZO 구성원소 중 In 과 상호 확산을 활발하게 하며, 어닐링 후에는 Cu-In-O 기반의 결정질 응집체가 형성된다. *p* 형 Cu-In-O 응집체는 *n* 형 IGZO 내부에 불균일(heterogeneous) *pn* 접합을 형성시켜 IGZO 의 전도도를 감소시킬 뿐만 아니라, *pn* 접합의 공간하전영역 (space charge region)의 변화를 기반으로 하는 가역적 저항변화현상을 발생시킨다. 즉, Cu 확산 도핑조건에 따라 Cu 도펀트의 전자상태가 역동적으로 변화함을 최초로 보고하였고, 비정질 산화물반도체 내 Cu 도핑조절을 통해서 저항변화소자의 구현 및 성능을 조절할 수 있음을 제안하였다.

본 연구는 비정질 산화물반도체의 온도와 시간에 따른 도핑효과를 측정할 수 있는 전자소자를 개발한 것을 바탕으로, 도펀트의 구조적 위치변화 및 새로운 상(phase) 형성에 따른 내인성 및 외인성 도펀트의 도핑 메커니즘을 규명한 연구이다. 오직 비정질 무질서도 감소를 통해서 비정질 산화물 반도체의

전자농도를 조절할 수 있음을 실험적으로 제안하고, 외인성 도펀트의 농도 및 분포조절을 통해서 단순히 전자농도를 조절하는 것뿐만 아니라 비정질 산화물반도체 내 새로운 기능성을 부여할 수 있다는 가능성을 제시하는 것에 의미가 있다.

표제어: 비정질 산화물반도체, In-Ga-Zn-O, 도핑, 산소공공, 구리, 전자상태, 구조완화, 확산, 저항변화현상, 메모리스터

학 번: 2009-23046